UNIVERSIDAD DE INVESTIGACIÓN DE TECNOLOGÍA EXPERIMENTAL YACHAY

Escuela de Ciencias Químicas e Ingeniería

TÍTULO: Modelling of coordination polymer of M^{2+} (M = Zn, Co, Cu) from ditopic organic linkers (maleic acid, 1,2-dicarboxylic-bencene acid and 4,4'-bipyridine) and their photoreactive properties.

Trabajo de integración curricular presentado como requisito para la obtención del título de Químico.

Autor:

Escobar Pullas Alexander Eduardo

Tutor:

Ph.D. – Thibault Terencio

Co-Tutor:

Ph.D. – Ávila Edward

Urcuquí, Junio 2021

UNIVERSIDAD
YACHAY
TECH

Urcuquí, 24 de junio de 2021

SECRETARÍA GENERAL
(Vicerrectorado Académico/Cancillería)
ESCUELA DE CIENCIAS QUÍMICAS E INGENIERÍA
CARRERA DE QUÍMICA
ACTA DE DEFENSA No. UITEY-CHE-2021-00016-AD

A los 24 días del mes de junio de 2021, a las 16:00 horas, de manera virtual mediante videoconferencia, y ante el Tribunal Calificador, integrado por los docentes:

Presidente Tribunal de Defensa	Dr. SAUCEDO VAZQUEZ, JUAN PABLO , Ph.D.
Miembro No Tutor	Dr. SOMMER MARQUEZ, ALICIA ESTELA , Ph.D.
Tutor	Dr. TERENCIO THIBAULT , Ph.D.

El(la) señor(ita) estudiante **ESCOBAR PULLAS, ALEXANDER EDUARDO**, con cédula de identidad No. 1722403340, de la **ESCUELA DE CIENCIAS QUÍMICAS E INGENIERÍA**, de la Carrera de **QUÍMICA**, aprobada por el Consejo de Educación Superior (CES), mediante Resolución **RPC-SO-39-No.456-2014**, realiza a través de videoconferencia, la sustentación de su trabajo de titulación denominado: **MODELLING OF COORDINATION POLYMER OF POLYMER OF M2+ (M = ZN, CO, CU) FROM DITOPIC ORGANIC LINKERS (MALEIC ACID, 1,2-DICARBOXYLIC-BENCENE ACID AND 4,4'-BIPYRIDINE) AND THEIR PHOTOREACTIVE PROPERTIES**, previa a la obtención del título de **QUÍMICO/A**.

El citado trabajo de titulación, fue debidamente aprobado por el(los) docente(s):

Tutor	Dr. TERENCIO THIBAULT , Ph.D.
Co - Tutor	Dr. AVILA SOSA, EDWARD EBNER , Ph.D.

Y recibió las observaciones de los otros miembros del Tribunal Calificador, las mismas que han sido incorporadas por el(la) estudiante.

Previamente cumplidos los requisitos legales y reglamentarios, el trabajo de titulación fue sustentado por el(la) estudiante y examinado por los miembros del Tribunal Calificador. Escuchada la sustentación del trabajo de titulación a través de videoconferencia, que integró la exposición de el(la) estudiante sobre el contenido de la misma y las preguntas formuladas por los miembros del Tribunal, se califica la sustentación del trabajo de titulación con las siguientes calificaciones:

Tipo	Docente	Calificación
Tutor	Dr. TERENCIO THIBAULT , Ph.D.	10,0
Presidente Tribunal De Defensa	Dr. SAUCEDO VAZQUEZ, JUAN PABLO , Ph.D.	10,0
Miembro Tribunal De Defensa	Dr. SOMMER MARQUEZ, ALICIA ESTELA , Ph.D.	10,0

Lo que da un promedio de: **10 (Diez punto Cero)**, sobre 10 (diez), equivalente a: **APROBADO**

Para constancia de lo actuado, firman los miembros del Tribunal Calificador, el/la estudiante y el/la secretario ad-hoc.

Certifico que *en cumplimiento del Decreto Ejecutivo 1017 de 16 de marzo de 2020, la defensa de trabajo de titulación (o examen de grado modalidad teórico práctica) se realizó vía virtual, por lo que las firmas de los miembros del Tribunal de Defensa de Grado, constan en forma digital.*

ESCOBAR PULLAS, ALEXANDER EDUARDO
Estudiante

JUAN PABLO
SAUCEDO
VAZQUEZ

Firmado digitalmente por JUAN PABLO SAUCEDO VAZQUEZ
Fecha: 2021.07.06 09:11:47 -05'00'

Dr. SAUCEDO VAZQUEZ, JUAN PABLO , Ph.D.
Presidente Tribunal de Defensa

THIBAULT
TERENCIO

Dr. TERENCIO THIBAULT , Ph.D.
Tutor

ALICIA ESTELA
SOMMER
MARQUEZ

Firmado digitalmente por
ALICIA ESTELA SOMMER
MARQUEZ
Fecha: 2021.07.07 21:05:03
-05'00'

Dr. SOMMER MARQUEZ, ALICIA ESTELA , Ph.D.
Miembro No Tutor

CARLA SOFIA
YASELGA NARANJO

Digitally signed by CARLA
SOFIA YASELGA NARANJO
Date: 2021.07.07 17:19:33
-05'00'

YASELGA NARANJO, CARLA
Secretario Ad-hoc

AUTORÍA

Yo, **ALEXANDER EDUARDO ESCOBAR PULLAS**, con cédula de identidad 1722403340, declaro que las ideas, juicios, valoraciones, interpretaciones, consultas bibliográficas, definiciones y conceptualizaciones expuestas en el presente trabajo; así cómo, los procedimientos y herramientas utilizadas en la investigación, son de absoluta responsabilidad de el/la autora (a) del trabajo de integración curricular. Así mismo, me acojo a los reglamentos internos de la Universidad de Investigación de Tecnología Experimental Yachay.

Urcuquí, junio del 2021.

Alexander Eduardo Escobar Pullas

CI: 1722403340

AUTORIZACIÓN DE PUBLICACIÓN

Yo, **ALEXANDER EDUARDO ESCOBAR PULLAS,** con cédula de identidad 1722403340, cedo a la Universidad de Tecnología Experimental Yachay, los derechos de publicación de la presente obra, sin que deba haber un reconocimiento económico por este concepto. Declaro además que el texto del presente trabajo de titulación no podrá ser cedido a ninguna empresa editorial para su publicación u otros fines, sin contar previamente con la autorización escrita de la Universidad.

Asimismo, autorizo a la Universidad que realice la digitalización y publicación de este trabajo de integración curricular en el repositorio virtual, de conformidad a lo dispuesto en el Art. 144 de la Ley Orgánica de Educación Superior

Urcuquí, junio del 2021.

Alexander Eduardo Escobar Pullas

CI: 1722403340

DEDICATORIA

El presente trabajo está dedicado a mis padres y hermanos; quienes me vieron crecer y nunca me dejaron caer; ellos me enseñaron a soñar alto y luchar por los objetivos que persigo. Mi queridos padres, Raquel y Jorge, este trabajo es para ustedes porque ustedes no permitieron ninguna dificultad nos detenga a mis hermanos y a mí. Mis hermanos, Mary y Nico, este trabajo también es de ustedes por crecer conmigo y siempre hacerme ver el potencial que tengo. Ellos son y serán los motores de mi vida.

También este trabajo lo dedico a mi abuelito, José, que lleno de alegrías y ocurrencias mi niñez y juventud, siempre lo recordaré y llevaré en mi corazón.

Alexander Escobar

AGRADECIMIENTO

Este trabajo sin duda refleja mi crecimiento como persona durante mi carrera universitaria en Yachay Tech; por eso quiero agradecer a quienes forman parte de esta etapa tan bonita de mi vida.

Quiero agradecer a mis padres por todo el apoyo que me han dado independientemente de las situaciones que se han presentado siempre han estado para mí, gracias por su esfuerzo, soporte y el amor que nunca me faltó. De la misma forma, quiero agradecer a mis hermanos, por ser mis amigos, mis cómplices y siempre motivarme a seguir mis sueños. También, quiero agradecer a mis abuelitos José y Carmen; a mis tíos Jaime, Pato, Pepe y Rosi, y a mi primo David por ser una parte fundamental de mi vida, gracias por sus palabras, apoyo y cariño.

También quiero agradecer a mis profesores en Yachay Tech, en especial al profesor Antonio Díaz a quien también lo considero un gran amigo y a mis tutores que fueron mi soporte durante el desarrollo de este trabajo, Thibault y Edward, gracias por guiarme durante todo este proceso. Quiero dar también un gran agradecimiento a mis amigos más cercanos de la universidad que se volvieron mi segunda familia; en especial a mis roomies y los chicos de la patrimonial 18 por estar conmigo desde nivelación.

Quiero finalizar agradeciendo a los chicos, profesores y personas que me apoyaron en mis proyectos académicos y extracurriculares por hacer de Yachay Tech mi lugar favorito, un lugar de ciencia y amigos.

Alexander Escobar

RESUMEN

Los Metal-Organic Frameworks (MOFs) son un tipo de polímeros de coordinación que se caracterizan por su gran versatilidad, área superficial y porosidad regular. Los MOFs están constituidos principalmente por iones o clústeres metálicos coordinados por ligantes orgánicos formando polímeros cristalinos. Estos polímeros de coordinación se dividen en tres generaciones desde compuestos con utilidad estructural hasta la tercera generación que corresponde a MOFs sensibles a estímulos. Se realizó síntesis hidrotermal utilizando hexametilentetramina (HMTA), 4,4'bipiridina y ácido maleico como ligantes y las siguientes sales metálicas: cloruro de cobre (II), cloruro de manganeso (II), nitrato de zinc (II) y nitrato de cobalto (II) por sus respectivos iones metálicos. Las dieciocho muestras obtenidas fueron caracterizadas por FTIR y espectroscopía UV-Vis, pero solo las muestras de la tercera fase fueron aptas para ser analizadas por difracción de rayos X (DR-X). Las fases identificadas por DRX solo incluyeron 4,4-bipiridina y contraiones y/o moléculas de agua en la esfera de coordinación. Los polímeros de coordinación identificados de Cu (II) y Mn (II) presentaron porosidades demasiado pequeñas para aplicaciones de adsorción; por otro lado, las fases identificadas de Co (II) y Zn (II) son minoritarias, pero solo podrían ser útiles para la adsorción de moléculas pequeñas como el dióxido de carbono.

La modelación de estos compuestos se hizo a partir de las fases identificadas por DRX, los patrones DRX simulados se compararon con los patrones experimentales. Por otro lado, se postuló una posible modificación post sintética mediante la ciclo-adición por Diels Alder del 1,3-butadieno al ácido maleico y la una posible foto-respuesta por la dimerización del anhídrido maleico cuando está de ligante. Para corroborar ambas posibilidades se calculó la orientación y superposición de orbitales que favorezcan esta reacción. Lo polímeros sintetizados son estructuras base, pero cuya modificación permitiría polímeros de coordinación funcionales con especial aplicación en absorción de gases.

Palabras Clave: MOFs, polímero de coordinación, adsorción, photo-respuesta, poros.

ABSTRACT

Metal-Organic Frameworks (MOFs) are a type of coordination polymers. These materials have great versatility, surface area, and regular porosity. MOFs are mainly constituted by ions or metal clusters coordinated by organic ligands forming crystalline polymers. MOFs are divided into three generations, from compounds with a structural utility to the third generation that corresponds to stimulus-sensitive MOFs, with application in almost all branches of industry. In the present work, hydrothermal synthesis was performed using hexamethylenetetramine (HMTA), 4,4'bipyridine, and maleic acid as binders and the following metal salts: copper (II) chloride, manganese (II) chloride, zinc nitrate (II), and cobalt (II) nitrate for their respective metal ions. The eighteen obtained samples were characterized by FTIR and UV-Vis spectroscopy. However, only the samples from the third phase were suitable for analysis by X-ray diffraction (X-DR). The phases identified by XRD only included 4,4-bipyridine and counter ions and/or water molecules in the coordination sphere. The identified coordination polymers of Cu (II) and Mn (II) present negligible porosities, so their application for gas adsorption was discarded.On the other hand, the identified phases of Co (II) and Zn (II) could only be useful for adsorption of small molecules such as carbon dioxide.

The modeling of these compounds was made from the phases identified by XRD, the simulated XRD patterns were compared with the experimental patterns. On the other hand, a possible post-synthetic modification was also postulated by Diels Alder's addition of 1,3-butadiene to maleic acid, and a possible photo-response by the dimerization of maleic anhydride. To corroborate both possibilities, the orbitals and orbital superposition's orientation that favored this reaction was calculated. The synthesized polymers are base structures whose modification would allow functional coordination polymers with a possible application in gas adsorption.

Key Words: MOFs, Coordination polymer, adsorption, photo-response, pores.

CONTENT

CHAPTER I: Introduction 14

CHAPTER II: Problem Statement 16

- General Objective 16
- Specific Objectives 16

CHAPTER III: Background 18

- 3.1 Porous Materials 18
- 3.2 Reticular Chemistry 19
- 3.3 MOFs 20
- 3.3.1 Structure of MOFs 22
  - 3.3.1.2 Single metal-ion nodes and Secondary Building Units 24
- 3.3.2 Architecture of Networks and Porous Structures 25
  - 3.4 Synthetic Methods of MOFs 26
- 3.5 Stimuli-Responsive Materials 27
- 3.5.1 Responsive MOFs 27
- 3.5.2 Photo-responsive MOFs 28
- 3.6 Referenced materials 28

CHAPTER IV: Methodology 31

- 4.1 Synthesis of MOFs 31
  - 4.1.1 Materials and reagents 31
- 4.2 Experimental procedures 31
  - 4.2.1 First Stage (Hydrothermal Synthesis) 32
  - 4.2.2 Second Stage (Reflux Conditions) 34
  - 4.2.3 Third Stage (Hydrothermal Synthesis) 35
- 4.3 Characterization Techniques 37
  - 4.3.1 Attenuated Total Reflection FTIR Spectroscopy 37
  - 4.3.3 Diffuse Reflectance UV-Vis Spectroscopy 38
  - 4.3.3 X-Ray Powder Diffraction Spectroscopy 39

CHAPTER V: Results and Discussion 41

- 5.1 Compounds of manganese, HMTA and maleic acid (AEEA001, AEEA002 and AEEA003) 45
  - 5.1.1 Attenuated Total Reflectance FTIR spectroscopy 45
  - 5.1.2 UV-Vis Spectrometry 46

5.2 Compounds of cobalt, HMTA and maleic acid compounds (AEEA004, AEEA005 and AEEA006) 47
5.2.1 Attenuated Total Reflectance FTIR spectroscopy 47
5.2.2 UV-Vis Spectrometry 48
5.3 Compounds of copper, HMTA and maleic acid compounds (AEEA007, AEEA008 and AEEA009) 49
5.3.1 Attenuated Total Reflectance FTIR spectroscopy 49
5.3.2 UV- Vis spectroscopy 50
5.4 Compounds synthetized by reflux (AEEA010, AEEA011 and AEEA012) 51
5.4.1 Attenuated Total Reflectance FTIR spectroscopy 51
5.4.2 UV- Vis spectroscopy 52
5.5 Compounds of manganese, 4,4-bipyridine and maleic acid (AEEP001) 53
5.5.1 Attenuated Total Reflectance FTIR spectroscopy 53
5.5.2 DRUV-Vis spectroscopy 54
5.5.3 X-Ray Powder Diffraction and Simulation of XRD patterns 55
5.6 Compounds of cobalt, 4,4-bipyridine and maleic acid (AEEP002) 62
5.6.1 Attenuated Total Reflectance FTIR spectroscopy 62
5.6.2 UV-Vis transmittance spectroscopy 63
5.6.3 X-Ray Powder Diffraction of Co-ma-bpy 63
5.7 Compounds of zinc, 4,4-bipyridine and maleic acid (AEEP003) 67
5.7.1 Attenuated Total Reflectance FTIR spectroscopy 67
5.7.2 Diffuse Reflectance UV-Vis Spectroscopy 68
5.7.3 X-Ray Diffractometry 69
5.8 Compounds of copper, 4,4-bipyridine and maleic acid (AEEP004) 72
5.8.1 Attenuated Total Reflectance FTIR spectroscopy 72
5.8.2 UV-Vis spectroscopy 74
5.8.3 X-Ray Diffractometry 74
5.9 Coordination Simulation 78
First coordination proposal 79
Second coordination proposal 80
Third and fourth coordination proposals 82
5.10 Absorption evaluation 86
5.11 Post-synthetic modification proposal by Diels Alder. 89
5.12 Photo-response modelling of referenced material. 90
CHAPTER VI: Conclusion and future work 92
References 94

Appendix I: COMPUTATIONAL INPUTS 99
    Orca Input examples 99
    Quantum Espresso Input examples 101

CHAPTER I: Introduction

Porous materials have been an attractive field for research in materials science for the promising applications for heat insulation, sound absorption, delivery and controlled release of substances, filtration, and storage of fluids and gases; through the years, new and sophisticated porous materials have been developed such as zeolites, metallic foams, carbon based porous materials, metal-organic frameworks (MOFs) and covalent organic frameworks (COFs).[1,2]

Reticular chemistry is the field of chemistry focused on the construction of reticular entities from building units, these entities have a periodic and well define array. Reticular chemistry initiated with the metal-organic frameworks as a porous material with better absorption properties than the zeolites; although, other compounds developed before as zeolites are included in the study field.[3]

MOFs are a kind of coordination polymer formed by metal ions and clusters as inorganic part linked by organic ligands; those materials can be designed with a very specific shape and size pore. The design of pore must consider the geometry coordination of metals and the ligand structure with the coordination sites. Although ligands can be design with a high accuracy by well-known reactions; the different coordination structures of metal ions introduce some uncertainty in the expected structure of molecular framework, this problem can be solved replacing the single metal nodes by secondary building subunits (SBUs), SUBs are metal complex which can provide more stability and increase the possible geometrical configuration for the framework.[2,4,5]

MOFs can form structures from 1D to 3D, but the pores can have structures from OD cage to 3D channels; MOFs with cavities which cannot let any guest molecule are considered frameworks with OD cages. The structure of pore and macro structure of MOFs definite the possible application of MOFs; MOFs have a huge branch of possible applications such as gas storage and separation, catalysis, controlled release, supercapacitors, molecular machines, biocompatible materials, and others. [6–8]

MOFs can be divided in three different generation, the first one is formed by MOFs with only structural applications in contrast, the third generation MOFs which are responsive materials; the third generation caught the attention of scientist by the possible applications in the industry introducing a specific behavior under certain conditions. Photo-responsive MOFs are part of the third generation, and those materials suffer reversible modifications, the photo response is a quantized mechanism, therefore each process need a radiation with specific wavelength. Those processes occurs in the organic molecules; the organic molecules can be part of the framework structure or a guest molecule.[9,10]

The materials modeling is a powerful technique which can provide information about the properties of materials, and it is very useful to design new materials; therefore, computational simulations let describe the possible behavior of material since microscopic view until a macroscopic environment.[11]

The modelling of MOFs can be made by programs which use Density Functional Theory (DFT) to solve and optimize the geometry of those materials; Orca and Quantum Espresso are programs usually used for geometrical optimization and for some material properties calculations. The computational methods can provide information of the possible behavior of MOFs, but in some cases graphical users interfaces (GUI) are needed to an easy interpretation of results, common GUIs are Xcrysden and Burai, also other programs as Mercury, Avogadro and Amsterdam Molecular Suit facilitate the extraction of information and the graphical modelling of materials.[12,13]

CHAPTER II: Problem Statement

The greenhouse gases are the main reason for world warming, which is one of the biggest problems that humans have because almost all their productive activities produce those gases principally carbon dioxide, and another big challenge for us is efficient water treatment. Many countries are worried about the consequences of those problems such as the increase of global temperature, melting of glacial poles, changes in the water and air currents which must lead to landslides, floods, storms, and other environmental catastrophes. The international community decided to take actions and in 2015 by the G20 group of United Nations Paris Agreement started, nowadays 189 countries are members of this agreement where the main goal is to maintain the global temperature increase very low, less than two degree Celsius, so all the countries need to develop strategies to support this goal. Ecuador is part of the Paris Agreement and by its constitution must protect the natural resources regarding the Ecuadorian industry has an organic environmental code which defines the vision of the industry in Ecuador and the Environment Ministry work with other institutions of state to assure the accomplishment of those agreements and laws.

Porous materials are a great possible solution for these problems and MOFs are the most promising materials because their permanent porosity and high specific surface let solid extraction of pollutants and separation and storage for those greenhouse gases produced by the industry, the modeling of those materials lets know the effectivity of materials in separations, diffusion, adsorption for CO_2 and pollutants and at the same time evaluate their photo response as a variable which could change the structure of the material network.

General Objective

- Synthesis and modeling of MOFs with different metallic ions (Co, Cu, Zn, and Mn) using hexamethylenetetramine (HMTA), 4,4 bipyridine, and maleic acid, and propose their possible photoresponsivity and carbon dioxide adsorption properties using computational methods.

Specific Objectives

- To synthesize MOFs with 4,4 bipyridine, hexamethylenetetramine (HTMA), and maleic acid as ligands and Co, Cu, Zn, and Mn as metallic ions by hydrothermal method.
- To determine the structure of synthetized compounds by XRD and determine the possible phases presented on each sample.
- To verify the functional groups of the MOFs (amine and acidic groups) by ATR-FTIR.

- To study how the crystalline structure of molecular frameworks formed.
- To study the CO_2 adsorption ability of synthetized MOFs.
- To model the photo response of MOFs with 4,4-bipyridine and maleic anhydride as ligands.

CHAPTER III: Background

3.1 Porous Materials

Porous Materials are basically any material that has voids, holes, channels, or any kind of pore. This property attracts attention from the scientific community because those materials have an internal surface area which a huge branch of possible applications. Nowadays many of those materials are synthesized in laboratories and others had been scaled to be produced by the industry. [1] The porous materials are represented in nature in a big diversity of things such as bones or tissues, fruits, rocks, and others; the natural processes for forming those materials helped to understand how to synthesize new designed porous materials. However, humanity was able to develop the porosity in new synthetical materials as in ceramics, bricks, clothing, and others; but nowadays the applications have been increasing at the same time as technology; and porous materials are required for heat insulation, sound absorption, delivery and controlled release of substances, filtration, and storage of fluids and gases.[1,14]

Porous solids normally formed by the action of a fluid which forms pores in a continuous solid phase, the fluid can be liquid or gaseous, but not all materials with pores should be called porous materials. These must have those two characteristics: possess several pores and the pores provide a specific performance to the material. In the synthetic porous materials normally the porous ones are designed with certain functionality and are considered as functional phase increasing the performance of the material. [14] They can be separated according to their porosity degree as low, middle, and high porosity; low and middle porosity material normally have closed pores. In the high porosity materials there are two cases based on the morphology of pores and solid phase; the first class are porous materials with a two-dimensional array of polygons and each pore is isolated from others, the cross-sectional geometry of those pores often is a triangle, quadrangle or hexagon, the last one produces a similar structure of the honeycomb and have the same name; in the same first case, Lotus-type porous materials have directional pores, and its shape is circular or elliptic producing less uniformity of pores distribution. [14]

The other case of porous materials presents a tridimensional array of pores and a reticulated structure, normally they are called three-dimensional reticulated framed materials. These materials have interconnected pores and open-cell structures. In the last case, these materials present a cell wall with pores which can have shapes like sphere, elliptical sphere, or polyhedron shape, these materials are also called bubblelike foamed materials.[14]

According to the precedence of porous materials, they can be classified as natural or artificial, but both have some characteristics attractive for engineering applications such as low relative density, large specific surface area, small thermal conductivity, good energy absorption, and high specific strength. Through the years, new porous materials have been developed and nowadays there are a huge number of known porous materials such as porous metals, porous ceramics, polymer foams, xerogels or aerogel, metallic foams, zeolites, silicas, carbon porous materials, periodic mesoporous organosilica (PMOS), metal-organic frameworks (MOFs) and covalent organic frameworks (COFs)[1,14,15]

3.2 Reticular Chemistry

The reticular chemistry is the branch of chemistry whose main purpose is to break and create new bonds configurated in a specific way, those bonds are strong to produce extended reticular structures of repetitive subunits or entities as molecules and clusters.[3] The materials studied in reticular chemistry are crystalline with a logical framework that could have a potential application based on the arrangement of building subunits. The reticular chemistry began bonding metallic ions with charged organic molecules, those were the first MOFs (Metal-Organic Framework), later other materials were developed as COFs (Covalent Organic Frameworks) and others included into the field while the reticular was developed such as COPs (Covalent Organic Polyhedra), MOPs (Metal-Organic Polyhedra) and ZIFs (Zeolite Imidazolate Frameworks). [2]

Reticular chemistry expands the field of coordination compounds with larger structures formed of geometrical and spatial specific arrangements of atoms on each building subunit. In this field chemists try to get a successful synthetic pathway to achieve a blueprint with a required molecular geometry and specific disposition of atomic units because those can determine the properties of the material. In organic chemistry, a compound with a specific conformation and configuration can be synthesized with a high level of precision and even functionalization of the complexes can be made by substitution or addition reactions. On the other hand, for metal complexes an uncertainty exists produced by the different geometries and coordination number that metallic ions can adopt, but in some cases can be despite using sophisticate multidentate ligands which can fix the metallic ions in a specific geometry and coordination. Furthermore, the reticular chemistry went forward by the synthesis of bigger structures where two main features are considered in synthesis: the first one is the kind of interaction and the directionality and how they can affect the final structure, the other one is the geometry and metric characteristics of molecular building units; both aspects are essential to synthesize extended crystalline structure and the first kind of that was metal organic frameworks (MOFs) using metallic ions and organic ligands.[2].

Reticular chemistry also is focused on the new characteristics of those porous materials based on the building units, their connectivity because the final material can present different properties than the building units, although this process carries to provide a possible application of those materials, researchers in this field are more interested in the way of synthesis and characteristics even without any application.[3]

On the other hand, those materials have unique properties never seen in other ones, so their scalability is another interesting field of research although the stability of those materials had been questioned. For example, COFs which are made from only organic molecules do not have great thermal stability or some MOFs synthesized have extraordinary properties but are unstable.

Before the stability required for a specific application should be evaluated for example for gas storage a high thermal stability is not necessary, so it is more important to determine what kind of stability, thermal, chemical, architectural, or mechanical is more important for a specific application; in this sense, many startups and BASF have commercialized MOFs and even the chemical company BASF was able to produce tons of those materials.[3]

3.3 MOFs

MOFs are hybrid inorganic-organic porous materials and crystalline polymeric compounds which are composed of organic ligands and metallic ions; those polymeric compounds are also defined as polynuclear metal clusters linked by organic ligands or bio-based molecules as bridges (Figure 1).[16,17] The versatility of those materials is one of their most attractive characteristics, this property is included by the huge number of organic ligands even designed ligands which have a specific proposal can be included inside the framework, regarding metallic ions which can be presented single, mixed, or as metallic clusters in the MOFs.[6,17] They are classified as a sub branch of coordination polymers by the IUPAC (2013) definition, those structures can be coordinated in 2D or 3D network-structures, this field was developed by Yaghi with carboxylate-based MOFs and by Kitagawa and coworkers with pyridyl-based compounds; nowadays the main objective is synthetizing MOFs with large pore apertures combined with large surface area.[18]

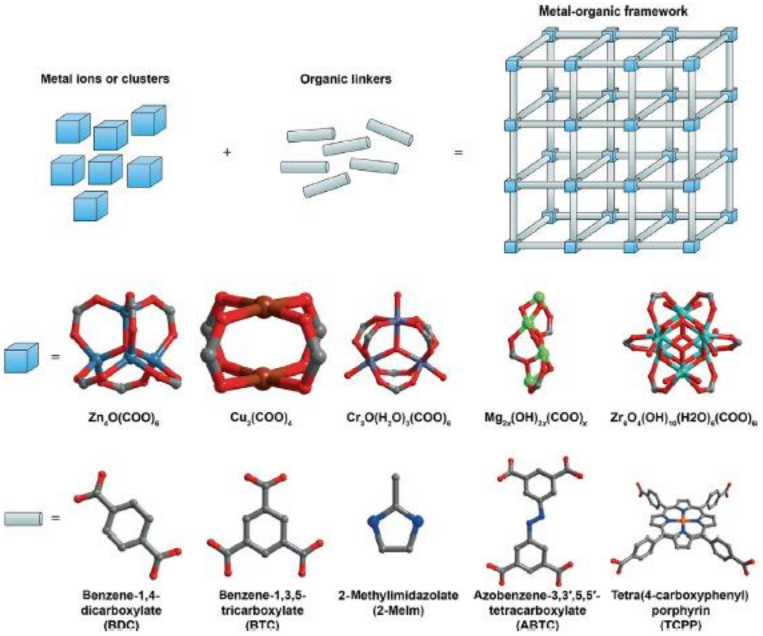

Figure 1. Scheme of basic components of Metal Organic Frameworks (MOFs)[19]

MOFs present the advantage of inorganic and organic porous materials, it means open-metal sites and functional groups,[6] but this duality of their nature also brings many attractive properties which characterize the MOFs such as high specific surface area (about 6000 m^2/g for some of them), ultrahigh permanent porosity which can reach 90% of their volume, and high tunable shape and pore size.[4,7,8]. In the earlier stage of MOFs, those characteristics made MOFs attractive for separation and storage of gases because MOFs presented better characteristics of sorption than aluminosilicate zeolites, also the regularity of the pores make them suitable for these applications; for example, in the storage of hydrogen or for separation of carbon dioxide from natural gas or fuel gas; another advantage of MOFs is the moderate cost and viability for bulky production of those materials. [8,15,20]

Furthermore, other applications were considered based on their versatility and designable structure; the size of the pores can be modified by changing the metals or ligands in the framework or considering specific conditions of reactions[7], the porosity can be designed letting to the guest molecules diffuse if they have a specific shape and- or size.[21] Additionally, other functionalities can be included in the pore zone with other kinds of modifications which can be classified in two groups as in situ modifications and post-synthetic modifications[8], those modifications let manipulate the structure of pores and active sites, and make MOFs interesting materials with properties as a catalyzer, ion exchanger, adsorbent, absorbent, and applications in energy storage, magnetism, luminescence, drug delivery, water treatment, sensor and others; although MOFs chemical stability should be considered because it is lower than in other ordered mesoporous materials.[15,16,21]

3.3.1 Structure of MOFs

MOFs are basically formed by two general parts or building units, one inorganic part with the metal ions or metallic clusters and a second part with the organic ligands. Regarding the inorganic part of MOFs single metal-ion nodes in the structure are less stable than polynuclear clusters which are called secondary building units (SBUs), the stability provided by SBUs is produced because chelation brings directionality and rigidity to the system and at the same time the charge of linkers helps to get uncharged material and increase the bond strength. MOF-2 is a great example of the stability achieved by the SBUs, in these case the synthesis carried out by vapor diffusion of trimethylamine/toluene mixture in a solution of benzene dicarboxylic acid (H_2BDC) and $Zn(NO_3)_2 \cdot 6H_2O$ with DMF/toluene as solvents; the formation of dimeric paddle wheel structures of $Zn_2(COO^-)_4$ as SBUs which are interconnected by BDC provide more rigidity and stability to form a neutral square grid structure (Figure 2), also these SBUs help to fix a permanent porosity because let retires all the solvent molecules without changes or collapses in the reticular structure increasing its suitability as gas adsorbent.[2,6,22]

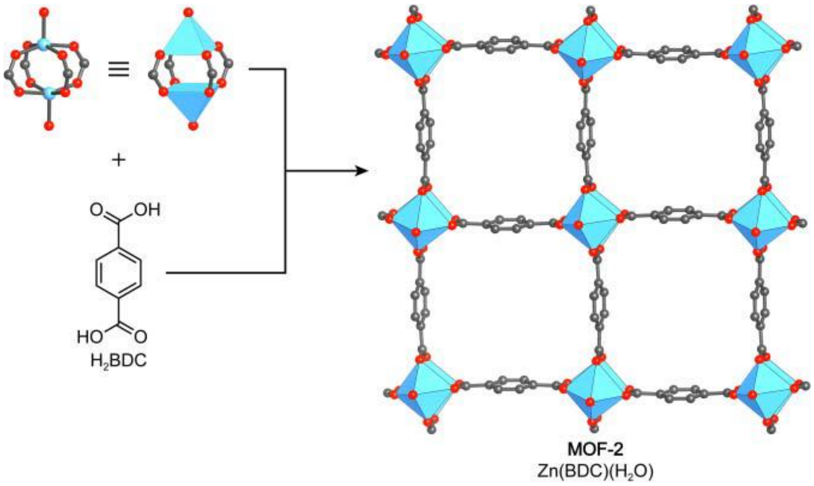

Figure 2. Crystal structure of MOF-2 across of a-axis, the polyhedron of metal clusters and H_2BDC are presented forming channels. [2]

the final structure of MOFs is defined by the linkage of SBUs and organic ligand which can be multidentate or designed to provide a specific size and form of pores. Although more interesting frameworks with more attractive properties can appear with the mixture of SUBs and organic ligand bridges achieving 2D and 3D MOFs. [2,22]

3.3.1.1 Organic Linkers

Organic linkers can modify the structure of MOFs and acts as bridges between the metal ions of SBUs, in the early stage of MOFs bipyridines and nitriles were the most used linkers considering their neutral charge although it brings some problems by their many drawbacks; therefore other organic linkers were introduced as the carboxylates-based linkers which can provide a better stability of framework because can neutralize the positive charge of metal ions and allow neutral MOFs with the requirement of counter ions others advantage of getting carboxylate-based linkers are: the strength of the bond between the linkers and SBUs increase the chemical, the thermal and mechanical stability of MOFs and carboxylates improve the formation of polynuclear metallic clusters with connectivity and geometry fixed. [2,5]

The strength of bonds between the linkers and metals can define the ability of crystallization by a directly proportional relation as is shown in Figure 3. MOFs synthesis normally have very symmetrical linkers independent of their nature as bases or acids, regarding the number of extension points which can be since two to twelve points, they can be classified as ditopic, tritopic, tretratopic, exatopic, octatopic, and dodecatopic (Figure 4) as the most common structure of organic linkers used in MOFs synthesis.[2]

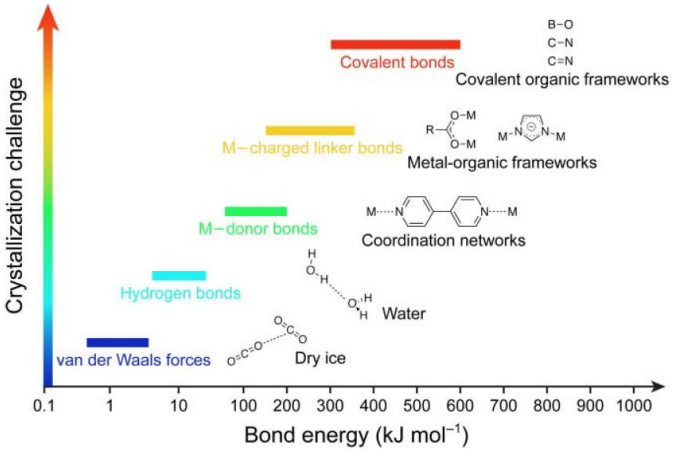

Figure 3 Relation between the bond energy and the ability of cristallization[2]

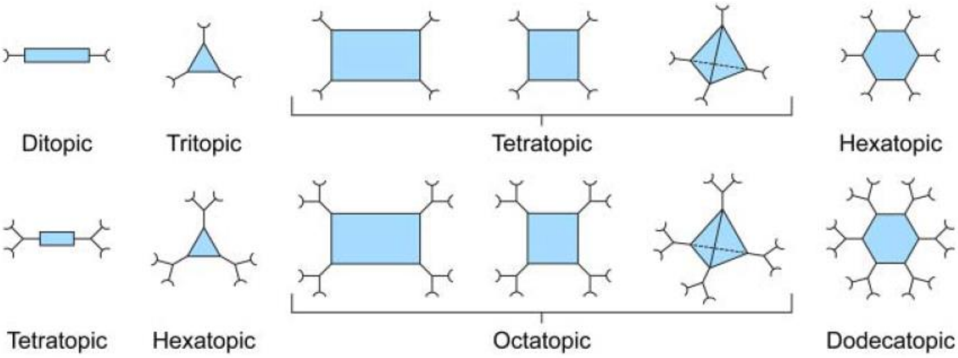

Figure 4. Basic geometries normally used in MOFs [2]

3.3.1.2 Single metal-ion nodes and Secondary Building Units

In the early stage of MOFs, the single metal-ion nodes were the main inorganic part of those molecular frameworks. The preferred metals used by the synthesis of MOFs are transition metal by their high coordination capability; those nodes can introduce some uncertainty in the coordination and that can affect the permanent porosity. The single metal nodes have a limited coordination sites, octahedral is the most common coordination geometry of d-block transition metal nodes, although linear and tetrahedral coordination can be presented; the limit of coordination sites is attributed to lanthanide f-block cations with higher coordination numbers between 8 to 12. Other via to achieve higher coordination sites is use metallic clusters which normally are formed from d-block transition metals, those complex inorganic parts are referred as secondary building units.[23]

Secondary building units are inorganic building units, usually cluster entities, those entities are formed by metal ions linked by organic ligands or other atoms by covalent bonds; the main characteristic of SBUs is the ligand and metal coordination modes of their structure can be used to form a extended reticular networks using polytopic ligands. SBUs can present many geometries such as octahedral, trigonal prism, square planar, square paddle wheel, and triangle (Figure 5); those geometries are defined by the coordination number and geometry of metal ions and the functional groups immersed in the structure, where linkers react with vacant or labile sites of metal ions, normally ligands are ditopic, tritopic or multitopic linkers. [2,6,22,24]

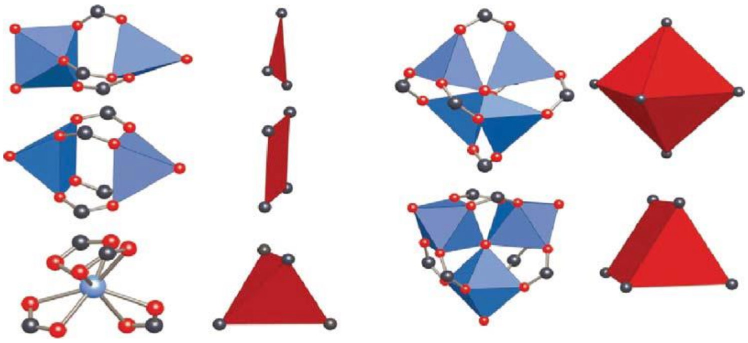

Figure 5. Examples of inorganic SBUs: (a) triangle, (b) square planar, (c) tetrahedron, (d) octahedron, and (e) trigonal prism.[6]

SBUs provide high crystallinity to the MOFs; actually, the macrostructure of MOFs is a consequence of the connectivity, and in this way, SBUs let access to large variety of framework structures because SBUs increase the coordination sites and define well their geometry. The rigidity and specific geometry of SBUs facilitate the synthetic of MOFs providing stability to the framework. Also, SBUs are useful to predict the topology of MOFs reducing the possibilities of geometrical configurations of resulting nets because both SUBs and organic ligands has geometrical constraints regarding of the coordination sites.[2,25]

3.3.2 Architecture of Networks and Porous Structures

MOFs are formed of a network of pores; the metals, SBUs, and organics ligands define the properties of pores and therefore the structure and arrangement of pores in the framework too. The arrangement of the building units of MOFs define the architecture of the framework from 1D until 3D structures; MOFs can present channel in one direction or a complex framework of interconnected channels. Those frameworks can have very complex structure considering advanced functional or responsive MOFs such as interpenetrating MOFs, but to distinguish the basic frameworks in the Figure 6 some schematic examples are sketched. [6,26]

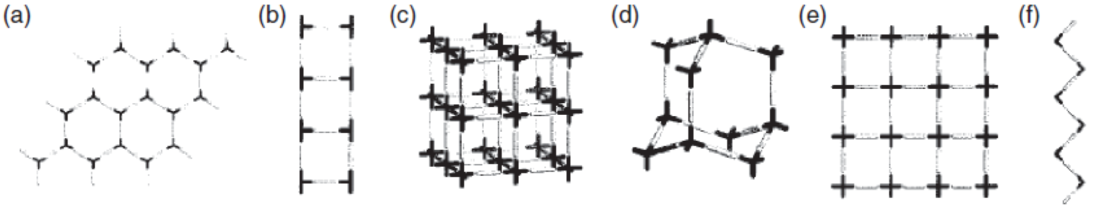

Figure 6. Representation of basic frameworks. a) honeycomb (2D), b) ladder (1D), c) hexagonal diamondoid (3D), d)square grid (2D), e) square grid (2D) and e) zigzag chain. [6]

Although the frameworks can adopt from 1D to 3D structures, the porous structures can be from OD to 3D structures. MOFs with too small cavities that are not able to admit any guest molecules are referred as solids without windows or with narrow windows; in this case, MOFs are formed by 0D cages. The 1D channels are defined as pores with enough size to admit a gust molecule inside, those pores are repeated infinitely in one dimension.[6]

There many MOFs constituted by 2D layers, in this case the pores are extended in two dimensions forming reticular layers, but those layers are not interconnected between them; there are two kinds of those sheets the first one formed by zigzag chains and the second one by straight chains as is shown in Figure 6 d) and e) respectively. MOFs with high porosity normally have 3D channels which are formed by interconnected 1D channels along the three dimensions, those MOFs are the most promising MOFs for possible applications in the industry; a simple scheme of that kind of MOFs is shown in Figure 6 c). [6]

3.4 Synthetic Methods of MOFs

MOFs have several synthetic pathways; the synthetic technique is selected depending on the many factor which can determine the formation facility and the stability of components under certain conditions. The factors which can influence the self- assembly of MOFs are the nature of ligands and metal ions or SBUs, the solvent, pH, steric hindrances, counterion requirements, temperature and the ratio of metal and ligand.[6]

All the synthetic routes have a main propose which is produce high quality of single crystals; although, in the early stages those protocols are for small scales. The most known synthetic ways are: solvothermal/hydrothermal synthesis, solvent-evaporation synthesis, diffusion synthesis, sonochemical, electrochemical, microwave assisted, mechanochemical, ionothermal, and high-throughput synthesis. In small scales, MOFs are synthetized by solvothermal/hydrothermal synthesis with electrical heating.[6,16]

3.4.1 Hydrothermal Synthesis

Hydrothermal synthesis is the most common synthetic way for MOFs in small scale (Figure 7); this protocol uses the reagents dissolved in hot water under high pressure, to manage the high-pressure conditions an autoclave is needed. The temperature range used in this kind of reactions is from 60 °C to 260 °C. This method used a temperature gradient, the hot stage let the dissolution of reagents and the cooling stage let the formation of seeds and growth of crystals. The next stages after synthesis are important too, the washing and drying of the compounds can affect the crystallization, therefore a slow evaporation of solvent and vacuum drying are preferred to get a high quality crystals.[6,16] Also, related with the synthesis steps, post-synthetic modifications can introduce new functionalities to the frameworks or even modify the macro structure of MOFs.[2]

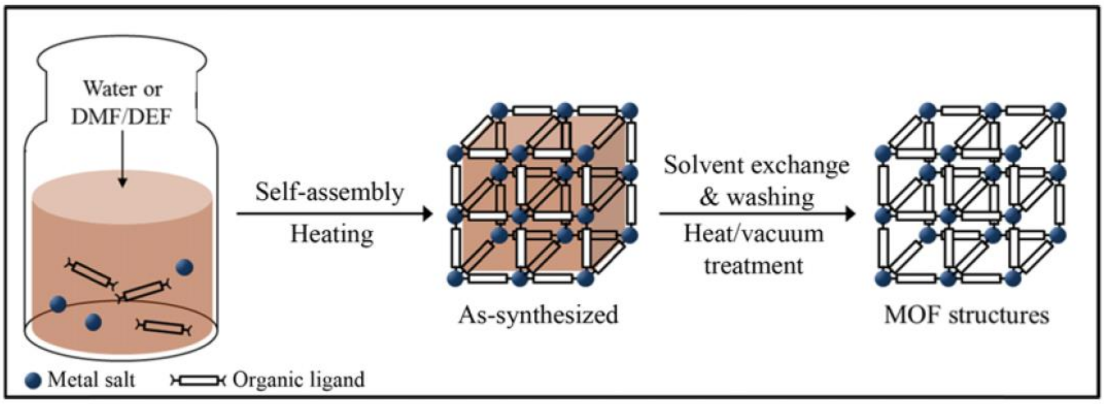

Figure 7. Conventional solvothermal/hydrothermal synthesis of MOFs.[16]

As result of the temperature gradient in a closed system, the pressure has a variation too; those variations create different environments which promote the formation of specific compound which can be stable on those conditions. The kinetic and thermodynamic compounds are in constant competition and the changes in the synthesis environment can change the formation quantities of each one; the main difference is that in certain conditions, some compounds have a higher velocity of formation (kinetic compounds), so in the beginning and short time lapse the kinetic compounds are formed in higher amounts that thermodynamic compounds, but if the reaction is not stopped those compounds will disappeared and let the formation of the most stable compounds with lower formation speed at those conditions (thermodynamic compounds); this equilibrium is reversible and the formation of each one can be controlled. In the hydrothermal synthesis in MOFs some kinetic compounds can appear, but the main propose of those synthetic protocol is achieving a thermodynamically controlled reaction.[27]

3.5 Stimuli-Responsive Materials

The materials which change their chemical or physical properties after the exposition to a stimulus (pH, temperature, pressure, radiation, etc.) are considered as responsive materials, and the interest in their study increase by the possible applications especially in the nano and biotechnology because this kind of materials could provide the remote control of these materials on the required intensity even in biocompatible materials used in drug delivery and tissue engineering. The design and engineering of polymers have been worried to develop new materials with this responsive behavior because those can increase the efficiency on many processes in the industry. [28]

3.5.1 Responsive MOFs

MOFs normally are used as passive materials for storage and separation of substances, but those materials are one of the most promising functional materials by their versatility and the possibility of introducing controlled and reversible transformations under certain conditions as molecular switches, these conditions can include stimulus as light, guest molecules, pressure, temperature, or changes in pH. These dynamic frameworks can be achieved by designing the organic ligands, SBUs, topology, and post-synthetic modifications of MOFs, normally the result of the stimuli is a reorganization of molecular and electronic structure. [9,29,30]

MOFs with reversible response under certain stimulus are also called the third generation MOFs or soft porous crystals, the main goal in these materials is achieving high specificity of the target molecules normally for stimuli-responsive applications; the understanding of structural changes or phase transitions which can be measured by its measurable physiochemical properties based on its sensitivity and response speed. [9]

3.5.2 Photo-responsive MOFs

Photo-responsive MOFs are a kind of third generation MOFs, those material respond to electromagnetic radiation stimulus with a structural reorganization, that kind of MOFs are considering as soft porous crystal. The photo-response can produce reversible discrete states of MOFs with very interesting applications for gas separation and storage, photo-chemical switches, polymer-enzyme switches, and molecular machines. The photo-response is produced by a photochromic compound; in this case, those compounds are the organic ligands which can experiment electronic and molecular structure changes. The photochromic moieties can be a framework backbone, side group or a guest molecule as is shown in Figure 8.[31–33]

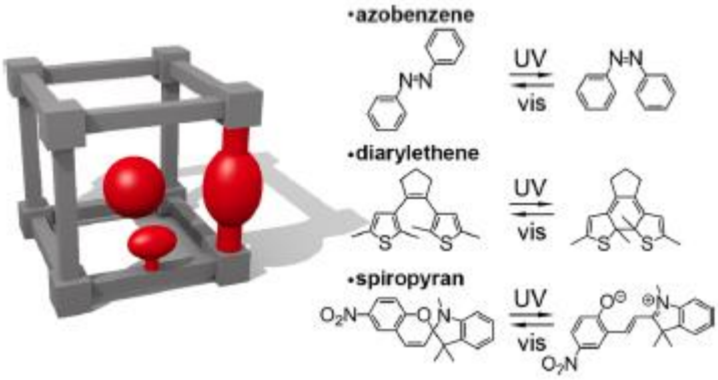

Figure 8. Scheme of photochromic moieties in the pore structure. a) framework backbone, b) side group, c) guest molecule.[33]

Photo-responsible MOFs depending on the nature of ligand and its function can produce isomerization as the azobencenes, topological changes and even more sophisticated behavior as molecular switches in the case of diarylethene and spiropyrans (Figure 9). On the other hand, the irradiation with UV radiation can induce the degradation of MOFs, so this property should be evaluated carefully.[33]

3.6 Referenced materials.

There are two reported materials which were the base for the proposed materials in this work. The first one was synthetized by Marylin Quintero and Edward Avila, this material was a MOF with Cu (II) as metallic ion, while maleic anhydride and 4,4-bipyridine as ligands; the Cu (II) ions has an octahedral coordination with 4,4-bipyridines in axial positions and four maleic anhydrides in the perpendicular plane. This material was elucidated by XRD, this structure provide suitable conditions to propose a photo reactive behavior by the dimerization of maleic anhydride; the coordination of Cu(II) is showed in Figure 9 [34]. This material has synthetized by hydrothermal synthesis, the maleic anhydride in the coordination sphere was obtained from maleic acid as result of the equilibrium of the acid in the synthesis conditions. Although this material was elucidated completely by XRD analysis, any application was studied or reported. In the present work computational simulations were carried out to stablish the properties as absorbent and its photo reactivity.

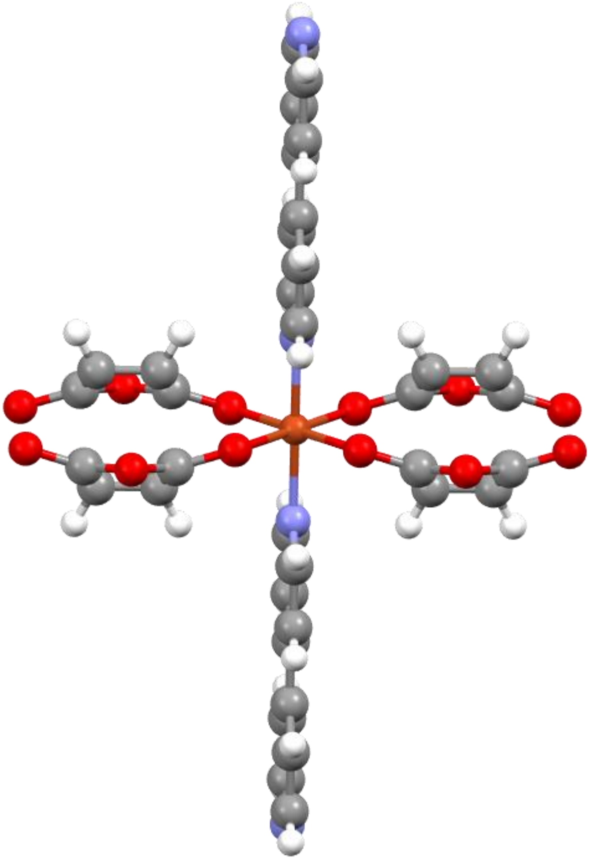

Figure 9. Symmetric unit of coordination polymer reported by Marylin Quintero and Edward Avila.[34]

The second material was reported by Patricia Mendoza in 2016 as result of her master thesis project, this work used Co (II) as metallic ion, while phthalic acid and 4,4-bipyridine as ligands. The Co (II) has as octahedral coordination with two 4.4-bipyridines in axial positions and four phthalic acids in the perpendicular plane as is shown in Figure 10. The main application evaluated for this material was the ionic interchange, but any application in adsorption was reported.[35] Both materials were synthetized in similar conditions by hydrothermal method and those conditions were used to stablish the synthetic conditions in this work.

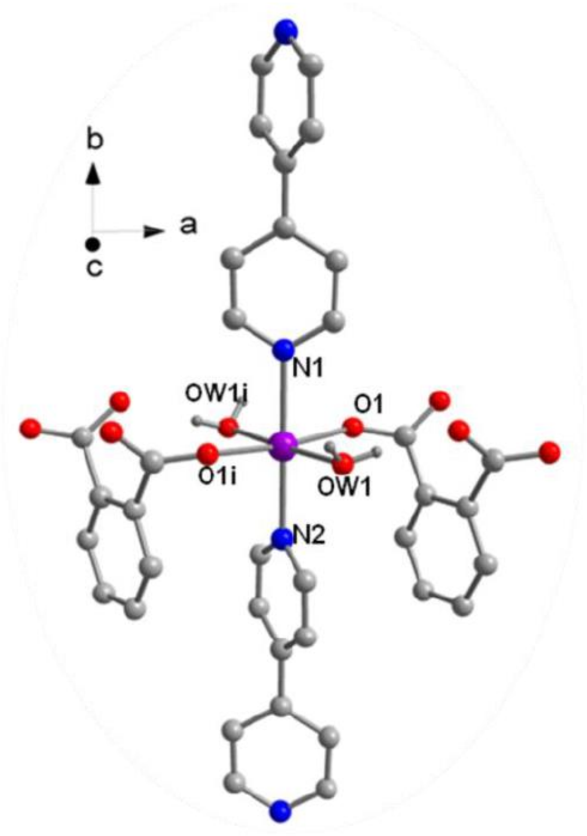

Figure 10. Symmetric unit of coordination polymer reported by Patricia Mendoza in 2016.[35]

CHAPTER IV: Methodology

4.1 Synthesis of MOFs

In the presented work, molecular organic frameworks were synthesized by two methods: hydrothermal synthesis and synthesis by reflux. Hydrothermal is one of the most used methods for the synthesis of MOFs, in this case, the compounds were prepared with maleic acid, hexamethylenetetramine, and 4,4-bipyridine and salts of cobalt, copper, manganese, and zinc.

The reflux method was considered as a suitable option for synthesis because hydrothermal synthesis carried out in vials in some cases has leaked of water, so this procedure although let to achieve less pressure maintain the temperature and pressure relatively stable.

4.1.1 Materials and reagents

The materials used in the synthesis pathway are the following: hot plate, 20 ml vials of borosilicate (Glassco brand), analytical balance, 50 ml round-bottomed flasks, 100 ml beakers, condenser, micro spatula, plastic film, 10ml syringe, stove, Eppendorf tubes, Teflon container and autoclave.

The reagents used in synthesis were: hexamethylenetetramine (HMTA), maleic acid, 4,4-bipyridine, distilled water, copper (II) chloride ($CuCl_2 \cdot 2H_2O$), cobalt (II) nitrate ($Co(NO_3)_2 \cdot 6H_2O$), manganese (II) chloride ($MnCl_2 \cdot 4H_2O$) and zinc (II) nitrate ($Zn(NO_3)_2 \cdot 6H_2O$).

4.2 Experimental procedures

The experimental procedure was divided into three stages and each one had a previous stage where the synthetic variables were tested with distilled water, those stages were the result of the reagents and materials available at this moment and the restrictions in all Ecuador to prevent the propagation of COVID-19.

4.2.1 First Stage (Hydrothermal Synthesis)

In this stage the first step was testing the 20 ml vials with distilled water, three vials with their respective flaps were filled with 10 ml of distilled water (half of the capacity approximately) and submitted 120°C on the stove for three days (only one flask was impermeable), then some combinations of cardboard, plastic film, rigid plastic, Foamex, and Teflon tape were tested to improve the impermeability of vials; the Teflon tape only was used in the vial thread, but the others were used to made insulating seals as is shown in Table 1.

Table 1.. Permeability test of different configuration of seals.

Seal combination	**Teflon on thread**	**Impermeability achieved**
Without seal	No	No
Cardboard + plastic film	No	No
Cardboard + foamix + plastic film	No	No
Rigid plastic+ foamix + plastic film	No	No
Without seal	Yes	Only in one
Cardboard + plastic film	Yes	No
Cardboard + foamix + plastic film	Yes	In both
Rigid plastic+ foamix + plastic film	Yes	Only in one

Each seal combination was tested with two vials with 10 ml of distilled water at 120°C on the stove for three days, the impermeable seals were built as is shown in the Figure 11. For each synthesis, a new seal was required for each flask.

The reagents were weighed in an analytical balance, the calculus of amounts of each reagent was based on the molar relation between metallic salt, maleic acid, and hexamethylenetetramine respectively, in this stage the molar relations tested was 1:1:1, 1:1:0.5, 1:1:0.25 as is shown in Table 2; it is important to note in this stage only the following salts were used: copper (II) chloride ($CuCl_2$), cobalt (II) nitrate ($Co(NO_3)_2 \cdot 6H_2O$), manganese (II) chloride ($MnCl_2 \cdot 4H_2O$). After weighing the reagents, each one was deposited in its respective vial, filled with 10 ml of distilled water, and reagents dissolved, finally, each flask was sealed and heated in the stove at 120°C for 72 hours.

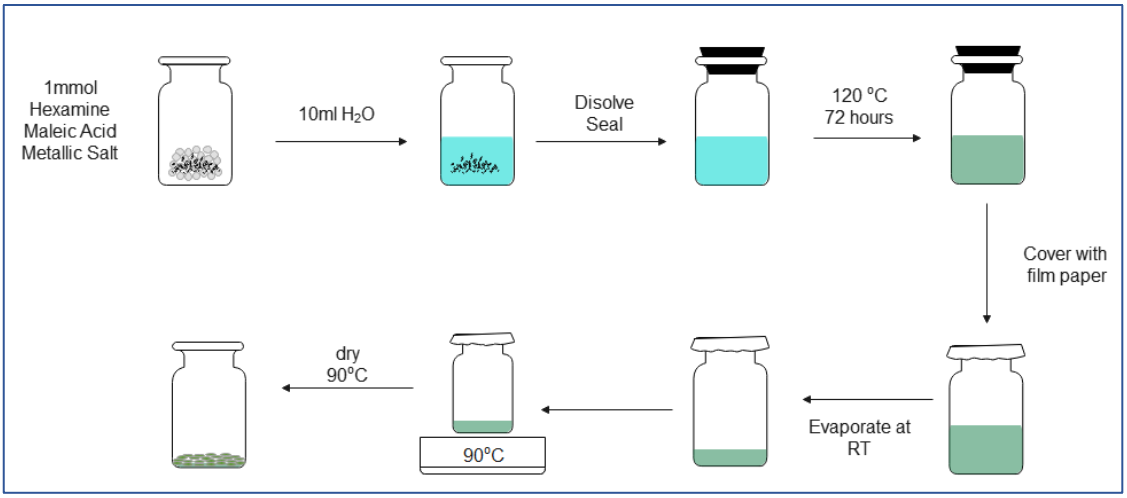

Figure 11. Scheme of processes performed in the first stage of synthesis.

All the process is shown in Figure 11, but to prevent reagent waste for a possible leak of water, MOFs were synthesized metal by metal and the sample was repeated when the flasks presented water leaked and that sample has an (*) in its label as is shown in Table 2.

Table 2. Amounts of reagents used in each MOF synthetized in the first stage of synthesis.

Code	**Metal**	**m_{salt}/g**	**n_{salt}/mmol**	**m_{ac}/g**	**n_{ac}/mmol**	**m_{hex}/g**	**n_{hex}/mmol**
AEEA001	Mn	0.0905	0.45728	0.1660	1.43005	0.1360	0.97014
AEEA001*	Mn	0.1972	0.99641	0.1213	1.04497	0.1404	1.00153
AEEA002	Mn	0.0907	0.45829	0.1209	1.04152	0.0701	0.50005
AEEA002*	Mn	0.1980	1.00045	0.1216	1.04755	0.0704	0.50219
AEEA003	Mn	0.0905	0.45728	0.1191	1.02602	0.0350	0.24967
AEEA004	Co	0.2892	0.99371	0.1197	1.03119	0.1408	0.92255
AEEA005	Co	0.2861	0.98306	0.1204	1.03722	0.0703	0.46062
AEEA005*	Co	0.2855	0.98099	0.1201	1.03463	0.0692	0.45341
AEEA006	Co	0.2890	0.99302	0.1191	1.02602	0.0352	0.23064
AEEA007	Cu	0.1338	0.99516	0.1217	1.04841	0.1402	1.00009
AEEA007*	Cu	0.1344	0.99665	0.1206	1.03894	0.1400	0.99867
AEEA008	Cu	0.1350	1.00409	0.1203	1.03635	0.0698	0.49791
AEEA008*	Cu	0.1340	0.99665	0.1206	1.03894	0.0703	0.50148
AEEA009	Cu	0.1343	0.99888	0.1218	1.04928	0.035	0.24967

After the synthesis of MOFs, all the flasks were covered with plastic film with small holes to let evaporation and to prevent contamination with dust, the flasks rested for nine months in those conditions than was dried at 90°C, after that when the humidity was not visible all samples were dried at 40°C and -20 psi in a vacuum stove for four days.

4.2.2 Second Stage (Reflux Conditions)

In the second stage, the MOFs were synthesized by a reflux synthetic pathway, in this case, all the reagents were weighed and deposited in a bottom rounded flask with 30 ml of water, the amounts of each reagent are tabulated in Table 3; then all reagents were dissolved and the reflux system was assembled as is shown in Figure 12, the condenser was capping with a balloon trying to maintain constant pressure in the system.

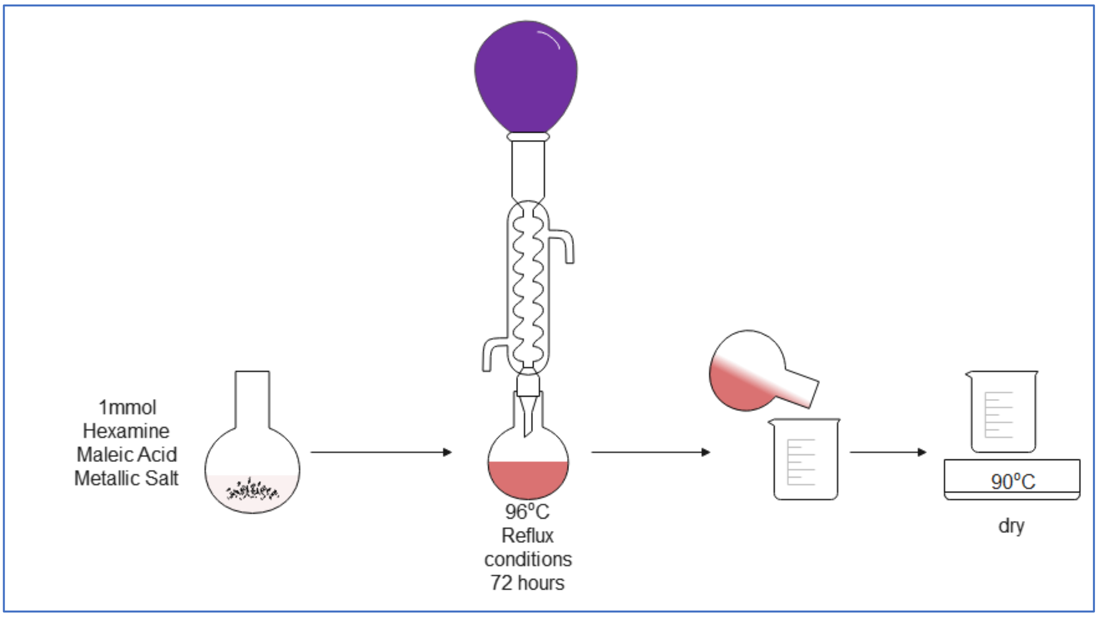

Figure 12. Scheme of processes performed in the second stage of synthesis.

To achieve the reflux conditions the equipment was calibrated using distilled water until the temperature was fixed at 96°C preventing the boiling of the solution. Another important point in this stage is that only manganese, cobalt, and zinc salts were used.

Table 3. Amounts of reagents used in each MOF synthesized in the second stage of synthesis.

Code	**Metal**	**m_{salt}/g**	**n_{salt}/mmol**	**m_{ac}/g**	**n_{ac}/mmol**	**m_{hex}/g**	**n_{hex}/mmol**
AEEA010	Mn	0.3958	1.999899	0.2475	2.13215	0.2799	1.996633
AEEA011	Co	0.5832	2.003917	0.2414	2.07960	0.2797	1.995206
AEEA012	Zn	0.5923	1.990924	0.2444	2.10545	0.2800	1.997346

The samples were transferred to beaker flasks of 50 ml and concentered until 10 ml at 90°C before covering them with plastic film with small holes, then the samples were stored at room conditions to let natural evaporation and crystallization of MOFs. After that, the samples were dried at 40°C and -20 psi of pressure for four days.

First and second were carried out before the pandemic emergency; during the sanitary emergency, the changes in each sample were not registered, although the samples remained in the laboratory some environmental changes were not recorded and variations in temperature of those months were not considered. Also, in both stages, a vacuum drying phase was required to extract all the water from the MOFs, because those compounds have a very hygroscopic behavior and only can stay few seconds completely dried.

4.2.3 Third Stage (Hydrothermal Synthesis)

In the third stage, the amine used was 4,4 bipyridine, in the first phase of this stage the procedure of the first stage was replicated but with many problems of leaking water in the vials. The problem was solved with an autoclave reactor that was mainly composed of two parts an inner silicon flask and a metallic hermetic flask, this reactor let work in hermetic conditions with constant pressure and without any risk of water leaking.

The reagents were weighed according to a molar proportion of 1:1:1 between slat, amine, and acid; also, the amounts were fixed to the new volume of the solution resulting in three millimoles of each reagent as is shown in Table 4, in this stage there was only one autoclave and the reactions of MOFs synthesis must be carried out sequentially in this of order manganese, cobalt, copper, and zinc.

Table 4. Amounts of reagents used in each MOF synthesized in the third stage of synthesis.

Code	Metal	m_{salt}/g	n_{salt}/mmol	m_{ac}/g	n_{ac}/mmol	m_{bpy}/g	n_{bpy}/mmol
AEEP001	Mn	0.5940	3.001364	0.3518	3.030669	0.4688	3.071681
AEEP002	Co	0.8786	3.018933	0.3550	3.058236	0.4619	3.026471
AEEP003	Cu	0.5110	2.997419	0.3565	3.071158	0.4618	3.025816
AEEP004	Zn	0.8935	3.00326	0.3491	3.007409	0.4595	3.010746

After the reagents of each sample were weighed, the reagents were deposited in the silicon flask and 40 ml of distilled water was added, the flask was sealed and shaken to dissolve all the reagents, it could take some minutes. Then the silicon flask was placed inside the metallic flask and hermetically sealed, the silicon flask has a capacity of 100 ml, but the solutions only have 40 ml to prevent an excess of pressure in the system and by the existing amount of 4,4 bipyridine.

The autoclave was placed inside the stove at 120 °C for 72 hours as is shown in Figure 13 and then was cooled at room temperature for six hours before it was opened. After the autoclave was opened, the sample was deposited in a beaker and cover with plastic film. Each sample was divided into two portions the first one of 10ml was dried at 90 °C and the second fraction of 30 ml was concentrated at room temperature for fifteen days. After the fifteen days, the second fraction was dried at 90 °C and stored in vial flasks.

In the case of copper and manganese before this step, the precipitates were filtered and dried at 90°C and stored in sealed vial flasks. After the synthesis and normal drying in the stove of the samples, all samples were dried at 40 °C and -20 psi of pressure in a vacuum stove.

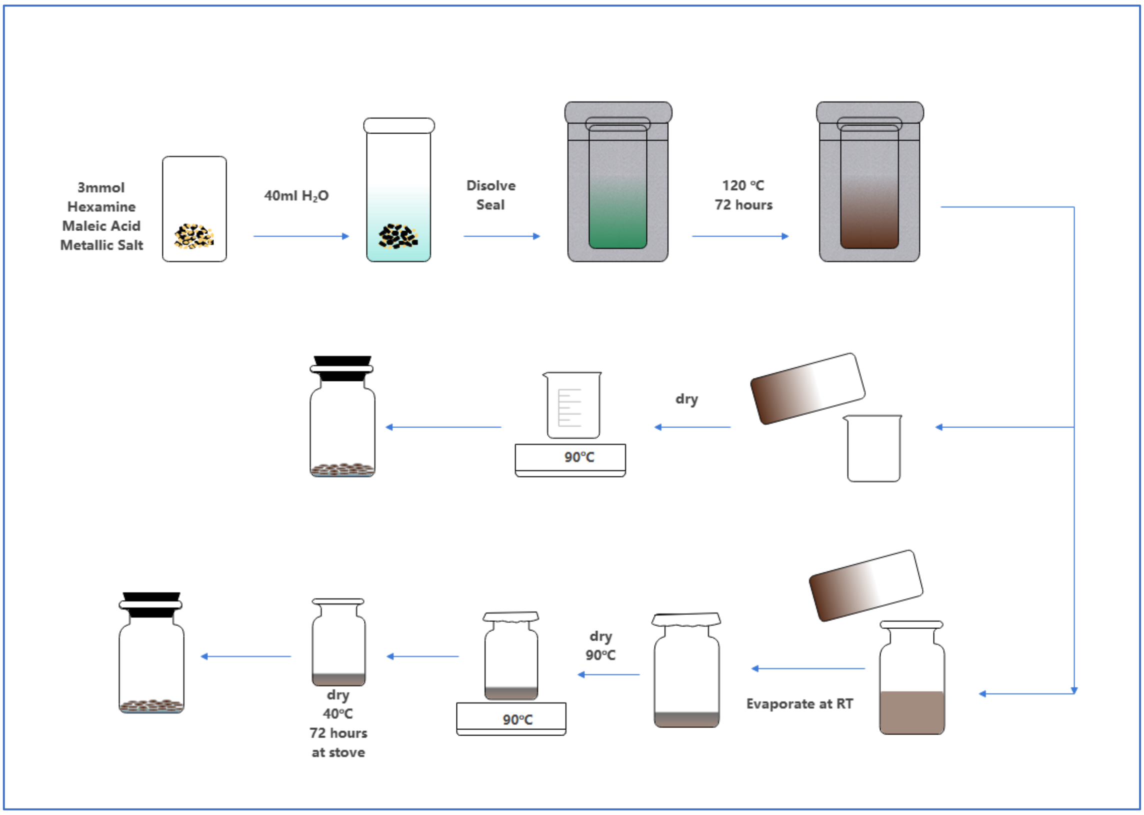

Figure 13.Scheme of processes performed in the third stage of synthesis.

Some samples in the three stages needed a second third phase of drying which was carried out at 40°C and -20 PSI for four days and rapidly sealed to prevent any hydration of the MOFs and only open for the characterization of the materials.

4.3 Characterization Techniques

The characterization techniques used to elucidate the compounds synthetized were Attenuated Total Reflection FTIR Spectroscopy (ATR-FTIR), Diffuse Reflectance UV-Vis Spectroscopy (DRS-UV-Vis) and X-Ray Diffractometry (XRD).

The synthetized materials can be separated in two groups the first one is composed by the samples from the first and second stage of synthesis and the second one by the compounds from the third stage of synthesis. The first group was elucidated only by ATR-FTIR and DRS-UV-Vis, because hygroscopic behavior of the sample from this group. On the other hand, the second group was able to dry and prepare for the XRD and ATR-FTIR and DRS-UV-Vis too.

4.3.1 Attenuated Total Reflection FTIR Spectroscopy

There are many compounds with covalent bonds which can absorb electromagnetic radiation from the infrared region. The principle of this characterization technique is based on the absorption of infrared radiation by the molecules producing the vibration of bonds, the vibrational range in the infrared is described between wavelengths from 2.5 μm to 25μm; the chemists usually use the wavenumber ($4000cm^{-1}$ to $400cm^{-1}$) rather than wavelength units[36].

The absorption of infrared radiation is a quantized process; the molecules only absorb a specific energy, the energetic changes registered in the IR spectrum correspond to the order of 8-40kJ/mole. The Infrared spectroscopy has two types of spectrometers, Disperse and Fourier Transform (FT-IR) instruments, but better and faster IR spectra are produced by FT-IR spectrometers.[36,37]

The reflection techniques for FT-IR can be Attenuated Total Reflection FT-IR spectrometry (ATR-FTIR) and Diffuse Reflectance FT-IR spectroscopy (DRIFTS). ATR-FTIR is the most common implemented technique used for organic and inorganic compounds; this technique needs a crystal with excellent properties of IR transmission and high refractive index. A monochromator select the beams with a specific wavelength, the IR beam irradiate the sample with greater angle than the critical angle to produce a complete refraction until the detector as is shown in Figure 14.[36,38,39]

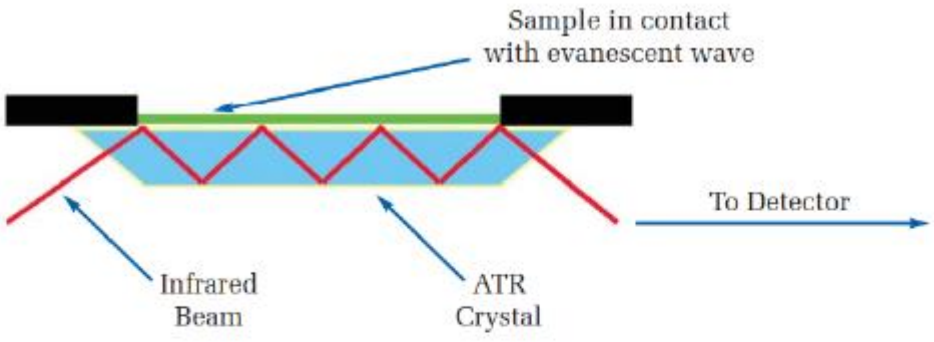

Figure 14. Simple scheme ATR-FTIR measurement in plane [111].

In the present work the IR spectra of the sample was measured by an Agilent FTIR cary 630 spectrometers, this equipment has a single reflection diamond for attenuated total reflection (ATR); the measurement rage for all spectra was from 4000cm^{-1} to 400 cm^{-1}.

4.3.3 Diffuse Reflectance UV-Vis Spectroscopy

In UV-Vis spectroscopy molecules absorb electromagnetic radiation in the ultraviolet and visible range (190 nm – 200 nm), the absorption is related with electronic and vibrational transitions; those electronic transitions normally occurs between a lower energy level and a higher energy level, normally, the electrons are promoted from the highest occupied molecular orbital (HOMO) to the lowest unoccupied molecular orbital (LUMO). [36,40]

Uv-Vis spectroscopy has two selection rules; spin selection rule stablish that changes in the spin multiplicity are forbidden electronic transitions; on the other hand, Laporte selection rule only allow electronic transition with a change in the parity of energy states. The application of UV-Vis spectrometry is limited for organic compounds because many of them do not present any coloration and the absorption only occurs in UV region, but the in MOFs, the metal ions normally absorbs in the visible region. The electronic transitions in the transition’s metals are d-d electronic transitions, those transition are forbidden by Laporte selection rule; therefore, its intensity is low in comparison with the absorptions from organic ligands in UV region. In metallic complex the maximum wavelength absorbed can be tuned by the ligands in the coordination sphere; the ligand field theory explains this behavior, this theory considering the nature of metal and ligands as the main factors that affect the configuration of the crystalline field and introduce the sigma and pi contributions. The ligands which can reduce the energy difference between molecular orbitals (crystal field) are called high spin or weak field ligand in contrast with the ligand which can increase the energetic difference that are called low spin or strong field ligands; this changes in the crystal field are reflected in the UV-Vis spectra and could analyzed by a Tanabe Sugano diagram when the electronic transitions are spin allowed.[5,36,41]

Diffuse reflectance spectroscopy (DRS) uses special cells and detectors arrays to detect the radiation reflected in all directions by the particles, this technique is normally used for solid samples which are crushed until form a powder; a simple scheme of a DRS equipment is sown in One important advantage of the UV-Vis-DRS is that this technique is nondestructive.[36,42,43]

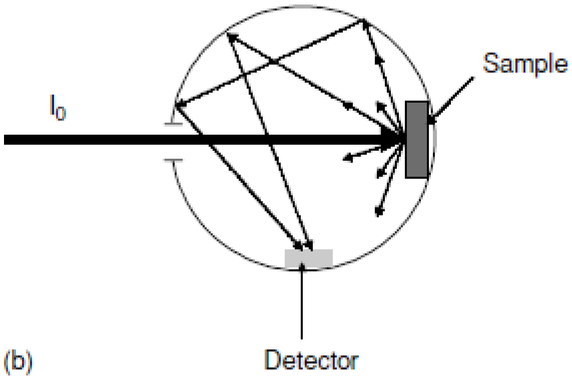

Figure 15. Scheme of an experimental arrangement in a UV-Vis-DRS equipment.[43]

In the present work the UV-Vis spectra of samples were measured by an UV/Vis/NIR, PerkinElmer Lambda 1050 spectrophotometer equipped with deuterium and tungsten lamps and a photomultiplier detector R6872, the Praying Mantis module was used for dried solid samples (third stage compounds). The spectra were measured in the range of 380 nm to 800 nm.

4.3.3 X-Ray Powder Diffraction Spectroscopy

X-ray diffraction spectroscopy is the most important characterization technique for MOFs, because this technique can elucidate the crystalline structure of the molecular framework. The X-Rays used in the diffraction are in the range of 0.5-2.5 Å of wavelengths; the x-rays are produced when the source element is charge with enough kinetic energy and immediately deaccelerated. X-ray sources can use different metal, and for a suitable diffractometry the metals in the sample should be considered because d-transition metals can produce x-rays with the similar wavelength of the x-ray sources and that produce noise in the diffractogram. [20,44,45]

X-ray powder diffraction spectroscopy is based on reflection geometry between x-ray source and detector as is shown in Figure 16. The Bragg-Bertano kind of diffractometer irradiate the sample with help of divergence slit until the beam achieve the sample and then the refraction beam is focused until the detector. This technique is based on the Braggs' law and for a polycrystalline sample, the goal is capture all possible orientation of the sample with the minimum change in the relative orientation of sample, this kind of XRD is faster, but have some limitations such as less accuracy than single crystal techniques, multiphase sample are difficult to solve and the preferred orientation of some crystals can increase the inaccuracy in the peak intensities. [44,45]

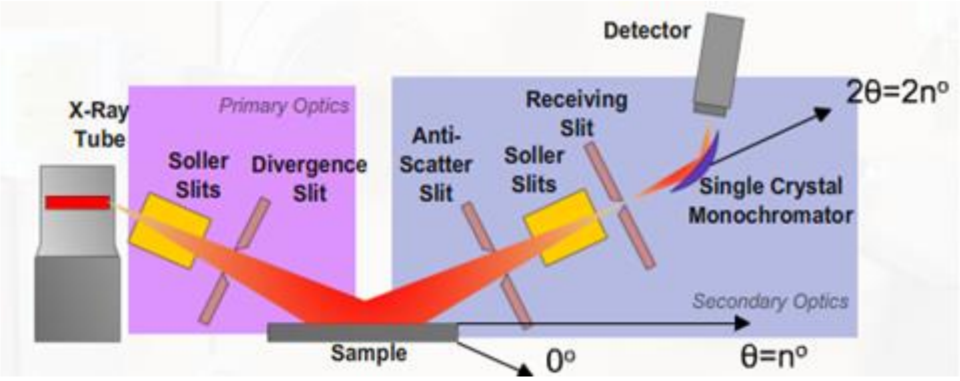

Figure 16. Scheme of the Bragg-Brentano diffractometer

X-Ray powder diffractograms of the samples were measure by a powder diffractometer Miniflex-600 Rigaku with D/tex Ultra2 detector. The x-ray source used was a CuKα tube operated at 40Kv and 15 mA. The range of 2θ was from 5° to 100°, although in plot only the region of 5° to 60° is shown.

CHAPTER V: Results and Discussion

The three different synthesis stages result in sixteen compounds, all of them have a change in its coloration attributed to the coordination with metallic ions.

In the first stage of synthesis, all the compounds have a slow evaporation at room temperature and produce ten compounds presented in Figure 17; these compounds have a characteristic coloration attributed to the coordination of metal ions; compounds from Mn (II) are yellowish, compounds from Co (II) are reddish and compounds from Cu (II) are greenish. Mn(II) and Cu(II) compounds formed kinetic compounds; those was not stable under room temperature and pressure as is shown in Figure 18; the kinetic compounds of copper had a dramatic change of color, the sample AEEA007 started as green blueish compound, then after hydrothermal synthesis some crystals were formed and then after few days the solution took brown dark coloration and crystals collapsed giving way to shine brown precipitate and finally the same solution turned to dark greenish coloration as is shown in Figure 17.

Figure 17. Synthetized compounds from the first stage of synthesis, they have the following order AEEA001, AEEA002*, AEEA003, AEEA004, AEEA005*, AEEA006, AEEA007, AEEA007*, AEEA008 and AEEA009 since the left side.*

In the second stage of synthesis, none sample form a precipitate or kinetic crystal, although the coloration change confirms the metal coordination; after the evaporation of solvent, those samples formed some filaments, but it could not form crystals because those compounds have hydroscopic behavior even when those sample seemed to be dried, they are a very viscous hydrated phase as is shown in for cobalt and manganese samples (Figure 19).

Both synthetic stages produce hydroscopic compounds and after months of slow solvent evaporation at room temperature, drying at 90°C in heat mantel and tough drying in vacuum, those compounds were unable for XRD analysis because Miniflex 600 is a powder X-Ray diffractometer and hydrated samples do not diffract well.

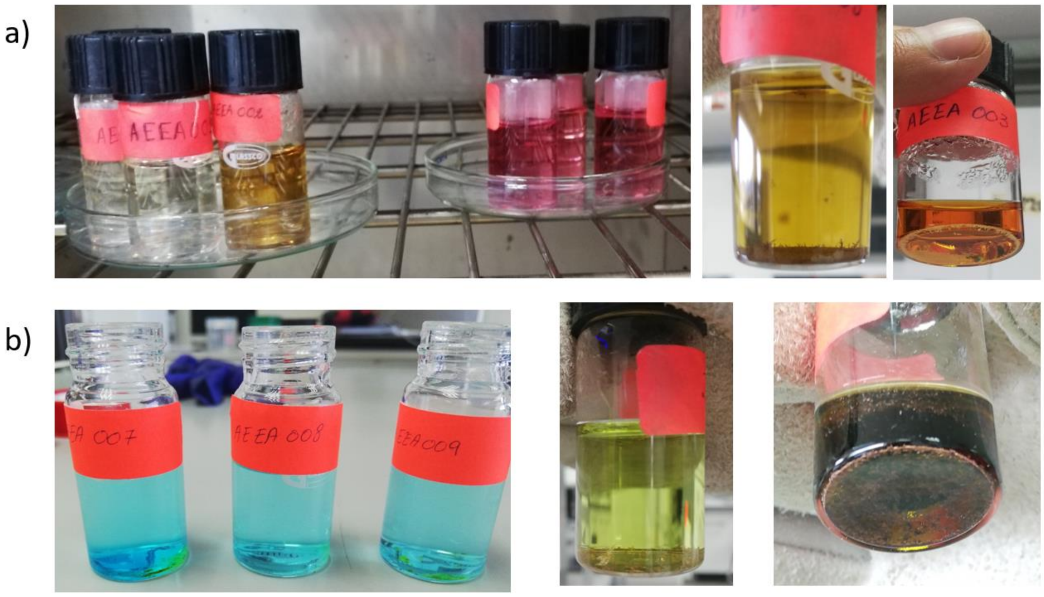

Figure 18. Kinetic compounds formed in the first stage of synthesis. From left to right in a) Mn (II) and Co (II) before hydrothermal synthesis, kinetic compounds of AEEA001 and AEEA003. From left to right in b) Cu (II) samples before hydrothermal, kinetic crystal compounds of AEEA008 recently retired from stove and two days after.

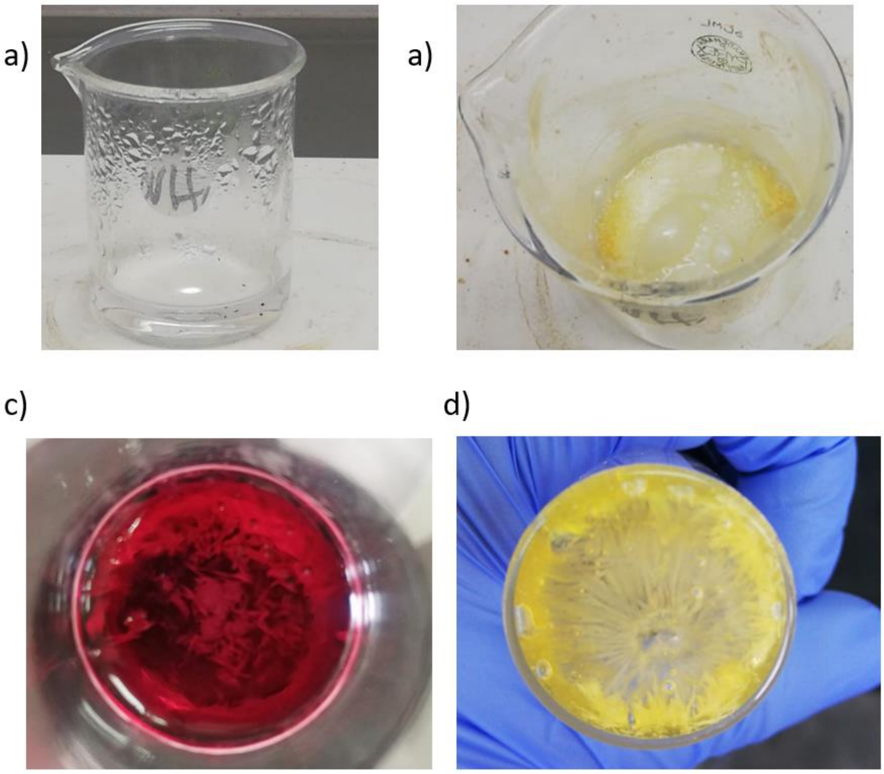

Figure 19. Compounds from second stage of synthesis. a) AEEA010 after reflux synthesis, b) a) AEEA010 compound after drying in heat mantel, c) a) AEEA011 compound and d) a) AEEA012 compound.

The third stage of synthesis was carried out in better conditions for hydrothermal synthesis, the samples with chloride salts formed precipitates and samples with nitrate salts did not form it. The samples of Mn (II) and Cu (II), AEEP and AEEP003, produce visible precipitates so these two phases were separated by filtration in each sample; the copper precipitate is greenish, and the copper soluble phase is darker (Figure 20 c)); the manganese precipitate was darker than manganese soluble phase that has intense yellow coloration (Figure 20 b)). On the on the other hand, the zinc, and cobalt samples (AEEP004 and AEEP003) only present one phase, but in cobalt case, there is a change on color between hydrated compound and dried compound (Figure 20 a)) this change could be produced by the insertion of water molecules in the coordination.

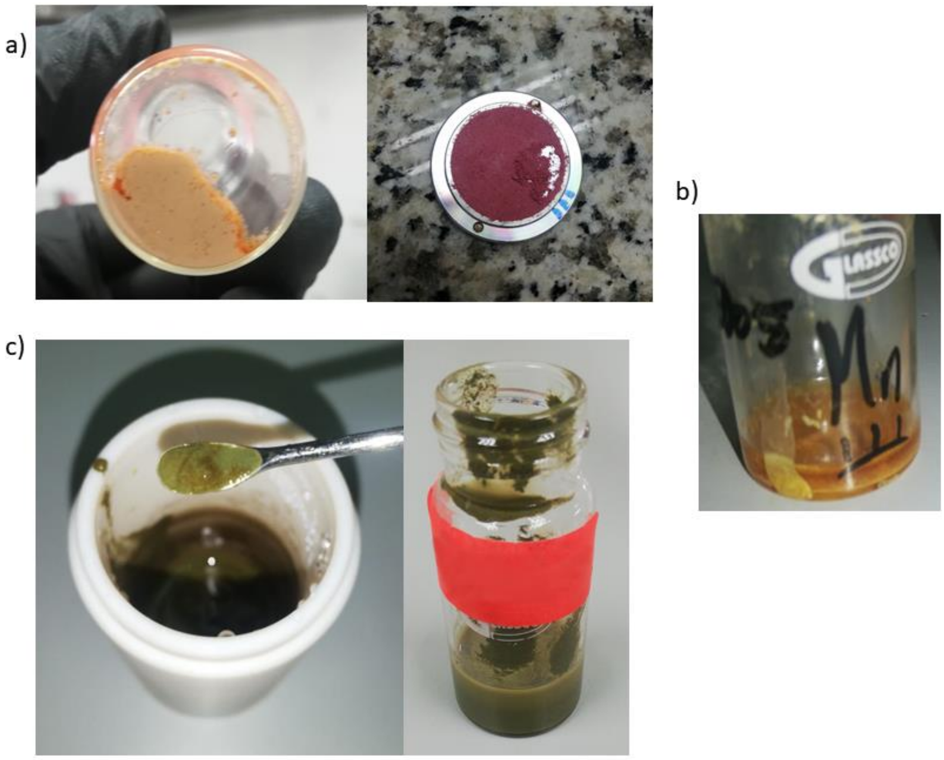

Figure 20. Compounds from third stage of synthesis. a) AEEP002 sample, left side from hydrated compound and right side from dried compound inside the XRD sample holder, b) AEEP001 sample, c) AEEP003 sample with greenish precipitate and dark greenish soluble phase.

The compounds synthesized in the different stages were characterized with ATR-IR and Uv-Vis, but only the third stage compounds were able to take their X-ray diffractogram, those techniques let us understand the possible structures and possible formation of a coordination compound. The IR spectra of the reagents were used as a simplest comparison to get a intioction of the melucules immersed in the coordination, the IR spectra of HMTA, maleic acid and 4,4-bipyridine are showed in , respectively; the maleic acid and HMTA are references of first and second stage synthesis compound, while maleic acid and 4,4-bipyridine for the third stage compounds.

Also, phases identified in XRD analysis were computationally simulated replacing the metal ions, although the soluble phase of copper was not able to take the XRD pattern because it hydrates quickly.

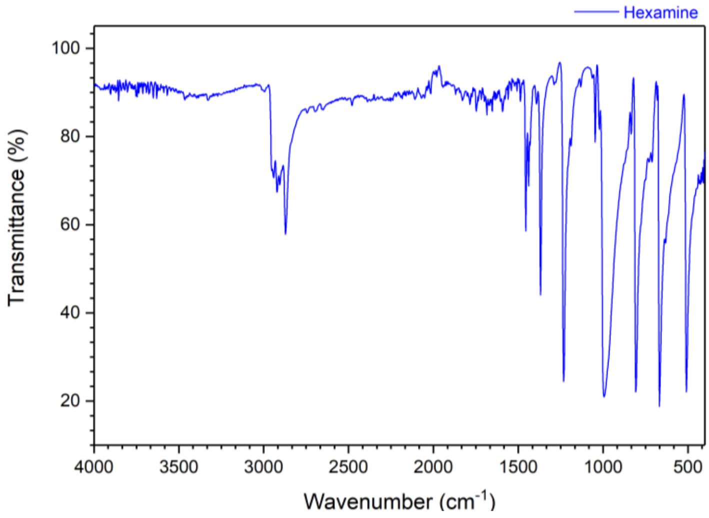

Figure 21. IR spectrum of HMTA (hexamine or hexamethylenetetramine)

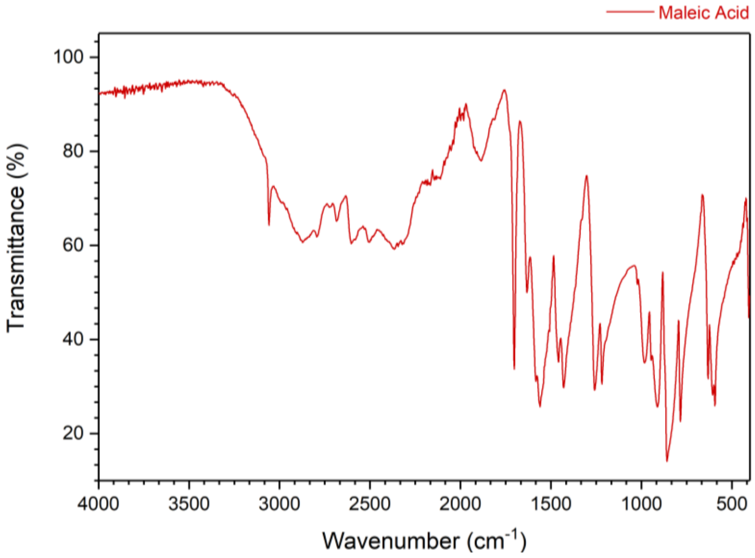

Figure 22. IR spectrum of maleic acid.

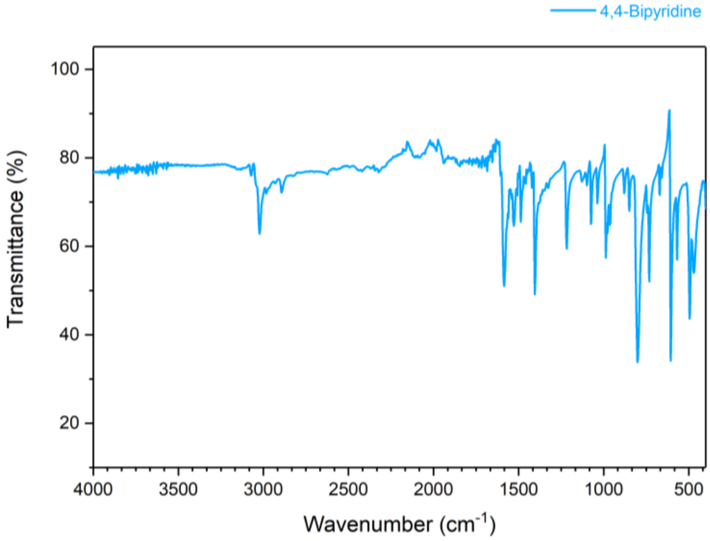

Figure 23. IR spectrum of 4,4-bipyridine.

5.1 Compounds of manganese, HMTA and maleic acid (AEEA001, AEEA002 and AEEA003)

5.1.1 Attenuated Total Reflectance FTIR spectroscopy

The IR spectra of manganese (II) coordination compounds of the first synthesis stage are shown in Figure 24. The more significant bands are from O-H stretching of maleic acid with a broadband B at 3400 - 2400 cm^{-1} which overlaps with bands A at 3100 cm^{-1} and C at 3000 cm^{-1} corresponded to =C-H and C-H stretching respectively[36], others bands related with maleic acid are D at 1700 cm^{-1} of carbonyl, bands E and F at 1580 cm^{-1} and 1395 cm^{-1} from carboxylate asymmetric and symmetric stretching [46], although band E also overlaps de C=C stretching band, the C-O stretching band G was located at 1300 cm^{-1}; the peak D is very visible only in the AEEA003 sample with less amount of amine and then the carbonyl peak reduces the intensity and is shifted to lower frequencies and overlapped by E peak, this effect is a result of increasing of pH since AEEA003 to AEEA001[47]. The bands assigned for HMTA are C at 3100 cm^{-1} of alkane C-H stretching, H and I at 1190 cm^{-1} and 670 cm^{-1} from C-N stretching[48] and C-N bending[49] respectively; on the other hand, the peaks related with manganese complex formation are J and K at 540 cm^{-1} and 420 cm^{-1} from Mn-N interaction and Mn-O interaction respectively[50], so the IR spectra suggest the formation of complex although a specific structure of cannot be suggested with a deep XRD analysis.

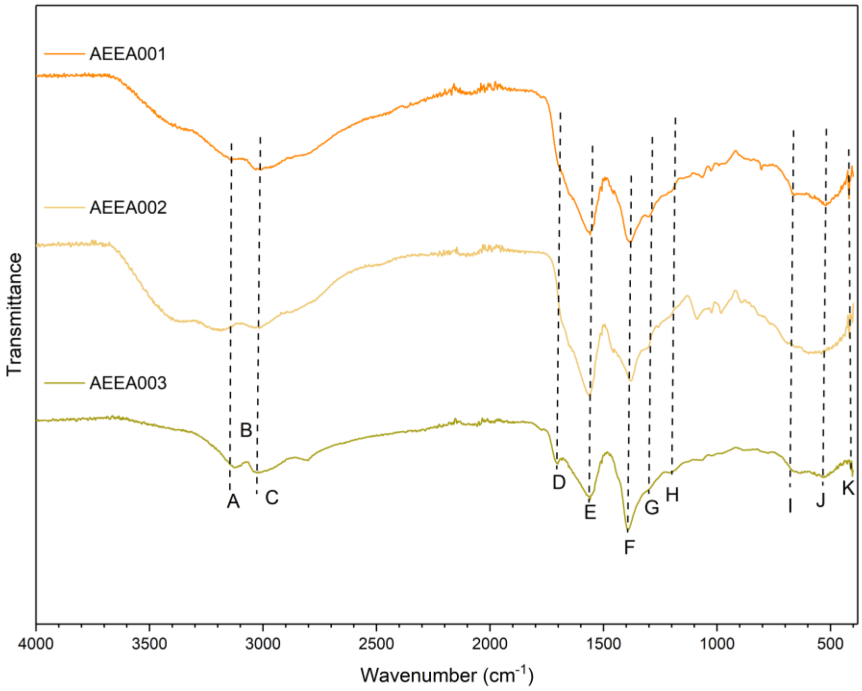

Figure 24. IR of AEEA 001, AEEA002, and AEEA003.

Table 5.IR bands assignations of manganese (II), HMTA, and maleic acid coordination compounds.

Band	Frequency (cm $^{-1}$)	Type of vibration
A	≈ 3100	alkene sp2 C-H stretching
B	≈ 3400 -2400	-OH
C	≈ 3000	alkane -CH sp3 stretching
D	≈ 1700	-C=O
E	≈ 1580	-C=C- stretching, -COO- asymmetric carboxylate
F	≈ 1395	- COO- symmetric carboxylate
G	≈ 1300	-CO stretching
H	≈ 1190	-C-N stretching
I	≈ 670	-C-N bending
J	≈ 540	-Mn-N stretching
K	≈ 420	-Mn-O stretching

5.1.2 UV-Vis Spectrometry

In the UV-Vis spectra, there are no absorptions in the visible region (400 nm-800 nm) which suggests no d-d electronic transition of manganese (II), the absorptions in UV region can be associated with LMCT[50] as is shown in Figure 25. Considering the d^5 Tanabe-Sugano diagram the unique possible crystal field configuration is an octahedral high spin configuration because the ground state $^6A_1$ has no allowed spin electronic transitions for d^5 high spin, also this agrees the nature of ligand with HMTA as only σ donor and maleic carboxylate as π donor as weak field ligands[5,41,51]. Another important characteristic of this pattern is a bathochromic shift by the increase in the molar rate of maleic acid reducing the splitting of Δ_O.

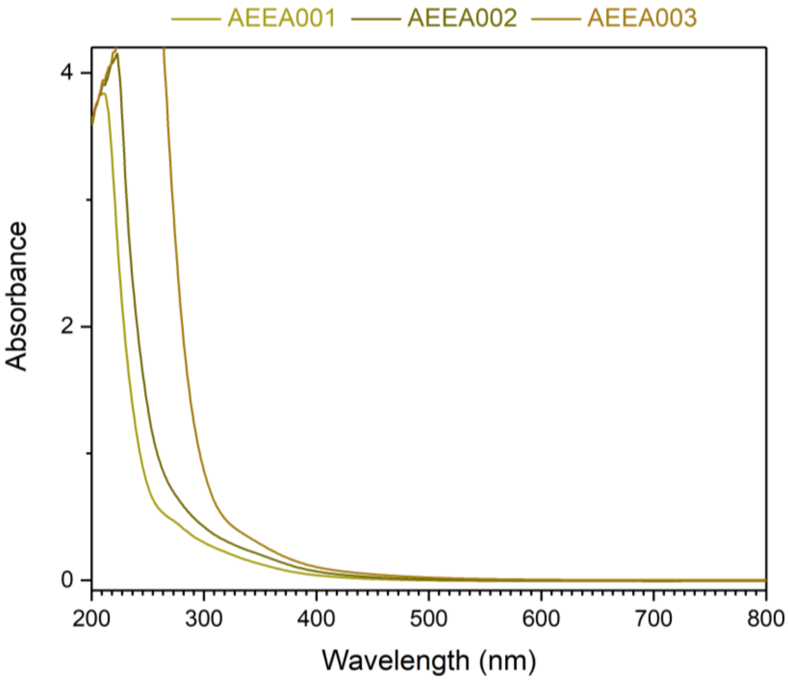

Figure 25. UV-Vis spectra of MOFs AEEA001, AEEA002 and AEEA003

5.2 Compounds of cobalt, HMTA and maleic acid compounds (AEEA004, AEEA005 and AEEA006)

5.2.1 Attenuated Total Reflectance FTIR spectroscopy

In the IR spectra of Co(II) compounds (AEEA001, AEEA002, AEEA003) (Figure 26) bands belong to the maleic acid and HMTA are presented and tabulated in Table 6; the presence of maleic acid in the compounds is confirmed by bands A from CH alkene stretching, C from carbonyl, D from carboxylate asymmetric stretching overlapped with C=C stretching[46], peak E from symmetric carboxylate stretching[52] and peak I assigned to cis alkene[37,53], also is visible the effect of pH on the peak C from carbonyl [47] which is visible only in AEEA006 and in AEEA004 and AEEA005 is presented as a shoulder; the peak H of -C-N stretching [48] is related with HTMA; on the other hand, the peak assigned to nitrates from salt is F at 1384 cm^{-1} [42,54] , the peaks J and K suggest possible coordination of cobalt (II) with nitrogen and oxygen respectively [55]

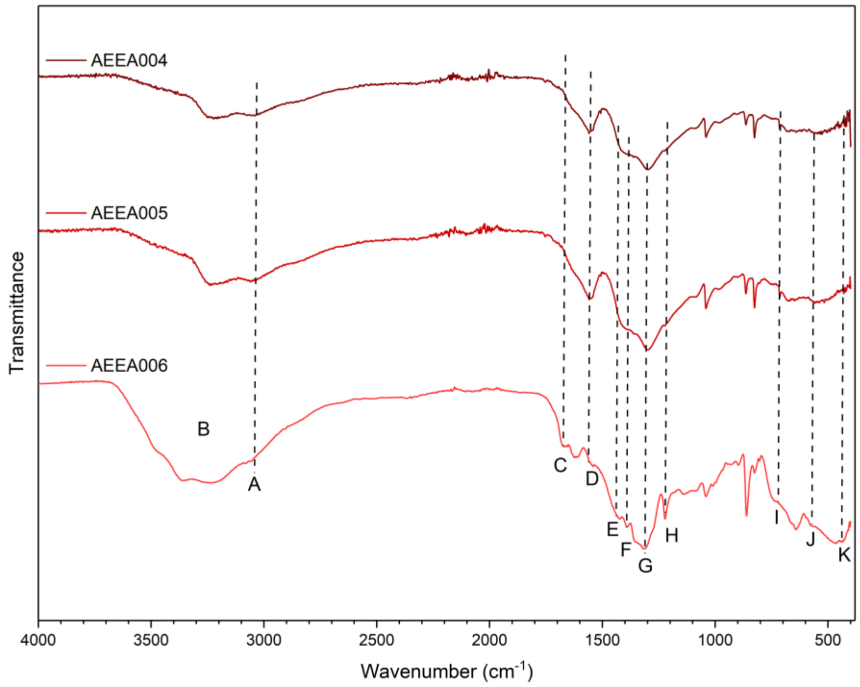

Figure 26. IR of AEEA004, AEEA005 and AEEA006.

Table 6. IR bands assignations of cobalt (II), HMTA, and maleic acid compounds in the first stage of synthesis.

Band	Frequency (cm^{-1})	Type of vibration
A	≈ 3050	alkene sp2 C-H stretching
B	≈ (3400 -2400)	O-H stretching
C	≈1680	-C=O stretching
D	≈ 1560	-C=C stretching, -COO- asymmetric carboxylate
E	≈ 1420	-COO- symmetric carboxylate
F	≈ 1384	nitrate
G	≈ 1300	-C-O stretching
H	≈1220	-C-N stretching
I	≈715	=CH cis out of plane
J	≈565	Co-N stretching
K	≈ 430	Co-O stretching

5.2.2 UV-Vis Spectrometry

The UV- Vis spectra of AEEA004, AEEA005, and AEEA006 (Figure 27) present two absorption peaks on each one in the visible region and the transitions with highest absorptions are in the range of 506 nm to 520nm suggesting an octahedral complexation[56]; also, the ligands of those complexes, HMAT, and maleic acid, let a Co (II) configuration on the crystal field and those peaks correspond to the higher energy transitions, to assign the electronic transition and approximated energy of each one a Tanabe Sugano analysis was carried out and the results are presented in Table 7. The visible transitions correspond to ${}^4T_{1g} \rightarrow {}^4A_{2g}$ and ${}^4T_{1g} \rightarrow {}^4T_{1g}$ and the lowest energy transition ${}^4T_{1g} \rightarrow {}^4T_{2g}$ is not shown in the UV-Vis spectra because is in the infrared zone (Figure 27. UV-Vis spectra of MOFs AEEA004, AEEA005 and AEEA006.), the values of octahedral delta, Racah parameters, and ${}^4T_{1g} \rightarrow {}^4T_{2g}$ were estimated too.

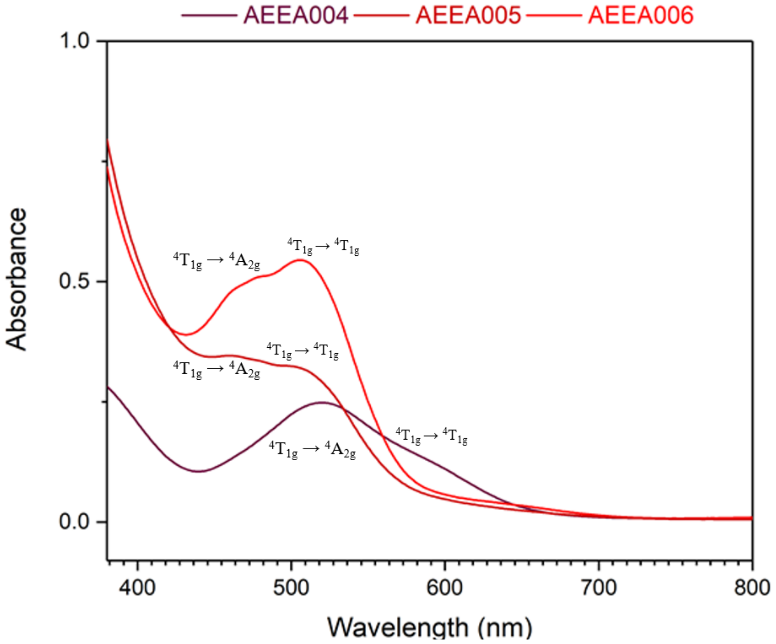

Figure 27. UV-Vis spectra of MOFs AEEA004, AEEA005 and AEEA006.

Table 7. Electronic transitions on the AEEA 004, AEEA005, and AEEA006 samples. The lowest electronic transition was predicted by Tanabe Sugano diagram for d7 high spin. The table tabulated values of wavelength and wavenumber for each transition and include Raca.

Sample	**AEEA004**		**AEEA005**		**AEEA006**	
	nm	**cm^{-1}**	**nm**	**cm^{-1}**	**nm**	**cm^{-1}**
$^4T_{1g} \rightarrow {}^4A_{2g}$	475	21053	446	21739	520	19230
$^4T_{1g} \rightarrow {}^4T_{1g}$	510	19608	505	19802	566	17668
$^4T_{1g} \rightarrow {}^4T_{2g}$	983.7	10165.4	975.8	10248.4	1098.3	9104.9
Δ_O (cm^{-1})	11617.6		11771.8		10458.4	
B	726.1		692.5		615.2	

5.3 Compounds of copper, HMTA and maleic acid compounds (AEEA007, AEEA008 and AEEA009)

5.3.1 Attenuated Total Reflectance FTIR spectroscopy

The ATR-FTIR spectra of copper (Figure 28) compounds from the first stage of synthesis, show the presence of maleic acid and HMTA in the final compound. The main bands related to maleic acid are A, B, C, D, E, and H which were assigned to alkene CH stretching, OH acid stretching, asymmetric and symmetric carboxylate stretching, and CH cis out of plane was assigned to H band[36,46,53]; while peak G was assigned to C-N stretching of HMTA; the peaks I and J suggest a possible coordination of copper (II) ion with the carboxylate groups and nitrogen atoms from HTMA[52,55].

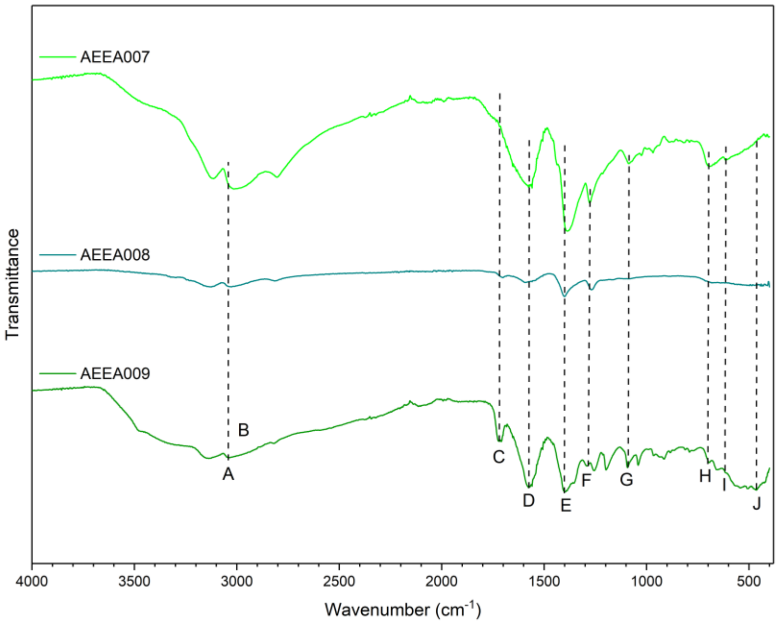

Figure 28. IR spectra of MOFs AEEA 004, AEEA005, and AEEA006. Those compounds are made of copper (II), HMTA, and maleic acid.

Table 8. IR bands assignations of copper (II), HMTA, and maleic acid compounds in the first stage of synthesis.

Band	**Frequency (cm^{-1})**	**Type of vibration**
A	≈ 3100	alkene sp2 C-H stretching
B	≈ (3500 -2400)	-O-H stretching
C	≈1715	-C=O stretching
D	≈ 1580	-C=C stretching, -COO- asymmetric carboxylate
E	≈ 1400	- COO- symmetric carboxylate
F	≈ 1280	C-O stretching
G	≈1090	C-N stretching
H	≈700	=CH out of plane
I	≈600	Cu-N stretching
J	≈ 450	Cu-O stretching

5.3.2 UV- Vis spectroscopy

In the UV- Vis spectra those compounds (Figure 29) present a broad absorption band as a result of the electronic configuration of copper (II) as d^9 ion whit only one possible d-d electronic transition, normally this compound has a distorted octahedral conformation[41,57], although evaluating the ligands it is more probably an elongate octahedral structure because the carboxylates contribute to a strong crystal field. The peaks are at 704nm, 746nm, and 794nm from AEEA007, AEEA008, and AEEA009 respectively, where it is evident a bathochromic shift related to the increase of molar rate between maleic acid and HMTA.

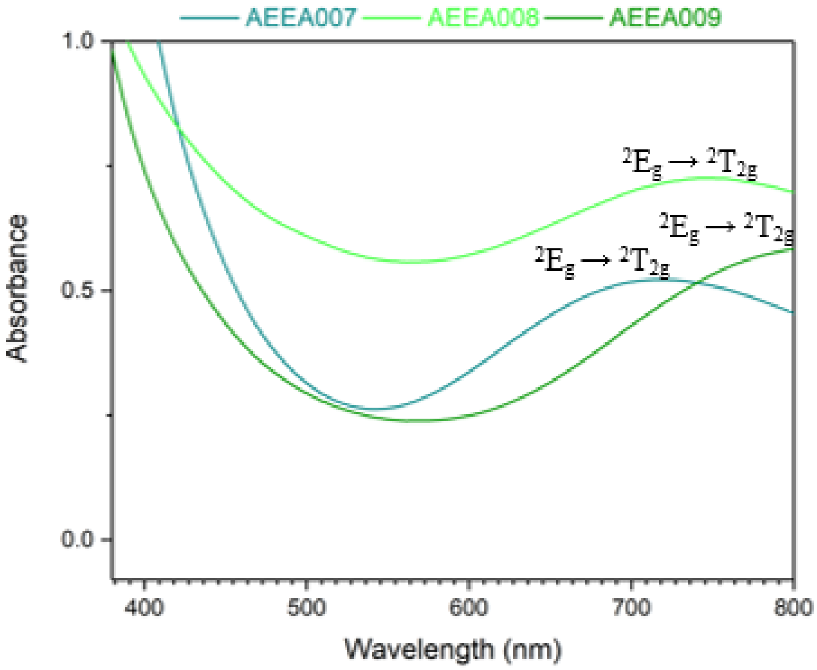

Figure 29. UV-Vis spectra of samples AEEA007, AEEA008, and AEEA009

5.4 Compounds synthetized by reflux (AEEA010, AEEA011 and AEEA012)

5.4.1 Attenuated Total Reflectance FTIR spectroscopy

The compounds of the second stage of synthesis remain the same molar rate 1:1:1 between metallic salt, maleic acid, and HMTA. In the FTIR spectra (Figure 30) of those compounds, bands related with maleic acid and HMTA are visible, the specific values for each compound are tabulated in Table 9; the bands A and B are from CH alkene stretching and O-H stretching although band B overlaps bands from CH sp^3 from HMTA, the band C related with carbonyl group is not well defined in the AEEA012 compound but is presented as shoulder overlapped with band D, the bands D and E are related with carboxylate asymmetric and symmetric stretching. The FTIR spectra of AEEA011 and AEEA012 are more similar because the metallic salts have the same counter ion (nitrate) and it is visible in the band F that overlaps the peak from nitrate normally at 1384 cm^{-1} [42,54], but the assignment for F band is the C-O stretching. On the other hand, the band G is from C-N stretching of HMTA, and H peak is from CH cis out of plane[48,53], while the peaks related with metal coordination are I and J from M-N and M-O interaction respectively, although the peak J is not visible in the sample AEEA010 because the peaks of metal-oxygen interactions are normally weak and appear near to the 430cm^{-1} [23,50,35,39].

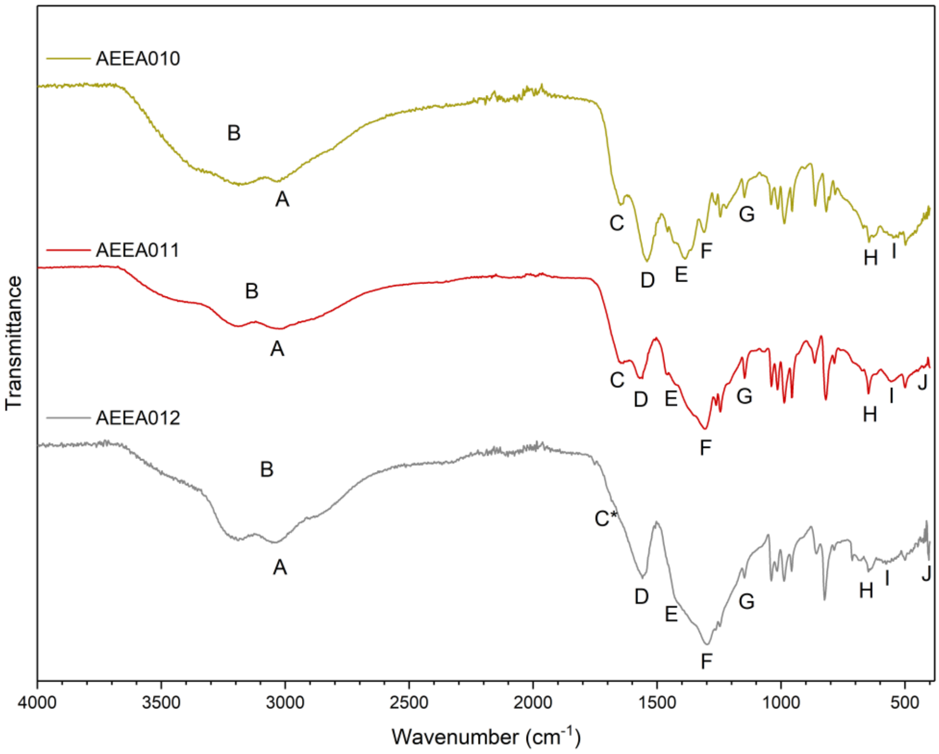

Figure 30. IR spectra of samples AEEA010, AEEA011, and AEEA012. Those compounds are synthesized from maleic acid and HMTA with the ions Mn(II), Co(II), and Zn(II) respectively.

Table 9. IR bands assignations for compounds synthesized in the second stage by reflux condition.

Band reference	**Type of vibration**	**AEEA010 /cm^{-1}**	**AEEA011 / cm^{-1}**	**AEEA012 / cm^{-1}**
A	alkene sp2 CH stretching	3030	3035	3035
B	-O-H stretching	3600-2500	3600-2400	3600-2600
C	-C=O stretching	1660	1665	-
D	-C=C stretching, -COO- asymmetric carboxylate	1550	1560	1560
E	- COO- symmetric carboxylate	1390	1410	1415
F	-C-O stretching	1300	1304	1302
G	-C-N stretching	1145	1147	1155
H	=C-H out of plane	650	655	650
I	M-N stretching	550	560	570
J	M-O stretching	-	415	420

5.4.2 UV- Vis spectroscopy

In the UV-Vis spectra (Figure 31) the samples AEEA010 and AEEA012 do not have any absorption in the visible region, those spectra belong to the Mn(II) and Zn(II) respectively, this behavior is expected because the Mn(II) has a 3d^5 electronic configuration and nature of ligands suggest a high spin crystal field configuration that is corroborated by d^5 Tanabe Sugano diagram because there is no allowed spin transition for $^6A_1$ ground state[41,59], while Zinc(II) has a 3d^{10} electronic configuration, therefore, any d-d transition is possible, in both cases the color of the compounds can be attributed to LMCT which are visible in ultraviolet region[60]. The compound AEEA011 has transitions at 507 nm and 480 nm and according to the nature of ligands it is expected a d^7 high spin configuration, those transitions correspond to $^4T_{1g} \rightarrow {}^4A_{2g}$ and $^4T_{1g} \rightarrow {}^4T_{1g}$ respectively and the Δ_O has an approximate value of 11228.51 cm^{-1}.

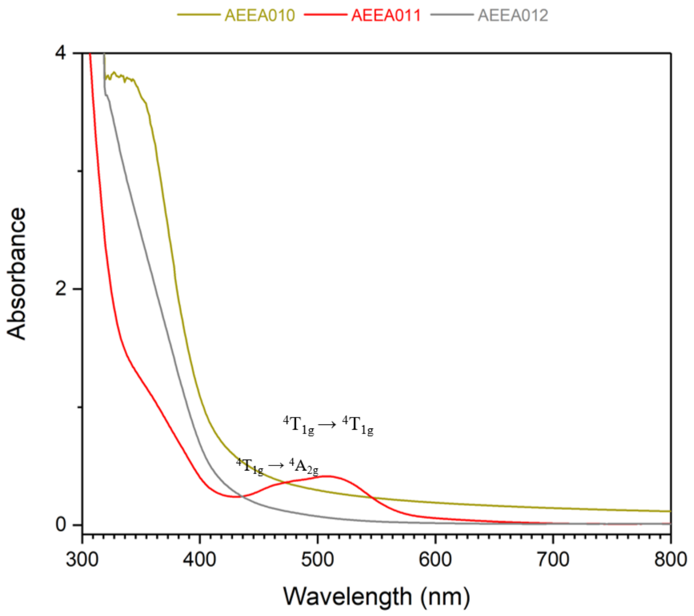

Figure 31. UV-Vis spectra of samples AEEA010, AEEA011 and AEEA012

5.5 Compounds of manganese, 4,4-bipyridine and maleic acid (AEEP001)

5.5.1 Attenuated Total Reflectance FTIR spectroscopy

In the third stage of synthesis the hydrothermal synthesis was carried out on an autoclave to improve the synthetic environment, the sample AEEP 001 formed a precipitate in a very small quantity which will be called Mn-ma-bpy*, while another dissolved phase as Mn-ma-bpy. In the FTIR spectrum of Mn-ma-bpy* only is visible bands of 4,4-bipyridine (bpy), the band A is associated with sp^2 CH stretching, the band E was assigned to C=N stretching[61], the bands G, I, and K was assigned to semicircle stretching from heterocycle, C-N stretching and 2 adjacent H wag respectively and finally the band L was assigned to Mn-N interaction[36,37,62].

The FTIR spectrum of Mn-ma-bpy (Figure 32) have the same bands of 4,4 bipyridine but from maleic acid too, as is shown in Table 10; the peaks related with maleic acid are the band B related with OH stretching overlapping the band A from CH sp^2 stretching, the bands C and D are from carbonyl group and C=C stretching from acid, while the peak E* represent the C=N band and asymmetric carboxylate stretching overlapped themselves and peak G* was assigned to symmetric carboxylate stretching and semicircle stretching overlapped themselves, the peak J is C-O stretching band while the peaks L and M are related with the interaction between Mn(II) and N and O respectively[36,37,62].

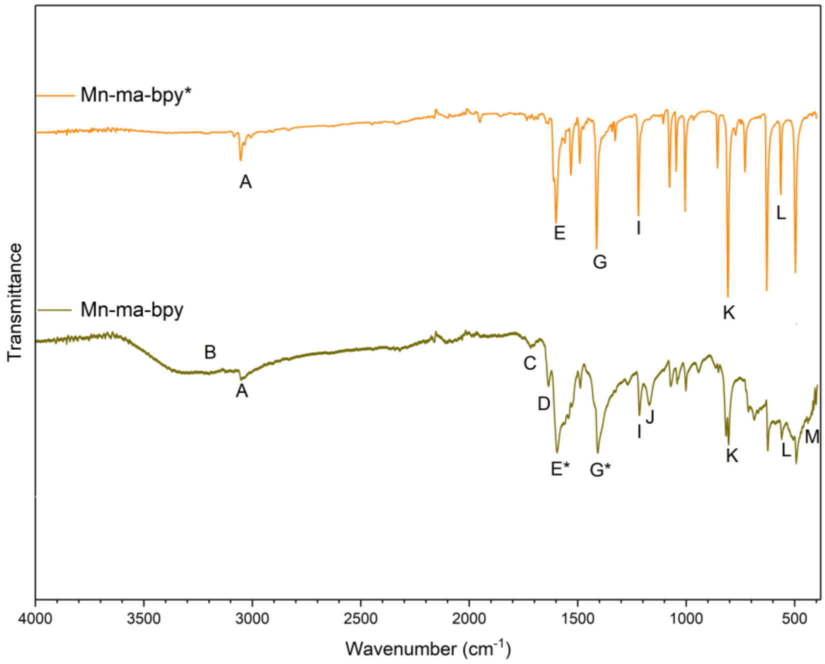

Figure 32. IR spectra of sample AEEP001. The Mn-ma-bpy correspond to the precipitate and Mn-ma-bpy to the dissolved part.*

Table 10. IR bands assignations for Mn-ma-bpy and Ma-ma-bpy sample.*

Band	Type of vibration	Mn-ma-bpy*	Mn-ma-bpy
A	alkene sp2 CH stretching	3055, 3037	3040
B	-OH	-	3600 -2500
C	-C=O	-	1716
D	-C=C stretching acid	-	1635
E	-C=N	1600	1602*
F	-COO- asymmetric carboxylate	-	1602*
G	Semicircle stretching	1415	1410*
H	-COO- symmetric carboxylate	-	1410*
I	-C-N stretching	1220	1222
J	-C-O stretching	-	1170
K	2 adjacent H wag	808	806
L	Mn-N	564	564
M	Mn-O		442

5.5.2 DRUV-Vis spectroscopy

In the Diffuse Reflectance UV-Vis spectra of sample AEEP001, it is clear a similar behavior in both phases Mn-ma-bpy and Ma-ma-bpy*, although in the case of Mn-ma-bpy*, the 4,4 bipyridine is the unique ligand which could let a low spin configuration the low oxidation state and as 3d transition metal the high spin configuration is preferred and reflected in the spectrum where there is not any d-d electronic transition in the visible region; while in the Mn-ma-byp the oxygen donor (maleic acid) advantages the high spin configuration as too the oxidation state and its 3d energy level, so in both cases as high spin $3d^5$ electronic configuration there is not allowed spin transition, but in both the absorptions lower than 400 nm is the result of LMCT.

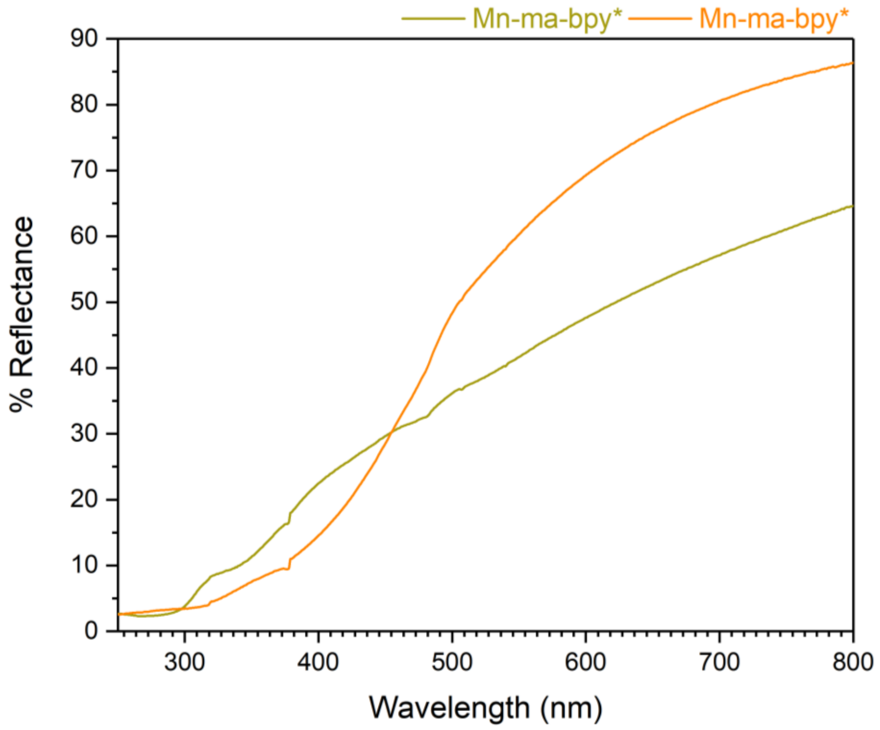

Figure 33. Diffuse Reflectance UV-Vis spectra of AEEP001, both phases are presented Mn-ma-bpy and Mn-ma-bpy.*

5.5.3 X-Ray Powder Diffraction and Simulation of XRD patterns

The analysis of X-Ray Powder Diffraction was carried out after a thorough drying of several days, because those compounds have a hydroscopic behavior although the precipitate can remain dried for a couple of hours, on the contrary, the other phase absorbs water in few minutes. This behavior delays the preparation of the sample and taking the diffractogram; this analytic technique was performed in a Rigaku Miniflex 600 diffractometer and has the main objective to determine the crystalline structure and possible phases presented in the samples. The diffractograms was taken in range of 5-90 degrees with $K\alpha_1\alpha_2$ of copper of 1.54056 Å at room temperature.

5.5.3.1 X-Ray Powder Diffraction of Mn-ma-bpy

In the XRD analysis of Mn-ma-bpy, two possible phases were identified. In the CCDC database, the phase was 4,4'-Bipyridinium hexachloro-osmium(IV), this phase was reported by B. Dolling and his team in 2001. The reagents of this sample could form this phase, but according with XRD comparison there are not many similarities between their XRD patterns and even the simulated phase with Mn (II) as metal center do not have all the peaks, although simulated phase XRD was calculated in Mercury software after replacing Os (IV) by Mn (II) in the original structure (Figure 34). The Os (IV) phase and simulated phase for Mn (II) are orthorhombic systems and have an octahedral coordination for each metal. This identified phase agrees with DRUV-Vis spectra because the coordination of chlorides with Mn (II) ion should produce a high spin d^5 configuration therefore any d-d transition is spin allowed and the unique transition is in UV region produced by LMCT; on the other hand the FTIR spectra on Mn-ma-bpy shows the presence of maleic acid, so the identified phase do not match and can be a minority phase dissolved. This phase as is shown in (*) is a molecular coordination compound, has octahedral coordination between a Mn (II) and six chloride ions, while the bipyridines stablish the structure, but they do not form any ligand bridge; the unit cell presented in Figure 35 shows fifteen coordination octahedrons and eight 4,4 bipyridines, but they do not stablish a framework in any direction, and it is an undesired phase for the propose of this work.

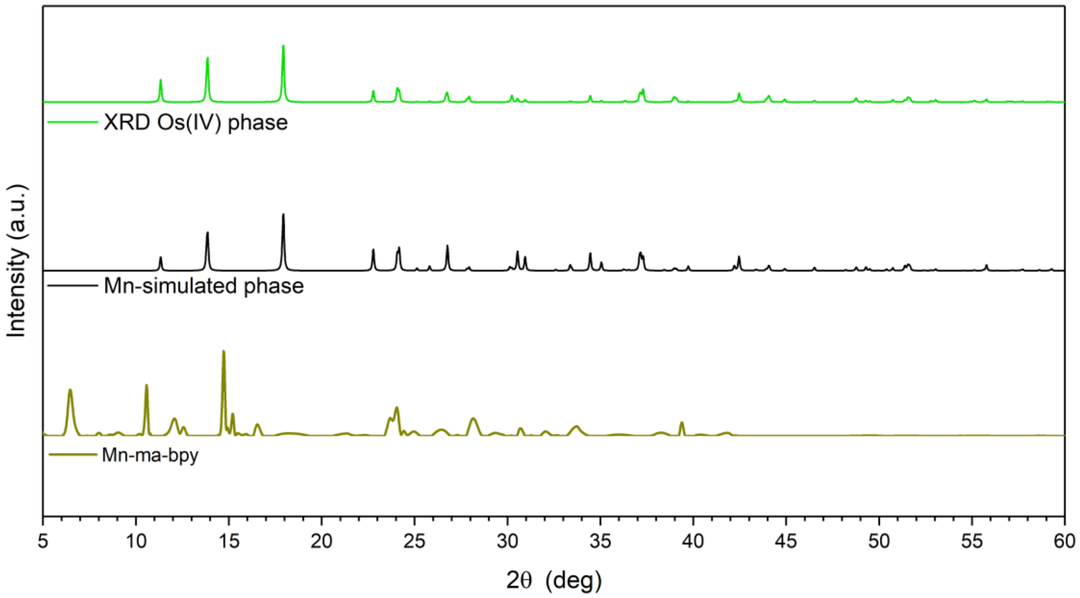

Figure 34. XRD patterns for Mn-ma-bpy structure determination. The phase found by geometry optimization is referred as Mn-simulated phase, the XRD Os (IV) phase is the phase found by phase comparison in Smart Lab Studio II and the experimental pattern is labeled as Mn-ma-bpy.*

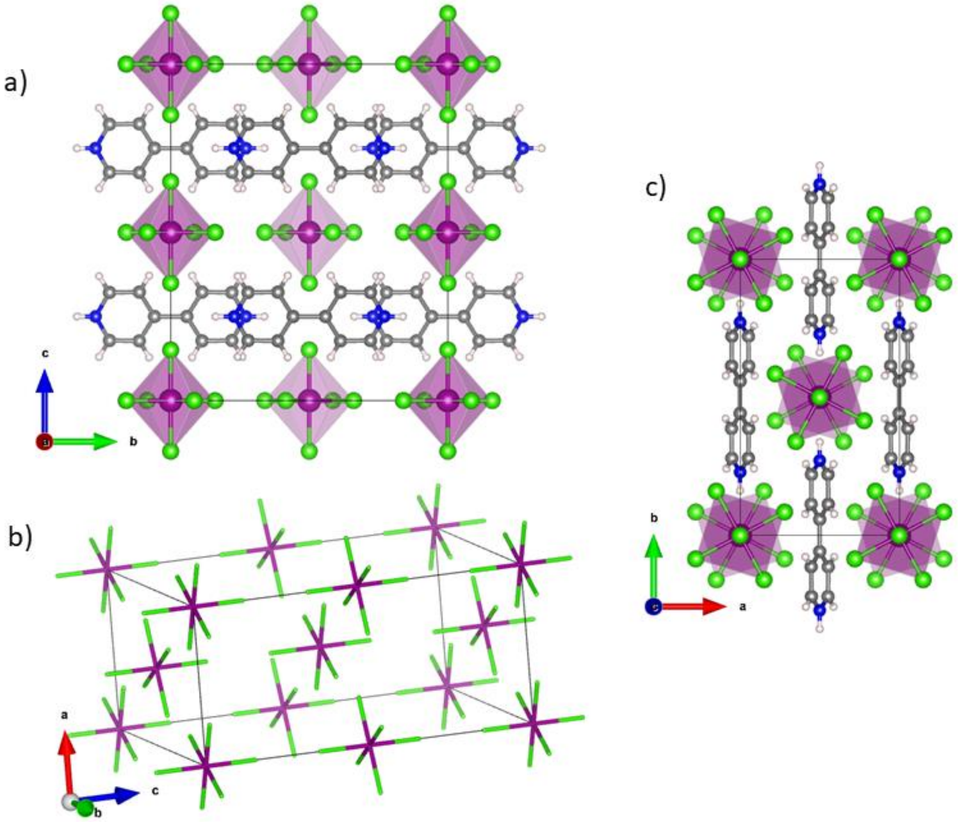

Figure 35. Mn-simulated phase simulation projected on planes. a) projection on a, b) perspective projection that shows no bonds between octahedrons. c) projection on c.

Another phase was matched with the experimental XRD of Mn-ma-bpy; this phase has tw0 4,4 bipyridines in axial positions and four maleic anhydrides as the coordination sphere on Cu (II), that phase was reported by Marylin Quintero and Edward Avila in 2011[34]. The same process was performed, the XRD was calculated in Mercury software after replacing Cu (II) by Mn (II) in the original structure. In this case, again the match between the experimental XRD pattern (Mn-ma-bpy) and Cu (II) phase and Mn (II) simulated phase 2 do not match as it should do it (Figure 36), but the main reason to refute this phase is the FTIR pattern of Mn-ma-bpy that do not have any band belongs to maleic anhydride. This phase is MOF that form maleic anhydride and 4,4 bipyridine brides between the Mn (II) ion and chlorides act as counter ion; this configuration lets formation of channels in c and a direction as is shown in Figure 37 .

After the analysis, the Mn- phase simulated (Figure 34) is possible because the FTIR pattern suggest the presence of maleic acid and 4,4-bipyridine in Mn-ma-bpy sample, but do not limit the presence of one phase which only contain 4,4 bipyridine; on the other hand, the Mn simulated phase 2 cannot be in the Mn-ma-bpy because there is not any band in FTIR spectrum corresponding to carbonyl from anhydrides.[36,37]

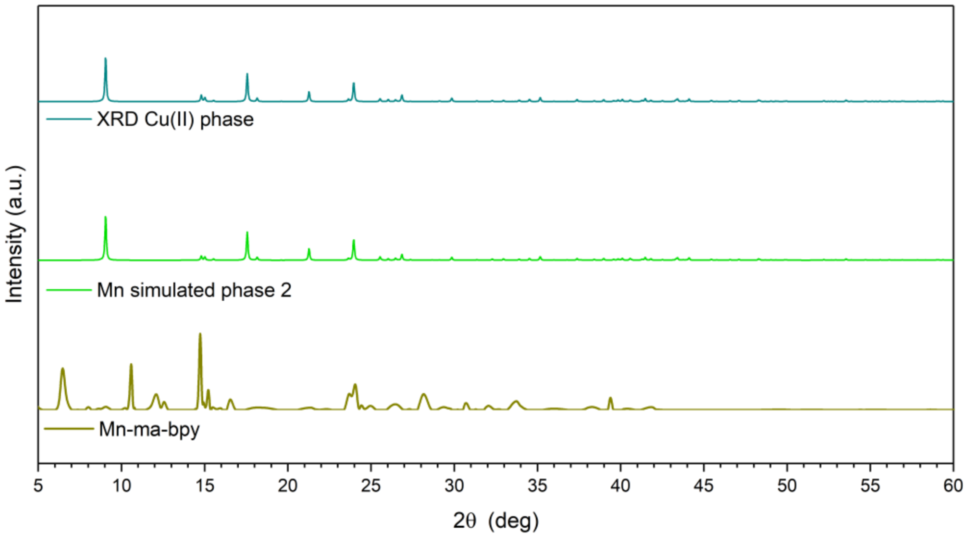

Figure 36. XRD patterns of Cu (II) phase matched by Smart Lab Studio II, Mn simulated phase 2 and Mn-ma-bpy as experimental pattern.

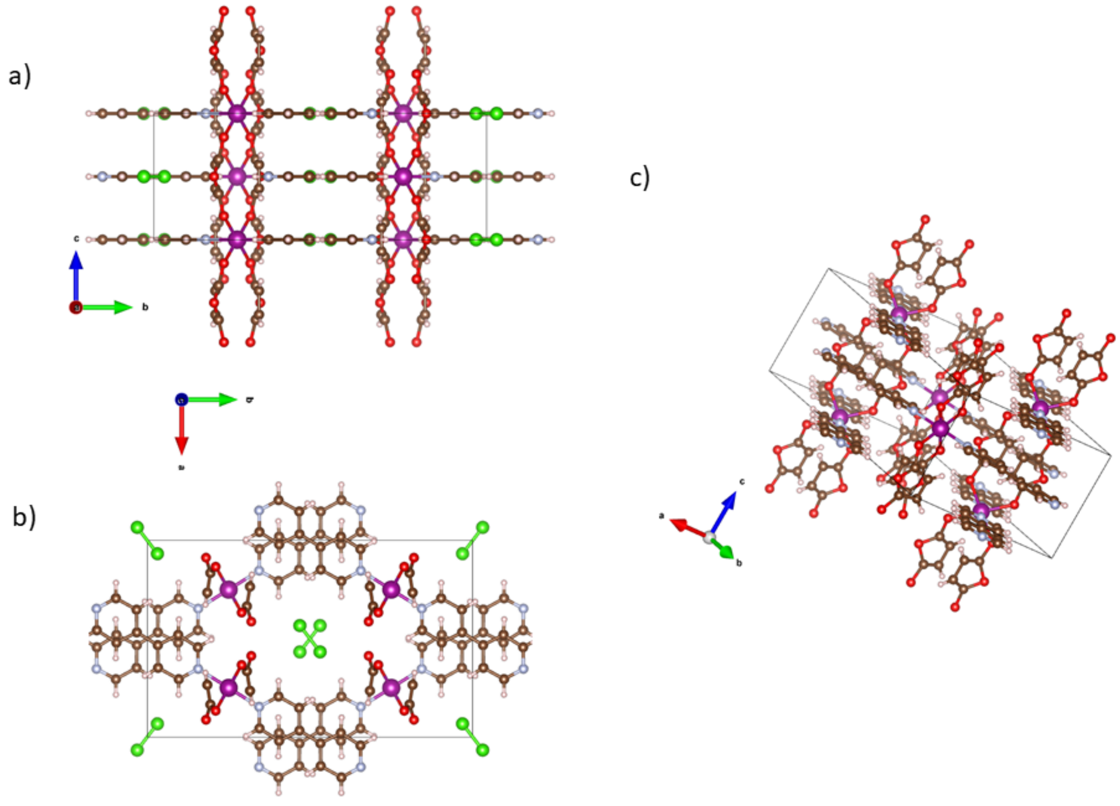

Figure 37. Mn simulated phase 2 projected on planes. a) projection on a plane, b) projection on c plane. c) perspective projection of chains formed by the MOF.

*4.5.3.2 X-Ray Powder Diffraction of Mn-ma-bpy**

In the XRD analysis of Mn-ma-bpy* was identified a phase presented in the precipitate, the identification needed a database of CCDC because there are not register any similar structure on free libraries, the values of this phase are presented in Table 11. The phase identified by SmartLab Studio II correspond to catena-[bis(m-2-chloro)-(m-2-4,4'-bipyridyl)-cadmium(II)] reported by Chunhua Hu and his team in 2003, this structure belong to octahedral coordination of Cd(II) with four chloride bridges on the equatorial plane and two 4,4 bipyridines on axial positions as a 2D coordination polymer[63], this structure agrees with the FTIR of Mn-ma-bpy*where only the 4,4 bipyridine is present although the metallic center in different in the case of Cd(II) has a $4d^{10}$ configuration without any possible d-d electronic transition, while Mn(II) in this case as high spin $3d^5$ have spin forbidden transition. The structure of the cadmium phase was optimized replacing the metallic center with Mn (II) in Quantum-Espresso software with the accuracy allowed by available computational resources, then with the optimized structure, the XRD pattern was calculated and compared with the experimental pattern of Mn-ma-bpy* and cadmium phase as is shown in Figure 38. The simulation of the XRD pattern was made with a scan range of 5 to 90 degrees and with the copper wavelength of Kα= 1.54056 Å in Mercury Software, it is notable the better with of XRD phase simulated of Mn (II) with experimental XRD diffractogram (Mn-ma-bpy) than with Cd(II) phase (Figure 38).

Table 11. Crystallographic data of Cd (II) phase and Mn (II) simulated phase.

	Cd (II) phase	**Mn*-simulated**
Chemical Formula	$(C_{10}\ H_8\ Cd\ Cl_2\ N_2)_n$	$(C_{10}\ H_8\ Mn\ Cl_2\ N_2)_n$
Molecular Weight	339.50 g/mol	282.03 g/mol
Radiation	Kα=1.54056 Å	Kα= 1.54056 Å
Crystalline system	Orthorhombic	Orthorhombic
Space group	P b a n	P b a n
Cell parameters	**a** 11.796 **b** 12.084 **c** 3.7716 **α** 90 **β** 90 **γ** 90	**a** 11.796300 **b** 12.084294 **c** 3.771690 **α** 90 **β** 90 **γ** 90
Volume	573.615	537.654

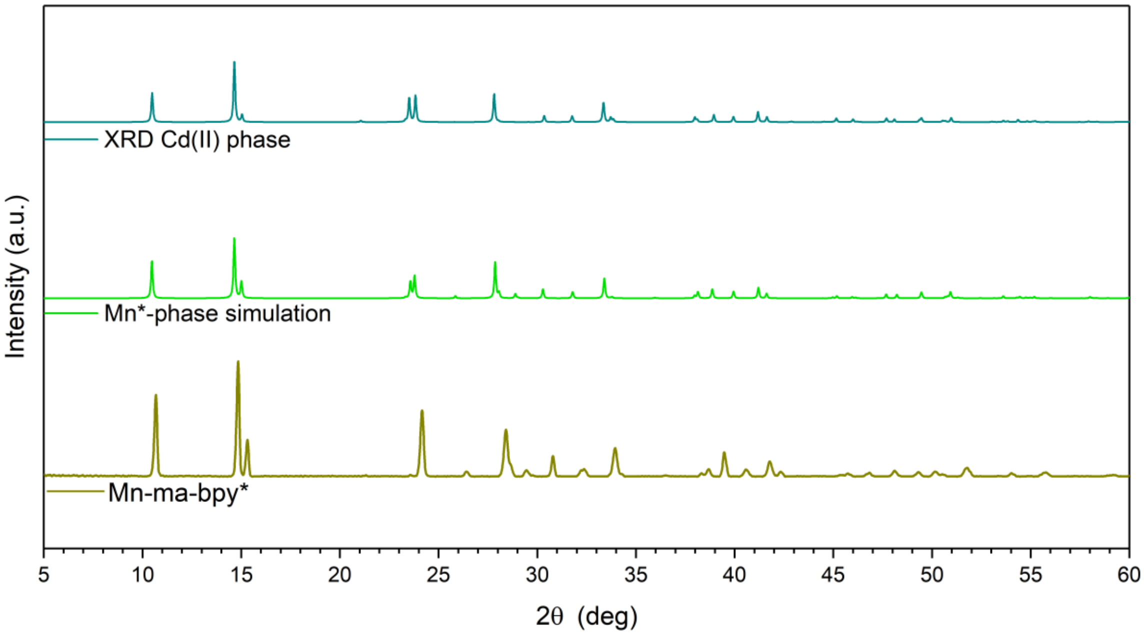

Figure 38. XRD patterns for Mn-ma-bpy structure determination. The phase found by geometry optimization is referred as Mn*-phase simulation, the XRD Cd (II) phase is the phase found by phase comparison in Smart Lab Studio II and the experimental pattern is labeled as Mn-ma-bpy**

The optimized structure for Mn (II) coordination polymer describes a 2D polymer, the coordination in the Mn(II) is a compressed octahedron with shorter bond distances between nitrogen and Mn(II), this slight distortion is tabulated in Table 12 with the coordination lengths and bond angles, the chlorides has the same length of bonds with Mn(II) although this larger length can be result of their function as bridges between the metallic centers. The asymmetric unit in composed of one Mn(II) ion, one chloride and a quarter of 4,4- bipyridine as is shown in Figure 39; the unit cell is formed of two parallel parts displaced ½ in (a) direction, each part is formed of four chlorides, a Mn(II) and a 4,4 -bipyridine (Figure 39. c)).

Table 12. Mn (II) coordination data in Mn-ma-bpy phase simulation, the bond lengths and bond angles related with Mn (II) are presented. The labels of atoms are from the Figure 25 in section (a))

Bond	Length (Å)	Bond	Bond angles (°)
Mn1-Cl1	2.621	Mn1-Cl1-Cl2	88.05
Mn1-Cl2	2.621	Mn1-Cl1-Cl3	91.95
Mn1-Cl3	2.621	Mn1-Cl1-N1	90
Mn1-Cl4	2.621	Mn1-Cl1-N2	90
Mn1-N1	2.335	Cl1-Mn1-Cl3	179.99
Mn1-N2	2.334	Cl2-Mn1-Cl4	180

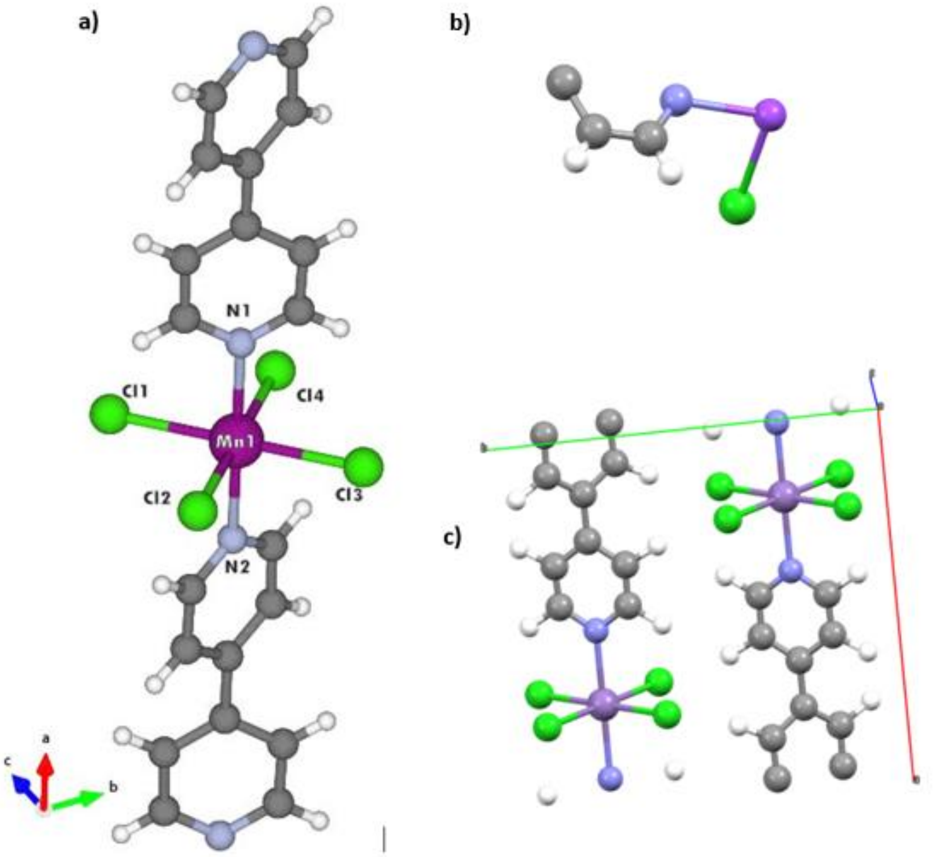

Figure 39. Structure of Mn-ma-bpy. a) Coordination of Mn (II), b) Asymmetric unit, c) Unit cell. a) was obtained using VESTA and b) and c) Mercury.*

The macro structure show only interconnection in two directions, a and c, but there is not any connection between chain in b direction this is clear in Figure 40, it is clear in the projection on c plane the displacement on the chain that is not visible in the projection on a and b planes, in the a and b projection it is visible the channel formed between the chains. Although the initial expectation was synthetized a tridimensional MOF, the steric hindrance of 4,4 bipyridine to coordinate in more positions which also affect the angles of chloride bridges.[63] Mn-ma-bpy* agrees with all characterization technique, so it is the first MOF elucidated completely.

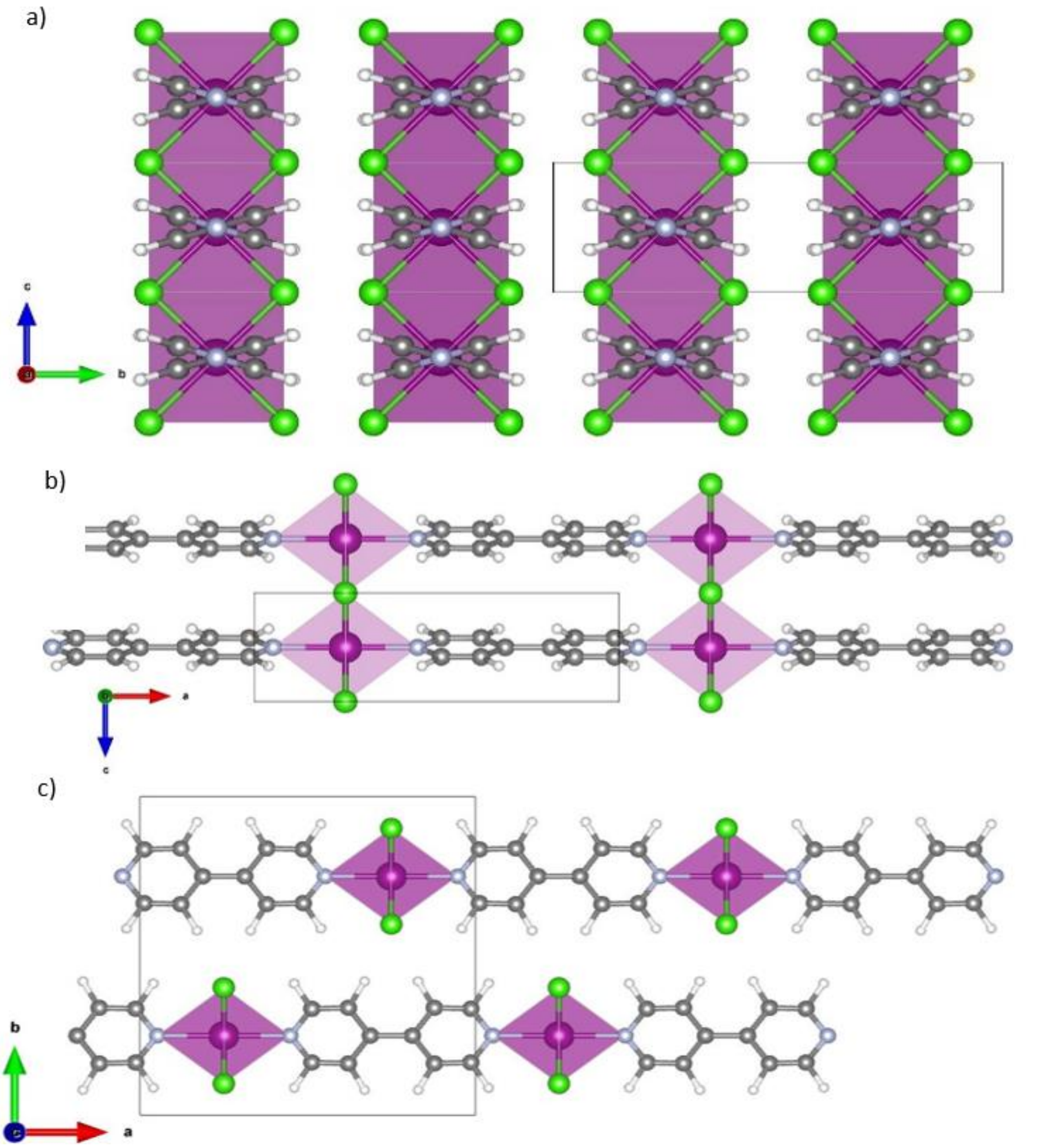

Figure 40.Mn-ma-bpy phase simulation projected on planes. a) projection on a, b) projection on b and c) projection on c. All graphs have the polyhedron representation of Mn (II) coordination.*

5.6 Compounds of cobalt, 4,4-bipyridine and maleic acid (AEEP002)

5.6.1 Attenuated Total Reflectance FTIR spectroscopy

The sample AEEP002 does not form any precipitate, in the analysis is referred as Co-ma-bpy, and on its FTIR spectrum (Figure 41), it is notable the presence of maleic acid and 4,4-bipyridine by the representative bands presented in Table 13. The band A was assigned to CH sp^2 stretching of maleic acid and 4,4 bpy, the peaks B, C and D are from O-H stretching, carbonyl group and C=C stretching of maleic acid respectively, the bands F and H are assigned to the asymmetric and symmetric carboxylate stretching respectively[46], although the band F also overlaps the quadrat stretching form 4,4-bpy and peak H presents a near shoulder as result of nitrate band overlapping ; others peaks related with maleic acid are I and L which belong to C-O stretching and cis C-H out of plane. On the other hand, regarding with 4,4-bipyridine the bands E, G and J are assigned to C=N stretching, bipyridine semicircle stretching and C-N stretching interaction; while the coordination peaks for Mn-N and Mn-O interaction are M and N respectively[42,54,61].

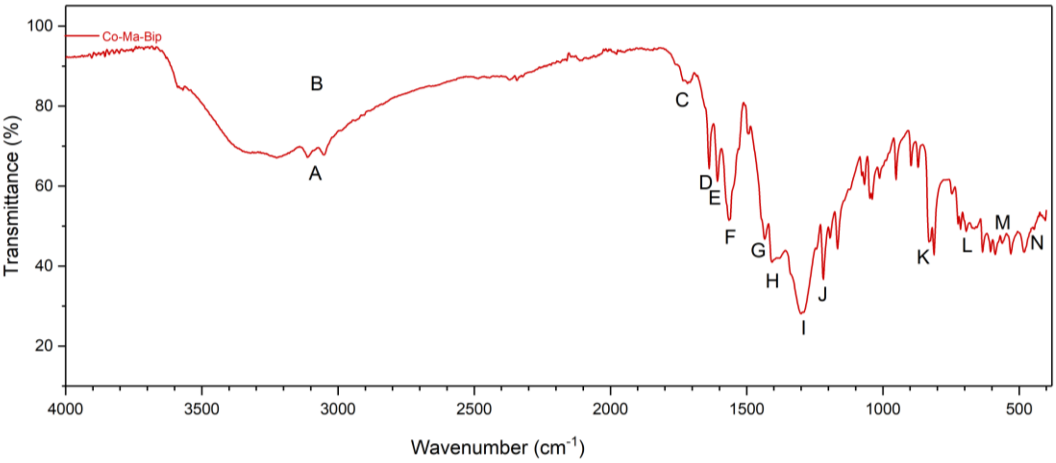

Figure 41.IR bands assignations for Co-ma-bpy sample.

Table 13. IR bands assignations for Co-ma-bpy sample.

Band	Frequency (cm^{-1})	Type of vibration
A	3100 and 3050	alkene sp2 CH stretching
B	3500 -2400	-OH
C	1714	-C=O
D	1635	-C=C stretching acid
E	1600	-C=N
F	1570	-COO- asymmetric carboxylate, overlapped quadrant stretching
G	1425	Semicircle stretching
H	1405	-COO- symmetric carboxylate, nitrate
I	1300	-C-O stretching
J	1220	-C-N stretching
K	830	2 adjacent H wag
L	700	=CH cis out of plane
M	564	Co-N
N	430	Co-O

5.6.2 UV-Vis transmittance spectroscopy

The UV-Vis diffuse reflectance spectrum of Co-ma-bpy show three electronic transitions, the transition under 400 nm is from LCMT, but the other two transitions are attributed to d-d transitions from cobalt (II) ion in coordination, but it is important to consider the ligands which affect the splitting of crystal field of coordination in this case the UV-Vis spectrum shows a high spin configuration and it is reasonable for the ligands identified in the FTIR spectrum the maleic acid and water molecules should be coordinated with cobalt in higher proportion than 4,4-bipyridine which is a strong field ligand as N-donor .[5,51] The d-d transitions occurs at 527 nm and 685 nm which correspond to 18975.33 cm^{-1} and 14598.54 cm^{-1} and are assigned to $^4T_{1g} \rightarrow {}^4A_{2g}$ and $^4T_{1g} \rightarrow {}^4T_{2g}$ transitions.

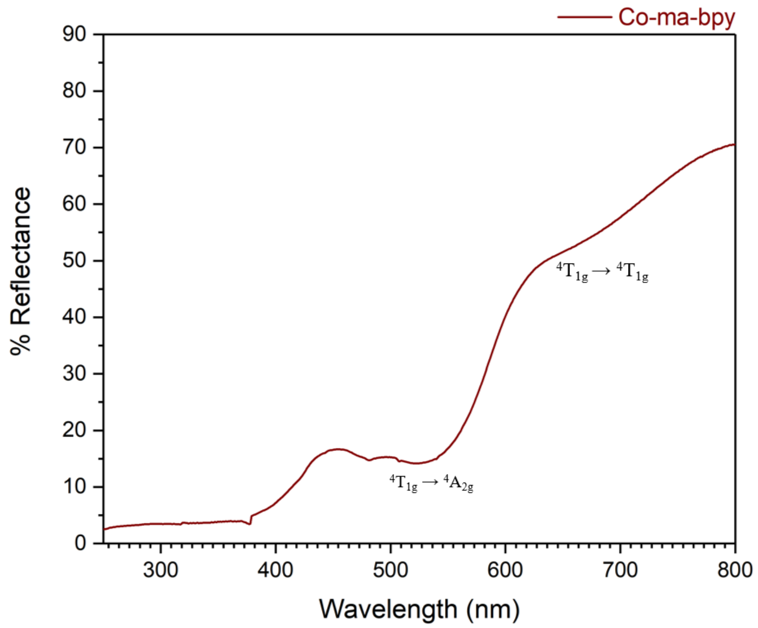

Figure 42. Diffuse reflectance UV-Vis spectrum of Co-ma-bpy.

5.6.3 X-Ray Powder Diffraction of Co-ma-bpy

The experimental diffractogram (Co-ma-bpy) had too much noise as result of fluorescence of Cobalt (II) ion because emit radiation near to the X-ray wavelength from Cu lamp, therefore the spectrum was refined on QualX software for smoothing, although it can lose information. In the XRD phase analysis an isostructural phase was identified in the CCDC data base, although this phase is present in minority proportion, this is clear in the XRD pattern comparison in Figure 43.

The phase found in CCDC database is catena-[bis(\m~2~-4,4'-Bipyridyl)-diaqua-cadmium(ii) dinitrate tetrahydrate, this phase only present 4-4 bipyridine as ligand and the metallic center is Cd (II), then a new simulated phase was optimized replacing Cd (II) ion by Co (II) ion in Quantum Espresso and then the XRD of Cd (II) and Co (II) phases was calculated on Mercury Software. The smoothed XRD pattern (Co-ma-bpy) is shown in Figure 43 and have many peaks which do not correspond with simulated phase neither Cd (II) phase, it infers that there are more phases present which cannot be identified.

The identified phase and simulated phase corresponded to monoclinic system and their crystallographic data is tabulated in Table 14. The simulated Co(II) phase describe a distorted octahedral coordination of cobalt formed by four 4,4 bipyridine and two water molecules; in this coordination any bond length is equal, although the bond length between Co(II) ion and oxygen are more similar, but lengths of nitrogen coordination with cobalt(II) has different lengths in decreasing order as Co1-N4, Co1-N1, Co1-N3 and Co1-N2, also the values of the bond angles are tabulated in Table 15 and sketched in Figure 44 a).

These distortions can be attributed by the interactions out of the metal coordination sphere, those interactions are between water molecules in the coordination sphere by hydrogen bonds with other water molecules and nitrates as is shown in Figure 44 c), this interactions are even more visible in the asymmetric unit Figure 44 b).

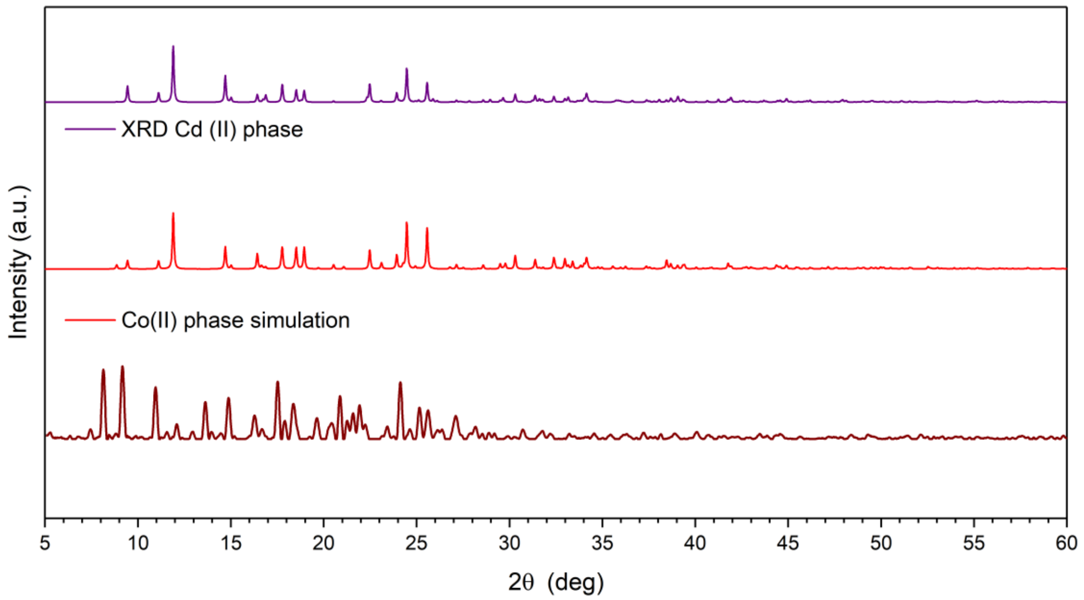

Figure 43. XRD patterns for Co-ma-bpy structure determination. The phase found by geometry optimization is referred as Co (II) phase simulation, the XRD Cd (II) phase is the phase found by phase comparison in Smart Lab Studio II and the experimental pattern is labeled as Co-ma-bpy.

Table 14. Crystallographic data of Cd(II) phase and Mn(II) simulated phase

	Cd(II) phase	**Co-simulated phase**
Chemical Formula	$(C_{20}H_{20}CdN_4O_2{}^{2+})_n,2(NO_3{}^{-})_n,4(H_2O)_n$	$(C_{20}H_{20}CoN_4O_2{}^{2+})_n,2(NO_3{}^{-})_n,4(H_2O)_n$
Molecular Weight	636.72 g/mol	583.24 g/mol
Radiation	Kα= 1.54056 Å	Kα= 1.54056 Å
Crystalline system	Monoclinic	Monoclinic
Space group	C 2/c	C 2/c
Cell parameters	**a** 18.8822	**a** 18.882200
	b 11.7880	**b** 11.788101
	c 12.1449	**c** 12.145009
	β 96.65	β 97.489
Volume	2680.19	2680.24

Table 15. Mn(II) coordination data in Mn-ma-bpy phase simulation, the bond lengths and bond angles related with Mn(II) are presented. The labels of atoms are from the Figure 44 in section (a))

Bond	**Length (Å)**	**Bond**	**Bond angles (°)**
Co1-N1	2.31233	N1-Co1-N2	87.6555
Co1-N2	2.15381	N2-Co1-N3	89.4462
Co1-N3	2.25453	N3-Co1-N4	91.6524
Co1-N4	2.32157	N4-Co1-N1	91.2440
Co1-O1	2.37137	N1-Co1-O1	85.8118
Co1-O2	2.36912	N2-Co1-O1	96.9286
		N1-Co1-O2	92.1309
		N2-Co1-O2	96.9951

The Co (II)simulated phase (Figure 45) is a 2D MOF, the channels formed by 4,4 bipyridine bridges are visible in a) and c), although these channels are partially occupied with water molecules and nitrates which have hydrogen bonds between them and 2D-channels, this interactions stabilize the complete structure and although in b) there is not any strong interaction to consider any formation of three dimensional MOF.

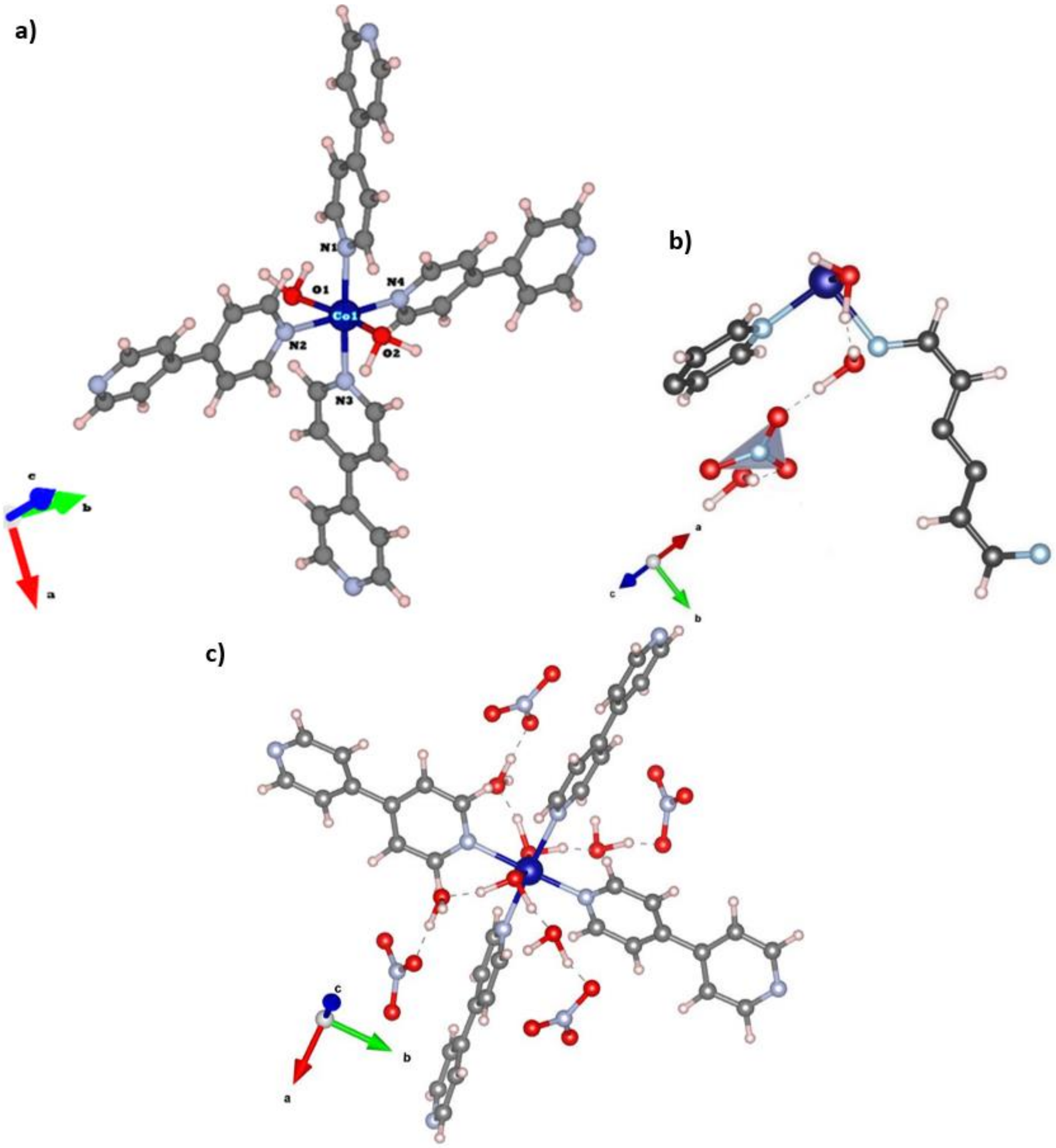

Figure 44. Coordination of Co (II) in simulated phase. a) Coordination of Co (II). b) Asymmetric unit of simulated phase. c) Near interactions with coordination sphere.

It is important to clarify that this phase is a minority one and the principal phase with maleic acid in the coordination sphere is not elucidated already, this phase should be consistent with FTIR and diffuse reflectance UV-Vis spectrum, because this phase should have peaks only from 4,4-bipyridine in ATR-FTIR spectrum and UV-Vis spectrum for a low spin d^7 configuration by 4,4-bipyridines as N-donor ligand, while the main phase have a high spin configuration as result of coordination of maleic acid and water molecules.

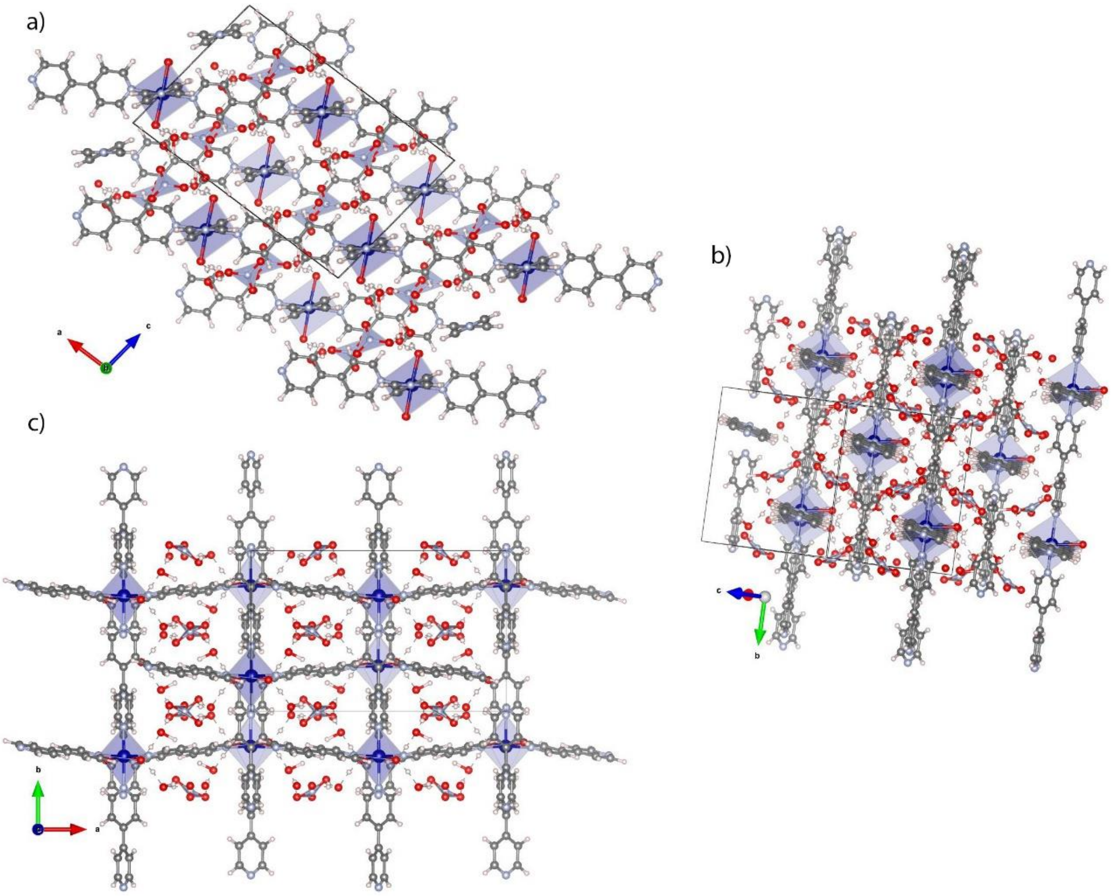

Figure 45. Co (II) simulated phase projected on planes. All graphs have the polyhedron representation of Co (II) coordination.

5.7 Compounds of zinc, 4,4-bipyridine and maleic acid (AEEP003)

5.7.1 Attenuated Total Reflectance FTIR spectroscopy

The sample AEEP003 does not form any precipitate, so this sample must be dried for two weeks until get a dried powder able to XRD analysis. This sample is referred as Zn-ma-bpy in the following tables and graphs. In the Zn-ma-bpy ATR-FTIR spectrum (Figure 46), there are bands from 4,4 bipyridine and maleic acid; the bands associated with maleic acid are A, B and C which are assigned to CH alkene stretching, OH stretching and C=C stretching, respectively; the peaks related with carboxylate asymmetric and symmetric are E and F[46], although these peaks overlap quadrant stretching and nitrate bands respectively[42,54], while the peak G is assigned to CO stretching; on the other hand, peaks belong to 4,4-bipyridine are D, H and I which are assigned to C=N stretching, C-N stretching and H wag of hetero atom cycle. [48,61] The coordination between

Zn(II) nitrogen and oxygen are visible in bands K and L[52,64]; the specific values are tabulated in Table 16 and sketched in Figure 46. This characterization technique infers that the coordination of Zn(II) should include 4,4 bipyridine, maleic acid and water molecules.

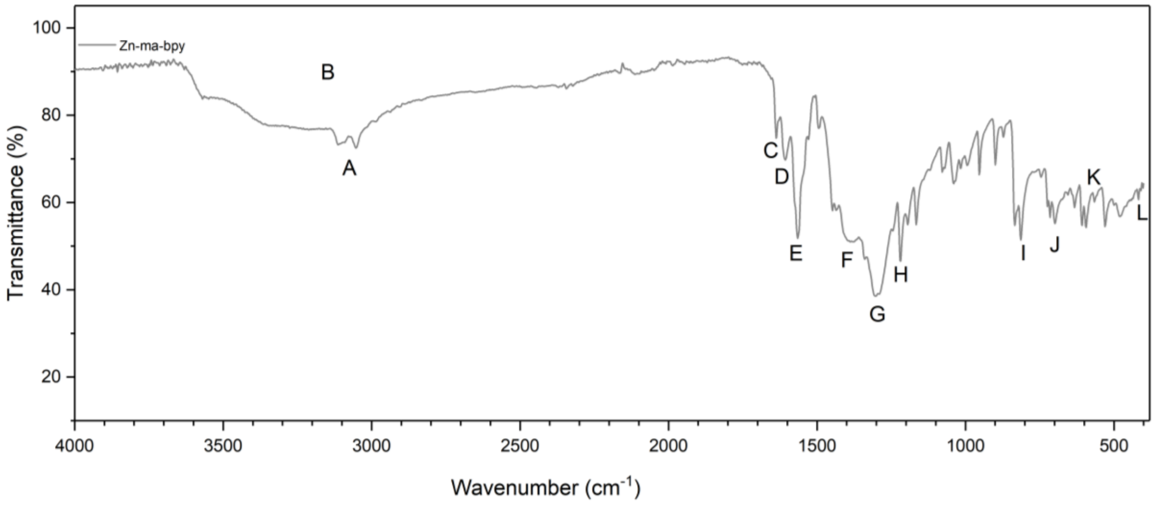

Figure 46. ATR-FTIR spectrum of Zn-ma-bpy.

Table 16. IR bands assignations for Zn-ma-bpy sample.

Band	Frequency (cm^{-1})	Type of vibration
A	3050,3100	alkene sp2 CH stretching
B	3500 -2400	-OH
C	1640	-C=C
D	1602	-C=N
E	1560	-COO- asymmetric carboxylate, overlapped quadrant stretching
F	1405	-COO- symmetric carboxylate, nitrate
G	1300	-C-O stretching
H	1220	-C-N stretching [48]
I	813	2 adjacent H wag
J	700	-C=C- cis out of plane
K	566	Zn-N
L	417	Zn-O

5.7.2 Diffuse Reflectance UV-Vis Spectroscopy

In diffuse reflectance UV-Vis spectrum of Zn-ma-bpy (Figure 47), there is no any electronic transition in visible region of the electromagnetic spectrum as is expected for Zn (II) ion which have $3d^{10}$ electronic configuration therefore no d-d transitions are possible and the yellowish color is attributed to LCMT.

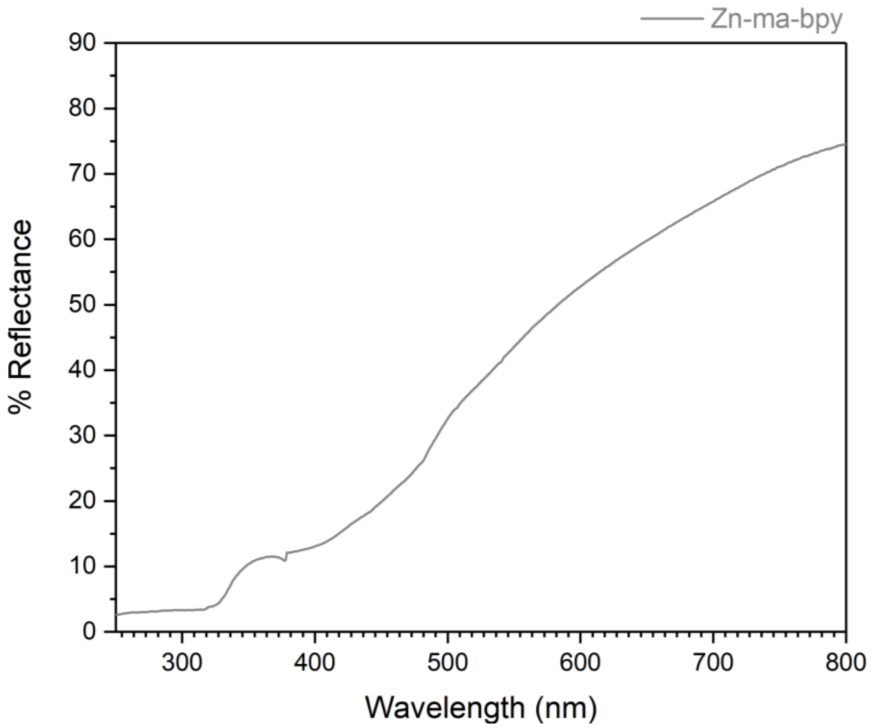

Figure 47. Diffuse reflectance UV-Vis spectrum of Zn-ma-bpy

5.7.3 X-Ray Diffractometry

The X-Ray diffractogram taken from sample Zn-ma-bpy was taken after an exhausted drying of sample although any considerable crystal was formed but this sample was manageable to take the diffractogram, also this sample does not absorb water as the other metal samples. The diffractogram was refined on Qualx2 software and then analyzed to find any reported phase; the phase identified is the same of sample AEEP002 that could be possible because both has the same counter ion and ligand as catena-[bis(\m~2~-4,4'-Bipyridyl)-diaqua-cadmium(ii) dinitrate tetrahydrate identified in CCDC database. The identified phase was optimized replacing the Cd (II) ion by Zn (II) ion by computational methods in Quantum-Espresso and then its XRD pattern was calculated in Mercury. The simulated phase corresponds to a monoclinic system and its crystallographic data is tabulated in Table 17. In Figure 48 the XRD patterns are compared and it is clear that Cd(II) identified phase and simulated Zn-phase are not the main phase in the sample Zn-ma-bpy because there are many peaks which not match, also, this preposition is supported by FTIR spectrum because the synthetized phase should have 4,4- bipyridine and maleic acid in the coordination, but the Zn simulated phase only include 4,4-bipyridine in metal coordination.

Table 17. Crystallographic data of Cd (II) phase and simulated phase of Zn (II) by Quantum Espresso.

	Cd(II) phase	**Zn-simulated**
Chemical Formula	$(C_{20}H_{20}CdN_4O_2^{2+})_n,2(NO_3^-)_n,4(H_2O)_n$	$(C_{20}H_{20}ZnN_4O_2^{2+})_n,2(NO_3^-)_n,4(H_2O)_n$
Molecular Weight	636.72 g/mol	589.70 g/mol
Radiation	Kα= 1.54056 Å	Kα= 1.54056 Å
Crystalline system	Monoclinic	Monoclinic
Space group	C 2/c	C 2/c
Lattice parameters	**a** 18.8822	**a** 18.882200
	b 11.7880	**b** 11.788101
	c 12.1449	**c** 12.145009
	β 97.489	β 97.489189
Volume	2680.19	2680.24

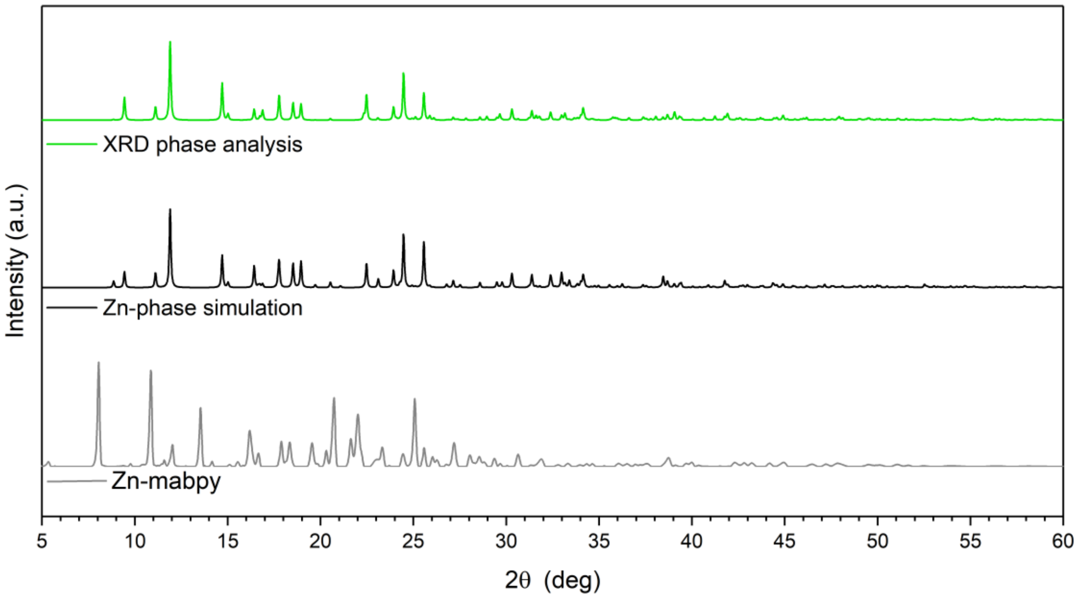

Figure 48. XRD patterns for Zn-ma-bpy structure determination. The phase found by geometry optimization is referred as Zn-phase simulation, the XRD Cd (II) phase is the phase found by phase comparison in Smart Lab Studio II and the experimental pattern is labeled.

Table 18. Zn (II) coordination data in Mn-ma-bpy phase simulation, the bond lengths and bond angles related with Zn (II) are presented. The labels of atoms are from the Figure 49 in section (a)).

Bond	Length (Å)	Bond	Bond angles (°)
Zn1-N1	2.24589	N1-Zn1-N2	86.6426
Zn1-N2	2.29595	N2-Zn1-N3	93.1308
Zn1-N3	2.23174	N3-Zn1-N4	93.3694
Zn1-N4	2.28314	N4-Zn1-N1	86.8572
Zn1-O1	2.11572	N1-Zn1-O1	94.5371
Zn1-O2	2.11595	N2-Zn1-O1	87.4087
		N1-Zn1-O2	94.5292
		N2-Zn1-O2	92.8256

The Zn simulated phase correspond to octahedral coordination of Zn(II), the coordination sphere is formed of four 4,4-bipyridines and two water molecules, the bipyridine are organized in the sample with water molecules in the perpendicular plane, the coordination sphere is shown in the Figure 49 and the values of coordination are tabulated in Table 18, this data shows a compressed octahedral coordination with larger bond lengths with nitrogen and shorter bond distances with oxygen from water, although the interactions with water and nitrates should be taken in account as is shown in Figure 49 (b)) where even the asymmetric unit include water molecule and nitrates joined by hydrogen bridges Figure 49 (c)). The coordination bonds lengths of Zn1-O1 and Zn1-O2 are very similar, and the same thing happens with nitrogen bonds in opposite positions therefore Zn-N1 and Zn1-N3 has similar bond length and larger than Zn1-O2 and Zn1-O4 bonds, this distortion is appreciable in Table 18. The Zn (II) simulated phase suggest a 2D MOF with channels formed by 4,4 bipyridines in a and b directions (Figure 50), while waters in coordination nor form any strong bond with channels but they interact with other water molecules and nitrates near the coordination sphere by hydrogen bonds, although this interaction stabilize the final structure of MOF. The * bipyridine bridges are extended in a and b directions, also in projection on the plane b the displacement between the chains is visible in Figure 50 section a).

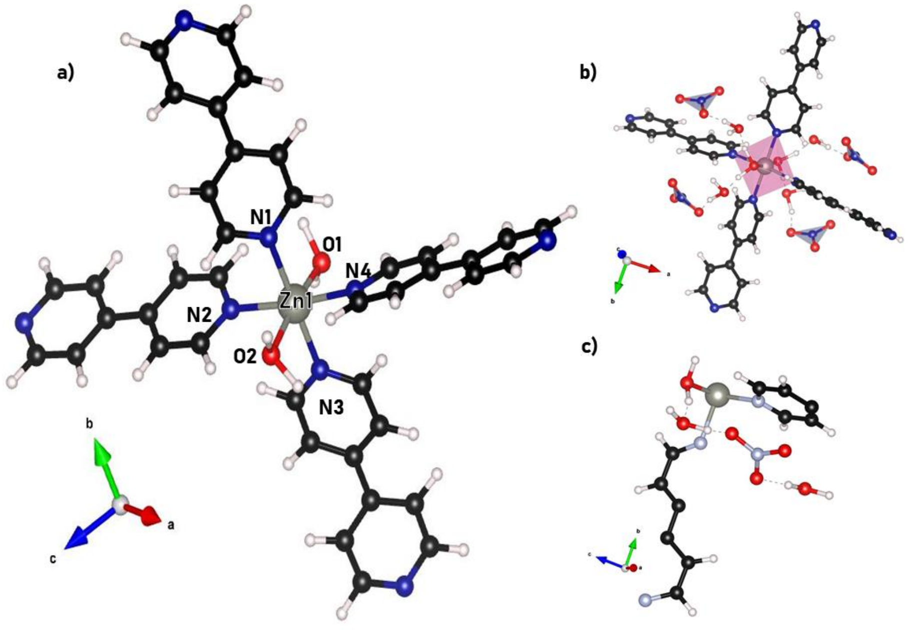

Figure 49. Coordination of Zn (II) in simulated phase. a) Coordination of Zn (II). b) Near interactions with coordination sphere. c) Asymmetric unit of Zn (II) phase.

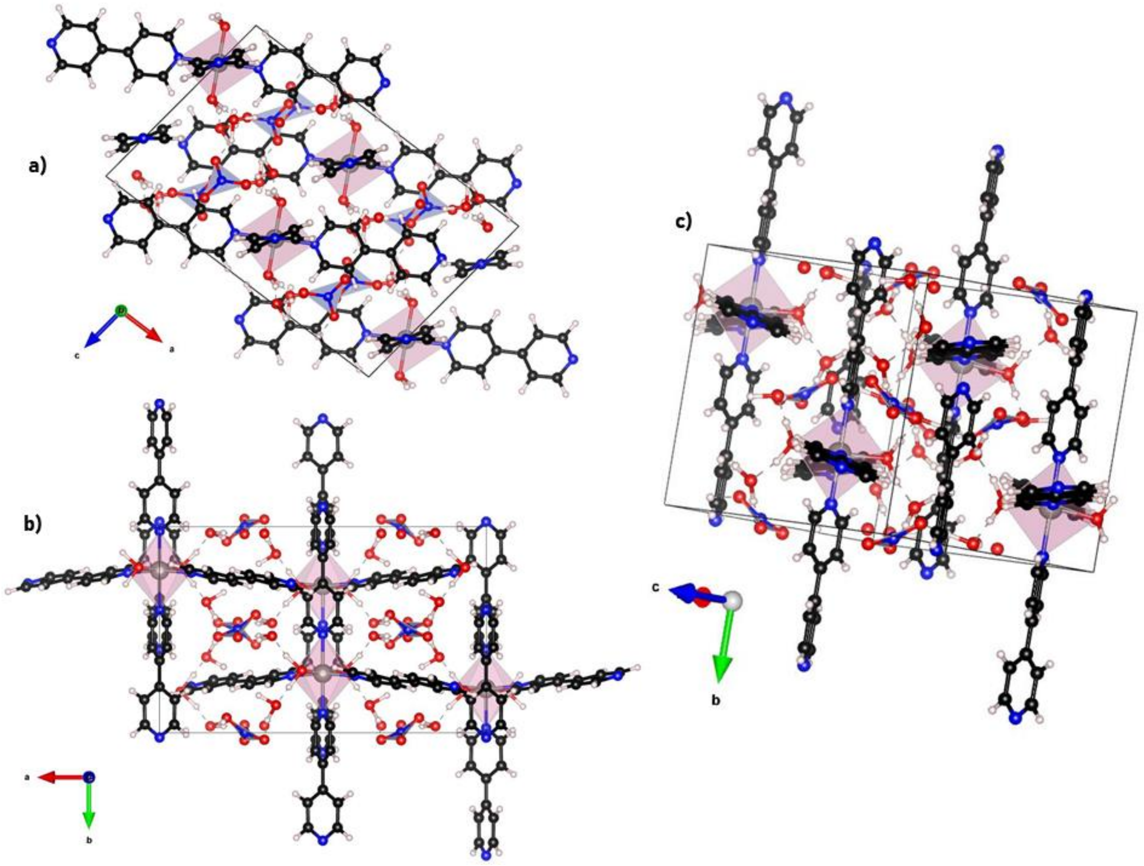

Figure 50. Zn (II) simulated phase projected on planes. All graphs have the polyhedron representation of Zn (II) coordination.

5.8 Compounds of copper, 4,4-bipyridine and maleic acid (AEEP004)

5.8.1 Attenuated Total Reflectance FTIR spectroscopy

The sample AEEP003 was the last one synthetized in the third stage of synthesis, this sample formed two main phases one soluble in water and a precipitate, the soluble phase is referred as Cu-ma-bpy and the precipitate as Cu-ma-bpy*; in the following characterization techniques each sample was dried although Cu-ma-bpy absorbed water rapidly this hydroscopic property difficult the X-Ray Diffractometry for this sample. In the FTIR spectra (Figure 51), the phase Cu-ma-bpy present bands belong to 4,4 bipyridine and maleic acid and the specific values on transmittance peaks are tabulated in Table 19; on the other hand, the Cu-ma-bpy phase only have bands from 4,4 bipyridine. The Cu-ma-bpy* present well defined bands that characterize the amines FTIR spectra, the bands A, E, H, K and L are assigned to unsaturated CH stretching, C=N stretching, semicircle stretching, C-N stretching and 2 adjacent H wag from 4,4-bipyridine respectively, while peak N regard to the Zn-N coordination. The FTIR spectrum from Cu-ma-bpy present the same peaks of precipitated phase, although the peaks from maleic acid too; the bands B, C and D are assigned to OH stretching, carbonyl and C=C stretching respectively, the first clue of maleic acid coordination is the asymmetric and symmetric carboxylates peaks correspond to F and I, but those peaks are overlapped in peaks E and H respectively; the bands J and M are from CO stretching and cis CH out of plane movement and, Cu-O and Cu-N bonds could be responsible of peaks N and O.

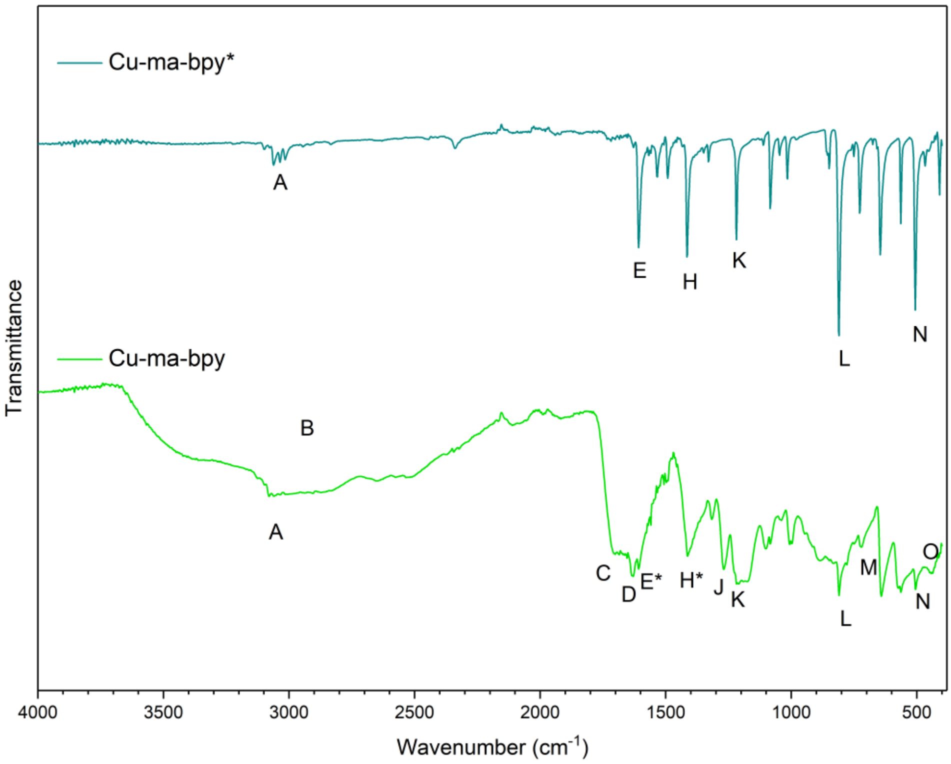

Figure 51. ATR-FTIR spectrum of AEEP004. Cu-ma-bpy is the precipitated phase and Cu-ma-bpy is hydro soluble phase.*

Table 19. Specific values for IR bands assigned to Cu-ma-bpy and Cu-ma-bpy.*

Band	Type of vibration	Cu-ma-bpy*	Cu-ma-bpy
A	alkene CH stretching	3020, 3040, 3060	3080
B	-OH	-	3600 -2400
C	-C=O	-	1710
D	-C=C stretching acid	-	1630
E	-C=N[61]	1610	1607*
F	-COO- asymmetric carboxylate[46],	-	1607*
H	Semicircle stretching	1415	1412*
I	-COO- symmetric carboxylate[46]	-	1412*
J	-C-O stretching	-	1268
K	-C-N stretching [48]	1218	1218
L	2 adjacent H wag	810	811
M	-C=C- cis oop [53]	-	710
N	Cu-N	562	560
O	Co-M	-	435

5.8.2 UV-Vis spectroscopy

Diffuse reflectance UV-Vis spectrum of Cu-ma-bpy was realized because of the small quantity produced was lost in the XRD analysis. The UV-Vis spectrum of Cu-ma-bpy* (Figure 52) shows an expected d-d absorption for Cu (II) ion as d^9 transition metal, according with FTIR spectrum only 4,4 bipyridine is in the coordination of Cu (II), but there is only one electronic arrangement independently if the crystal field is strong as in this time. Cu-ma-bpy is greenish opaque compound and its d-d transition occurs at 679 nm from Cu (II) ion coordinated and transition lower than 400 nm is from LMCT.

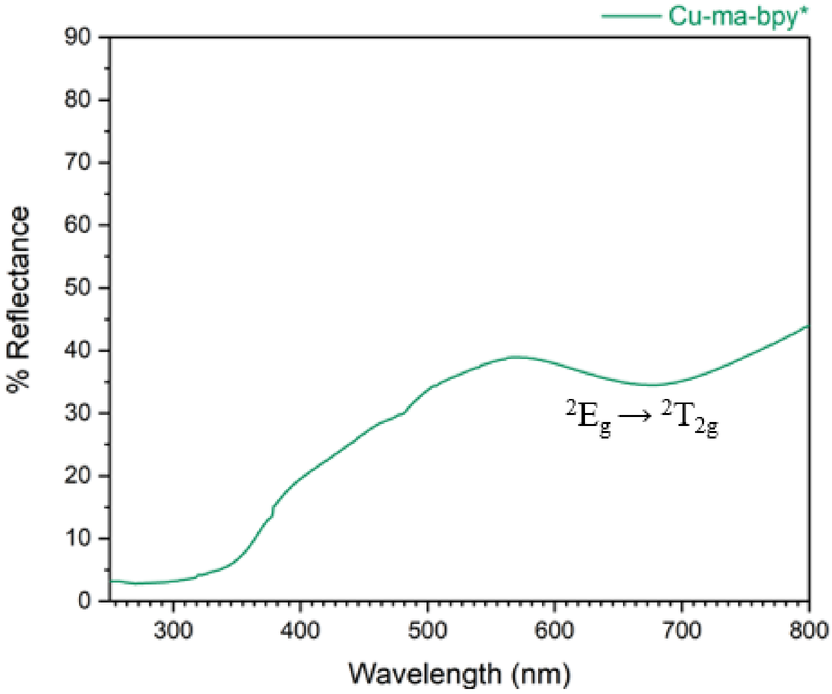

Figure 52. Diffuse reflectance UV-Vis spectrum of Cu-ma-bpy.*

5.8.3 X-Ray Diffractometry

The Cu-ma-bpy was not able to take the XRD pattern because it can remain less than a minute dried, so it produces too much noise in the XRD pattern. The Cu-ma-bpy* sample is a pale greenish precipitate; this compound is not hydroscopic and easy to dry than the other samples. The isostructural phase found in CCDC database by XRD analysis in SmartLab Studio II was catena-[bis(m-2-chloro)-(m-2-4,4'-bipyridyl)-cadmium(II)] reported by Chunhua Hu and his team in 2003[63]. The copper phase was simulated based on the Cd (II) but changing the metal center by Cu (II), the optimization was performed in Quantum Espresso and both XRD patters were calculated in Mercury software. The experimental, Cd (II) phase and simulated phase XRD patterns are compared in Figure 53 therefore is correct to infer that it is the main phase of the precipitate because this phase agrees with FTIR spectrum of Cu-ma-bpy* where only the 4,4 bipyridine is identified.

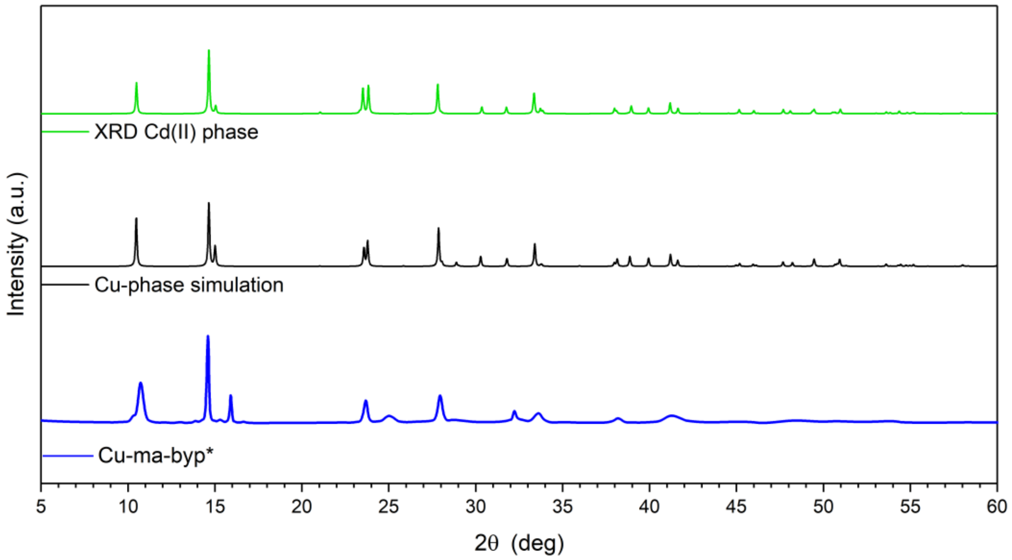

Figure 53. XRD patterns for Cu-ma-bpy structure determination. The phase found by geometry optimization is referred as Cu-phase simulation, the XRD Cd (II) phase is the phase found by phase comparison in Smart Lab Studio II and the experimental pattern is labeled.

Table 20. Crystallographic data of Cd (II) phase and simulated phase of Cu (II) by Quantum Espresso

	Cd (II) phase	**Cu(II)-simulated**
Chemical Formula	$(C_{10} H_8 Cd Cl_2 N_2)_n$	$(C_{10} H_8 Cu Cl_2 N_2)_n$
Molecular Weight of repetitive unit	339.50 g/mol	290.64 g/mol
Radiation	Kα= 1.54056 Å	Kα= 1.54056 Å
Crystalline system	Orthorhombic	Orthorhombic
Space group	P b a n	P b a n
Lattice parameters	**a** 11.796	**a** 11.796300
	b 12.084	**b** 12.084294
	c 3.7716	**c** 3.771690
	□ 90 □ 90 □ 90	**a** 90 **b** 90 90
Volume	537.615	537.654

Table 21. Cu (II) coordination data in Cu-ma-bpy phase simulation, the bond lengths and bond angles related with Cu (II) are presented. The labels of atoms are from the Figure 39 in section (a)).*

Bond	Length (Å)	Bond	Bond angles (°)
Cu1-N1	2.33517	Cl1-Cu1-Cl2	91.5590
Cu1-N2	2.33542	Cl2-Cu1-Cl3	88.3951
Cu1-Cl1	2.63223	Cl3-Cu1-Cl4	91.7183
Cu1-Cl2	2.63063	Cl4-Cu1-Cl1	88.3275
Cu1-Cl3	2.62708	N1-Cu1-Cl1	89.9755
Cu1-Cl4	2.62868	N1-Cu1-Cl2	89.9760
		N2-Cu1-Cl1	89.9770
		N2-Cu1-Cl2	89.9765

Crystallographic data of Cd (II) and Cu simulated are presented in Table 20; according to lengths and angles of coordination, the simulated Cu (II) phase has an octahedral coordination with four chlorides in same plane and two 4,4-bipyridines perpendicularly, this octahedron is compressed in bipyridines, while the chloride bonds are larger; also the angles confirm the slight distortion of the octahedron with values near to 90 degrees as shown in Table 21, this distortions can be produced by the interaction of chloride as bridges between the chains of bipyridines[63] (Figure 55 a)). The chlorides have the function of counter ion and bridges between the Cu (II) ion.

According with simulation Cu-ma-bpy* is a 2D MOF, the channels are formed by 4,4 bipyridine bridges in a direction and chloride bridges in c direction while in b direction there is any bond formed between bidirectional molecular framework, the channels formed follow the b direction and they are empty. In this case all characterization techniques confirm the formation of this phase, although the displacement of chains in a direction reduces the size of channels in b direction (Figure 55).

All characterization techniques agree ad infer that this is the second coordination polymer synthetized successfully.

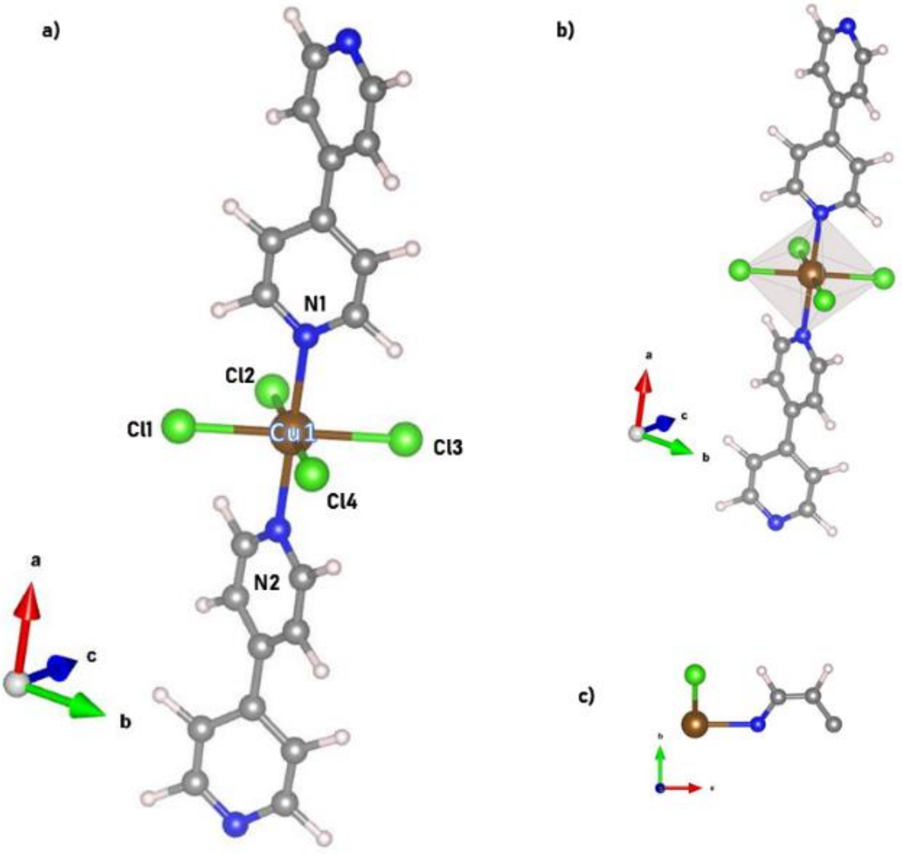

Figure 54. Coordination of Cu (II) in simulated phase. a) Coordination of Cu (II). b) Near interactions with coordination sphere. c) Asymmetric unit of Cu (II) phase.

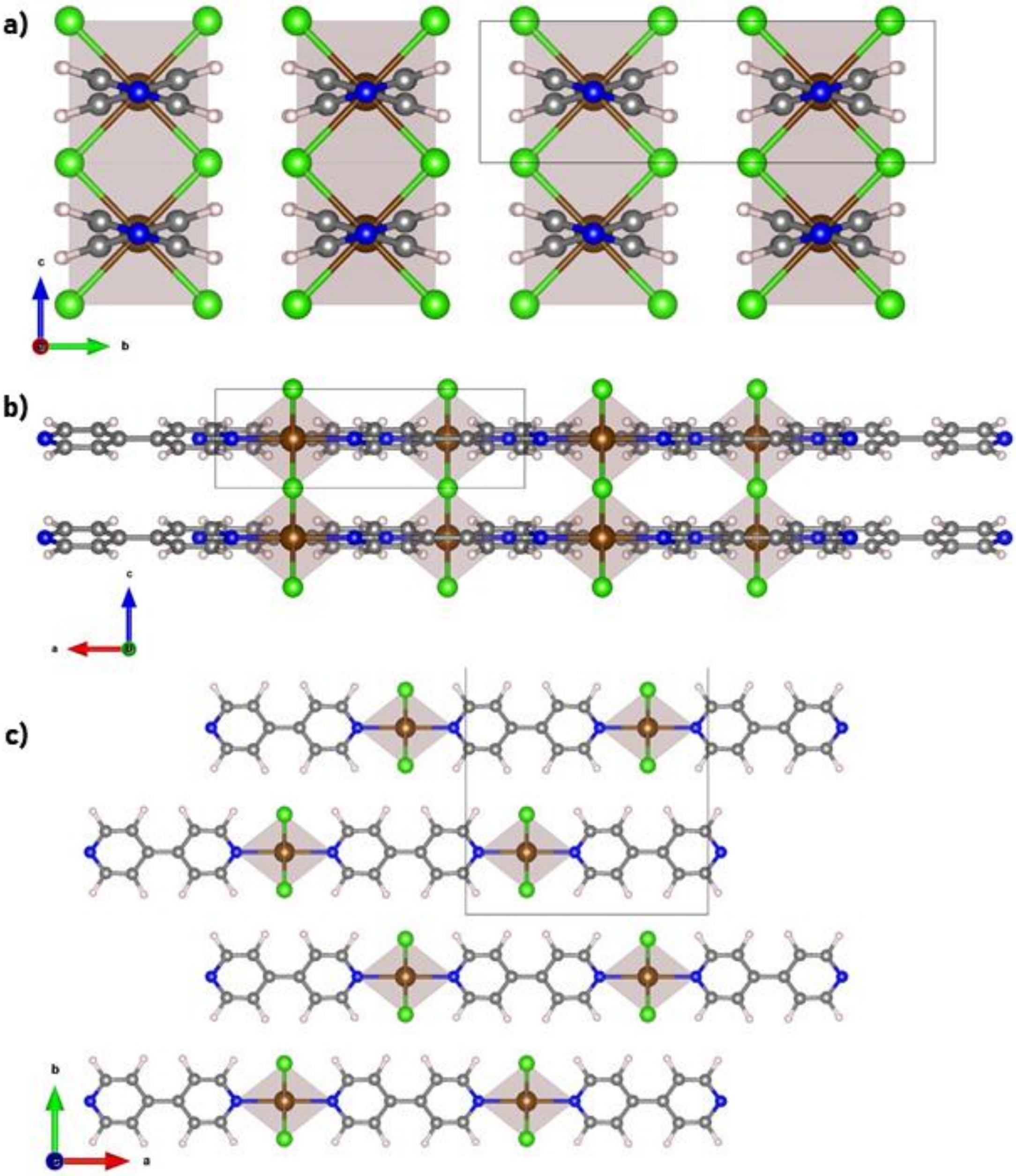

Figure 55. Cu-ma-bpy phase simulation projected on planes. a) projection on a, b) projection on b and c) projection on c. All graphs have the polyhedron representation of Cu (II) coordination.*

5.9 Coordination Simulation

All the ligands used in the present part were geometrically optimized by ORCA, using the basis-set def2-svp, method B3LYP and atom-pairwise dispersion correction B3BJ; all the optimization uses the same parameters for their calculus, their inputs are in APENDIX I. All optimized ligands are in Figure 56, those ligands are used in different computational calculations.

4,4-bipyridine and maleic anhydride are used to establish four possible coordination for each metallic ion to study how the coordination polyhedron changes according with nature of ligands as O-donor or N-donor. In this way, all the coordination suggested are octahedral; the first coordination proposal was the metal ion coordinated with six 4,4 bipyridines, the second coordination proposal was the metal ion coordination with six maleic anhydrides, the third coordination proposal was the metal ion coordinated with four 4,4 bipyridines and two maleic anhydrides and the last one suggests the metal ion coordinated with four maleic anhydrides and two 4,4 bipyridine.

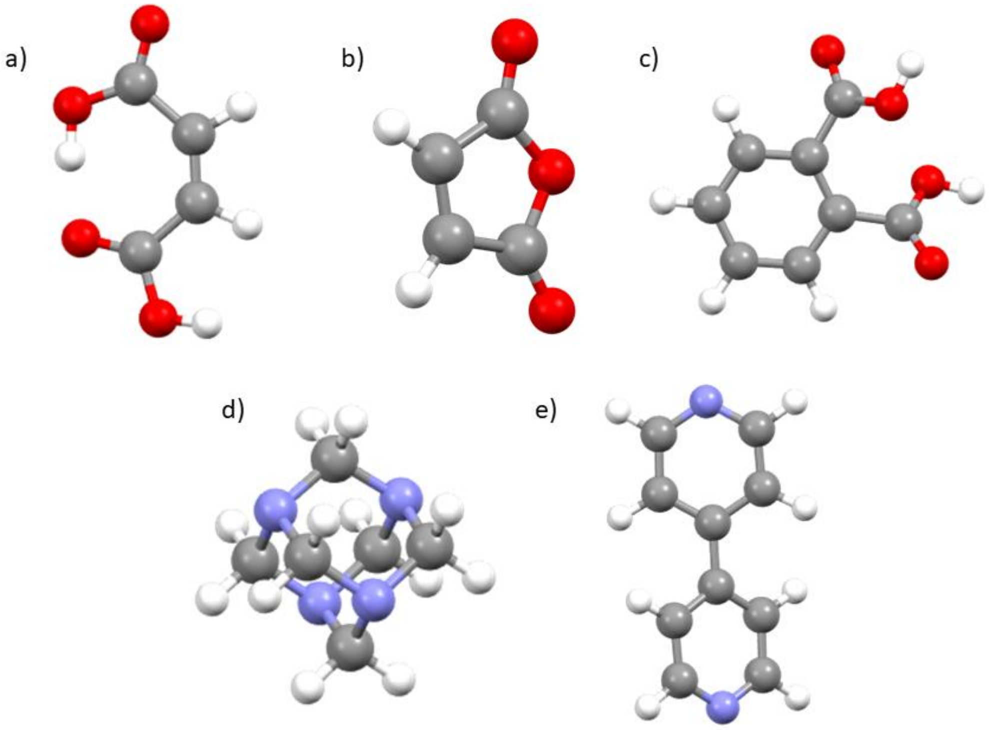

Figure 56. Optimized ligands by Orca software. a) maleic acid, b) maleic anhydride, c) phthalic acid, d) HTMA, e) 4,4-bipyridine.

First coordination proposal

The coordination of each metal is shown in Figure 57, the coordination lengths and angles are tabulated in Table 22, while the Mulliken atomic charges in Table 23. According with data, all complexes have octahedral distortion, as is expected the metal with less distortion is Zn (II) because is not susceptible to Jahn Teller effect, while Cu (II) complex has an elongated octahedral coordination in axial position (N1 and N4), Mn (II) and Co (II) have similar behavior in coordination the bond length are similar on each pair of bipyridines.

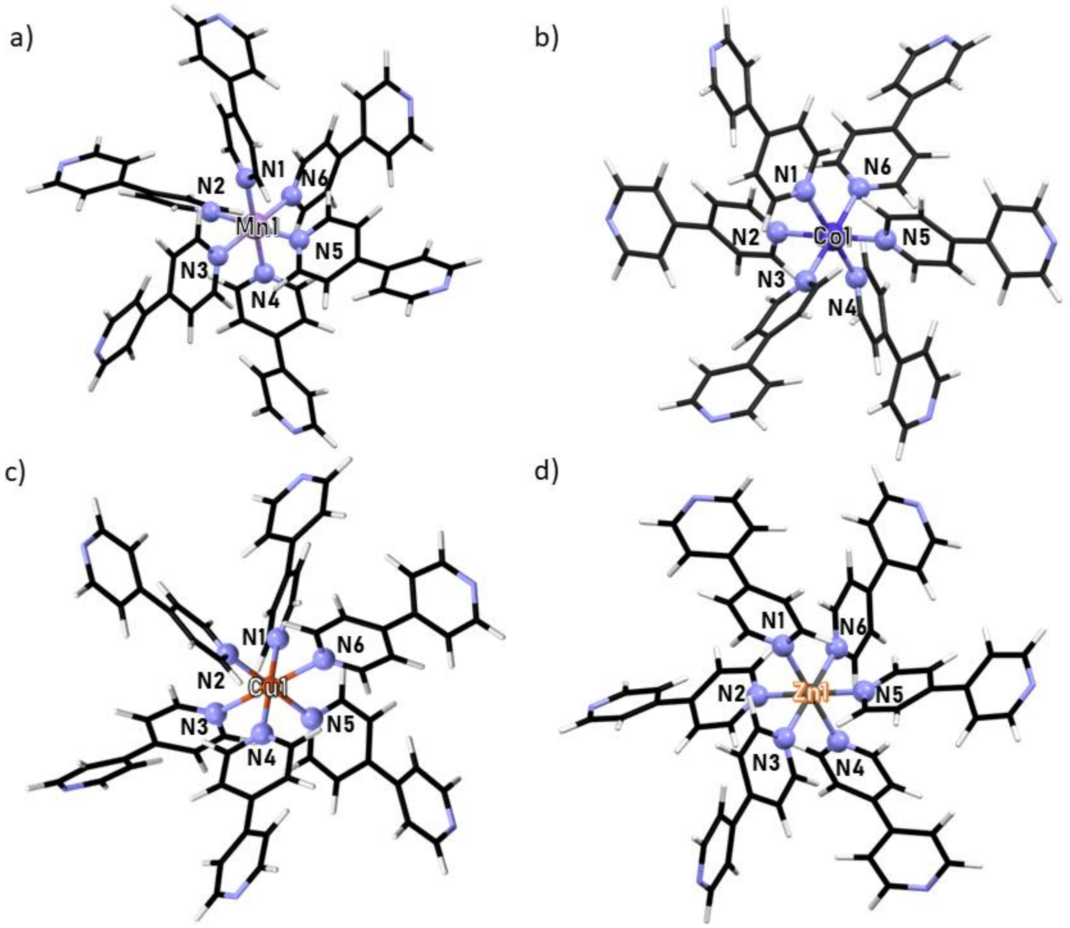

Figure 57. First coordination proposal. a) Mn (II) complex, b) Co(II) complex, c) Cu(II) complex and d) Zn(II) complex.

Table 22. Lengths and angles of coordination spheres from first coordination proposal.

Bond Lengths/ Å				
Bond	**Mn (II)**	**Co (II)**	**Cu (II)**	**Zn (II)**
M-N1	2.128	2.333	2.590	2.269
M-N2	2.090	2.342	2.094	2.246
M-N3	2.174	2.191	2.087	2.249
M-N4	2.118	2.159	2.581	2.271
M-N5	2.099	2.246	2.095	2.248
M-N6	2.167	2.237	2.087	2.254
Bond Angles/ °				
Bond	**Mn (II)**	**Co (II)**	**Cu (II)**	**Zn (II)**
N2-M-N3	91.45	91.96	89.92	89.92
N3-M-N5	89.23	89.14	90.09	89.94
N5-M-N6	90.56	89.42	89.92	90.07
N6-M-N2	88.76	89.43	90.07	90.07
N1-M-N2	90.88	87.87	89.67	90.32
N1-M-N3	90.43	87.67	90.08	89.81
N4-M-N2	88.85	89.45	90.42	89.77
N4-M-N3	89.03	93.76	89.97	90.35

Table 23. Mulliken Atomic Charges of each complex with first coordination proposal.

Mulliken Atomic Charges				
Atom	**Mn (II)**	**Co (II)**	**Cu (II)**	**Zn (II)**
N1	-0.265881	-	-0.237350	-0.246981
N2	-0.239582	-	-0.223644	-0.250842
N3	-0.243262	-	-0.208057	-0.248422
N4	-0.269721	-	-0.233405	-0.250338
N5	-0.240830	-	-0.224178	-0.250734
N6	-0.246108	-	-0.206181	-0.250509
Mn1	0.659572	-	-	-
Co1	-	-	-	-
Cu1	-	-	0.509774	-
Zn1	-	-	-	0.765909

Second coordination proposal

In the second coordination proposal, each metallic ion is coordinated with six maleic anhydrides, the angles and lengths of those coordination are shown in Figure 58 and tabulated in Table 24; although all complex has distortions in the coordination sphere, Cu(II) complex has the most distorted sphere.

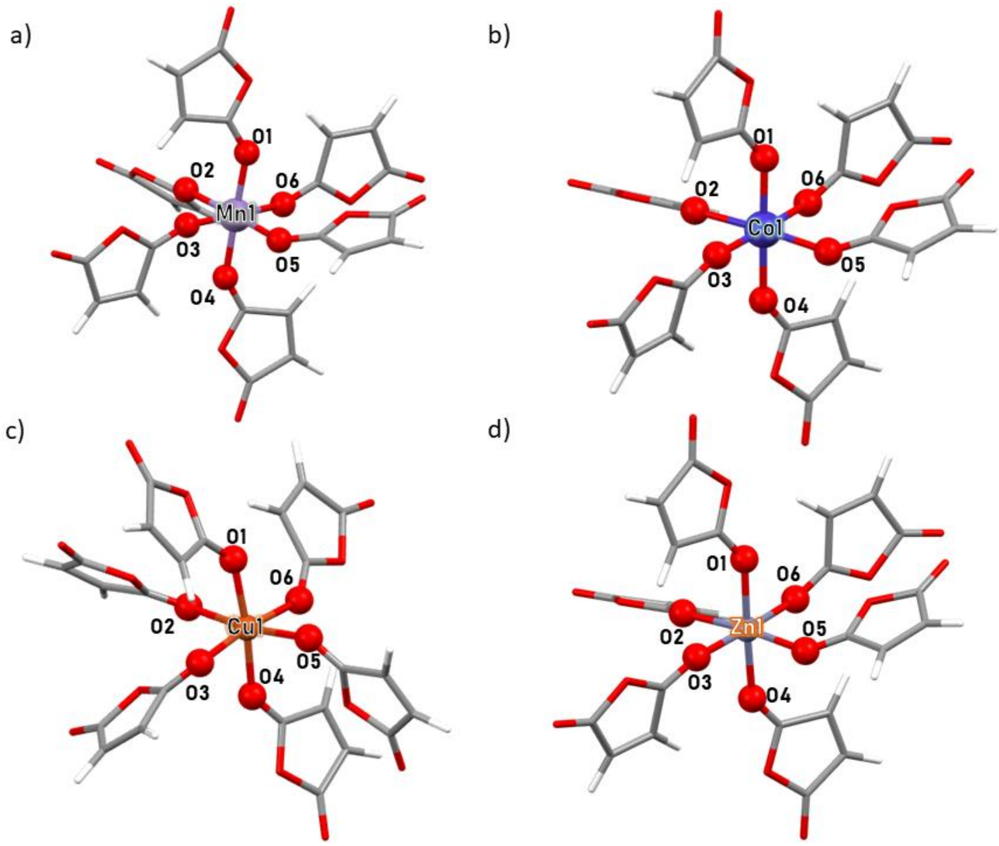

Figure 58. Second coordination proposal. a) Mn(II) complex, b) Co(II) complex, c) Cu(II) complex and d) Zn(II) complex.

Table 24. Lengths and angles of coordination spheres from second coordination proposal.

Bond Lengths/ Å				
Bond	**Mn (II)**	**Co (II)**	**Cu (II)**	**Zn (II)**
M-O1	1.988	2.069	2.000	2.074
M-O2	1.997	2.084	2.347	2.088
M-O3	2.014	2.066	2.051	2.073
M-O4	1.991	2.089	1.991	2.090
M-O5	2.024	2.147	2.310	2.142
M-O6	2.026	2.106	2.005	2.103
Bond Angles/ °				
Bond	**Mn (II)**	**Co (II)**	**Cu (II)**	**Zn (II)**
O2-M-O3	86.03	84.60	99.92	84.30
O3-M-O5	85.83	88.26	85.89	87.29
O5-M-O6	95.87	94.03	88.43	95.26
O6-M-O2	92.26	93.11	86.19	93.16
O1-M-O2	88.76	88.11	86.16	91.03
O1-M-O3	90.77	91.77	93.70	90.91
O4-M-O2	91.34	91.72	88.65	89.52
O4-M-O3	90.81	90.29	83.83	91.83

Table 25. Mulliken Atomic Charges of each complex with second coordination proposal.

Mulliken Atomic Charges				
Atom	**Mn (II)**	**Co (II)**	**Cu (II)**	**Zn (II)**
O1	-0.241769	-0.241234	-0.258921	-0.241444
O2	-0.284460	-0.311370	-0.267143	-0.295339
O3	-0.269625	-0.291833	-0.211997	-0.283341
O4	-0.258423	-0.264885	-0.264387	-0.272976
O5	-0.276984	-0.264885	-0.273134	-0.283004
O6	-0.256456	-0.279525	-0.210974	-0.316530
Mn1	0.851351	-	-	-
Co1	-	0.927113	-	-
Cu1	-	-	0.725818	-
Zn1	-	-	-	0.972487

Third and fourth coordination proposals

Both coordination proposals have the main objective to evaluate the preference in coordination of metal in the presence of both ligands, and N-donor (4,4-bipyridine) and O-donor (maleic anhydride); both coordination are octahedral, but the third proposal has a ratio 2:1 between 4,4-bipyridine and melic anhydride, while the fourth proposal has the inverse proportion of ligands. The length and angles of coordination from third and fourth coordination proposal are tabulated in Table 26 and

Table 28 respectively. The third coordination proposal formed an elongated octahedron in axial position with maleic anhydride coordination; the exception is Mn(II) complex that have shorter bond lengths on the oxygen bonds. In the fourth coordination proposal the complex of Co(II), Cu(II) an Zn(II) stabilized compressed octahedral coordination in axial positions with bipyridine coordination, otherwise, Mn(II) complex have more similar coordination lengths.

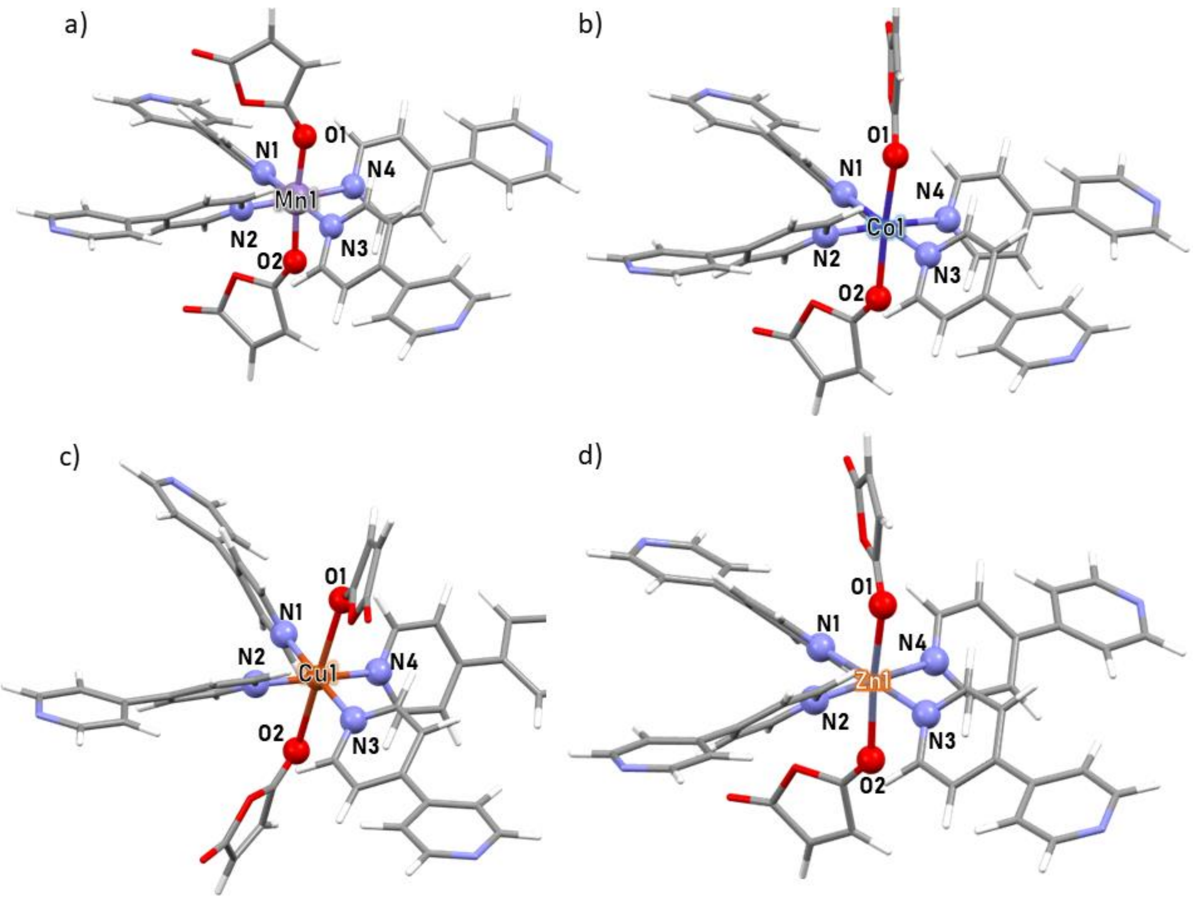

Figure 59. Third coordination proposal. a) Mn (II) complex, b) Co (II) complex, c) Cu (II) complex and d) Zn (II) complex.

Table 26. Lengths and angles of coordination spheres from third coordination proposal.

Bond Lengths/ Å				
Bond	**Mn (II)**	**Co (II)**	**Cu (II)**	**Zn (II)**
M-N1	2.089	2.126	2.051	2.133
M-N2	2.090	2.141	2.053	2.150
M-N3	2.086	2.157	2.054	2.143
M-N4	2.084	2.161	2.054	2.150
M-O1	2.059	2.253	2.568	2.349
M-O2	2.057	2.271	2.573	2.357
Bond Angles/ °				
Bond	**Mn (II)**	**Co (II)**	**Cu (II)**	**Zn (II)**
N1-M-N2	94.25	91.72	88.62	91.17
N2-M-N3	88.30	89.41	89.66	88.80
N3-M-N4	89.55	86.91	91.88	89.06
N4-M-N1	88.03	91.98	89.88	90.97
O1-M-N1	93.72	93.35	86.85	93.85
O1-M-N2	90.18	86.71	92.98	86.71
O2-M-N1	90.27	92.72	88.34	92.40
O2-M-N2	93.79	92.51	91.94	93.57

Table 27 Mulliken Atomic Charges of each complex with third coordination proposal.

Mulliken Atomic Charges				
Atom	**Mn (II)**	**Co (II)**	**Cu (II)**	**Zn (II)**
N1	-0.250769	-0.263921	-0.232240	-0.257003
N2	-0.253153	-0.264303	-0.232941	-0.255486
N3	-0.255902	-0.257311	-0.237372	-0.255599
N4	-0.254740	-0.256711	-0.238490	-0.255239
O1	-0.256841	-0.232765	-0.205405	-0.230902
O2	-0.258312	-0.234585	-0.205785	-0.231624
Mn1	0.707855	-	-	-
Co1	-	0.764074	-	-
Cu1	-	-	0.507184	-
Zn1	-	-	-	0.822883

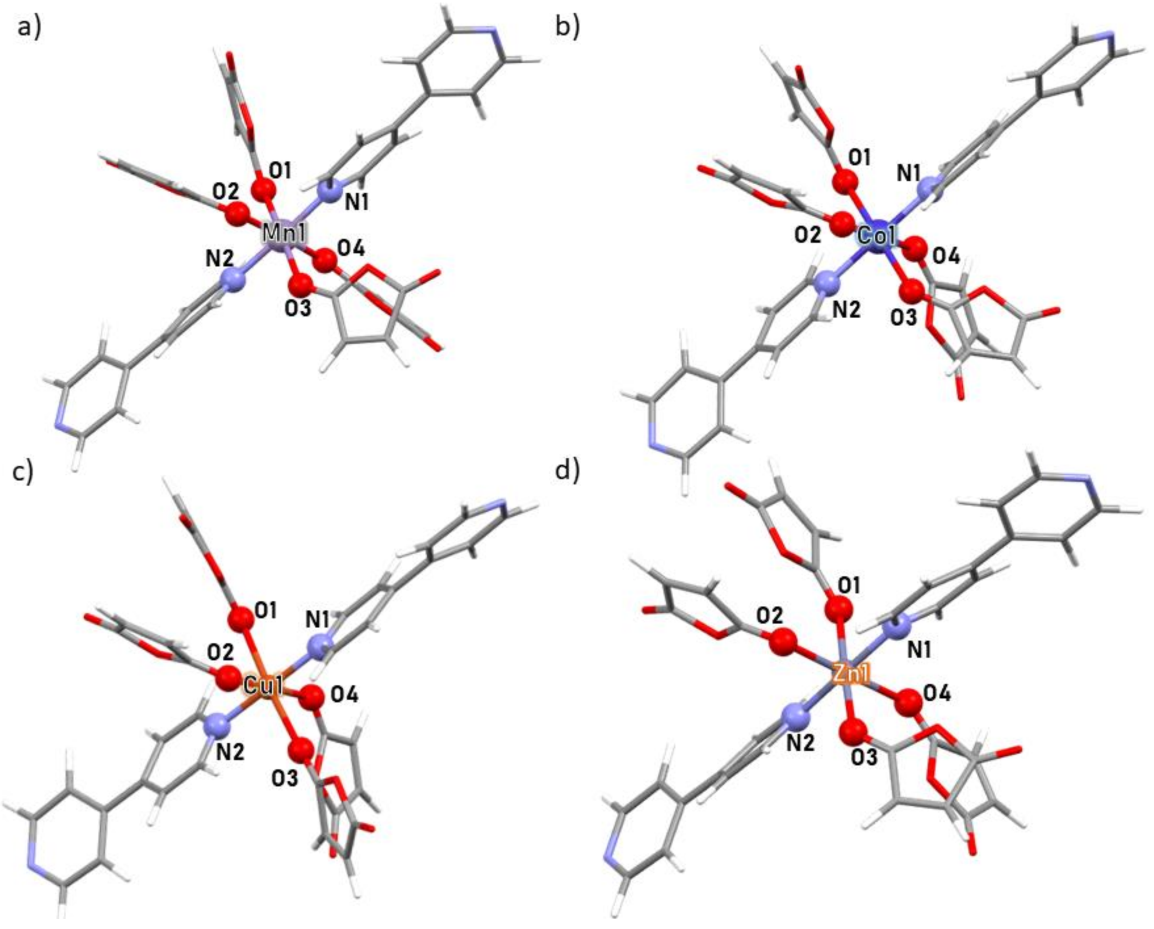

Figure 60.Fourth coordination proposal. a) Mn (II) complex, b) Co(II) complex, c) Cu(II) complex and d) Zn(II) complex.

Table 28. Lengths and angles of coordination spheres from fourth coordination proposal.

Bond Lengths/ Å				
Bond	**Mn (II)**	**Co (II)**	**Cu (II)**	**Zn (II)**
M-O1	2.036	2.199	2.336	2.331
M-O2	2.020	2.190	2.162	2.207
M-O3	2.078	2.188	2.286	2.206
M-O4	2.030	2.206	2.179	2.337
M-N1	2.048	2.079	1.993	2.037
M-N2	2.050	2.081	1.991	2.036
Bond Angles/ °				
Bond	**Mn (II)**	**Co (II)**	**Cu (II)**	**Zn (II)**
O1-M-O2	95.37	98.91	83.89	96.38
O2-M-O3	86.70	81.62	97.83	85.52
O3-M-O4	92.63	98.70	83.00	96.47
O4-M-O1	85.18	80.77	95.22	81.65
N1-M-O1	88.24	89.91	88.44	86.05
N1-M-O2	91.42	89.86	89.26	90.86
N2-M-O1	90.24	90.10	90.62	89.87
N2-M-O2	87.75	90.51	91.31	93.08

Table 29 Mulliken Atomic Charges of each complex with fourth coordination proposal.

Mulliken Atomic Charges				
Atom	**Mn (II)**	**Co (II)**	**Cu (II)**	**Zn (II)**
N1	-0.250894	-0.273705	-0.234625	-0.265241
N2	-0.252613	-0.275858	-0.236502	-0.269048
O1	-0.258161	-0.240983	-0.228165	-0.255904
O2	-0.267128	-0.241694	-0.224574	-0.254508
O3	-0.246425	-0.236096	-0.222065	-0.228364
O4	-0.253747	-0.238124	-0.217002	-0.228725
Mn1	0.761305	-	-	-
Co1	-	0.804623	-	-
Cu1	-	-	0.635810	-
Zn1	-	-	-	0.867227

The Mulliken charges in the coordination sphere atoms suggest the O-donor ligands has a better charge transfer with metals increasing the stability of complex, because the Mulliken charges also are influence by the overlapping of orbitals. Another tendency is clear in Table 23, Table 25, Table 27 and

Table 29 where Zn(II) ion has a better charged transfer followed by Co(II), Mn(II) and Cu(II).

5.10 Adsorption evaluation

One of the objectives of this work is to propose applications for the synthetized coordination polymers; the synthetized MOFs can be separated in two groups according of the isostructural phase identified, the first group is integrated by Cu-ma-bpy* and Mn-ma-bpy and the second group is formed by Co-ma-bpy and Zn-ma-bpy.

Cu-ma-bpy* and Mn-ma-bpy phases formed precipitates that have very similar molecular structures with chloride and 4,4-bipyridine bridges forming 2D framework, but although the pseudo channels are formed, those cannot be able for gas capturing or gas filtration application because are too small; it means that this MOF is formed of OD cages (Figure 61).

Amines present a great quality for adsorption and adsorption of carbon dioxide, but the bipyridines needs an activation by the addition of a hydrogen in the nitrogen atom, therefore there are not possible adsorption in the normal room environment; also, this activation has a high energetic cost, and this application is preferred for primary and secondary amines.[65]

The other possible absorption site is the metal, but this is not possible by the repulsion produced by chlorides and the electronic density of ring do not favored the adsorption too. Therefore, the carbon dioxide adsorption is completely discarded for these materials, but other applications can be tested in the future.

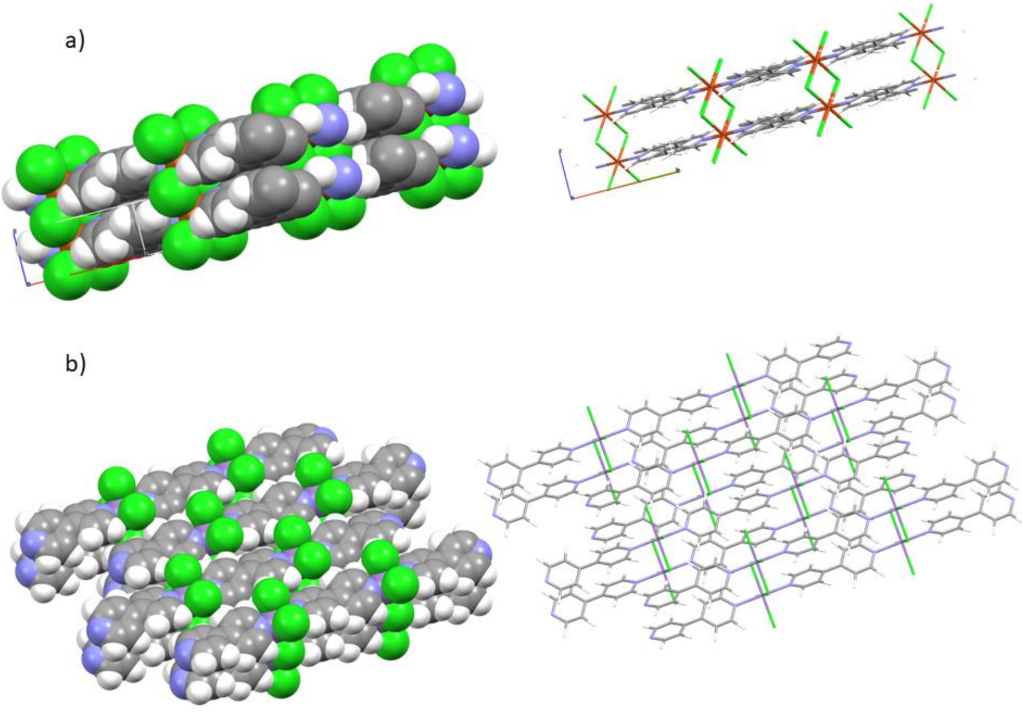

Figure 61. Space filled and, ball and sticks representation of a) Cu-ma-bpy and b) Mn-ma-bpy**

On the other hand, the minority phases identified for Co-ma-bpy and Zn-ma-bpy samples apparently do not have porosity because the water molecules and nitrates occupy the formed channels. These molecules can be removed leaving the porosity free, this process can be performed by heating the compound, although the hydrogen bonds between them increase the temperature needed. A thermal gravimetric analysis (TGA) is required to evaluate this possible pore activation. In this way, the water molecules and nitrates were removed from simulated structures and the spaces was occupied for carbon dioxide molecules to proof the possibility adsorption of this gas as shown in Figure 62. Although this is a possibility, the pore is small and only let to pass equal or shorter molecules than carbon dioxide.

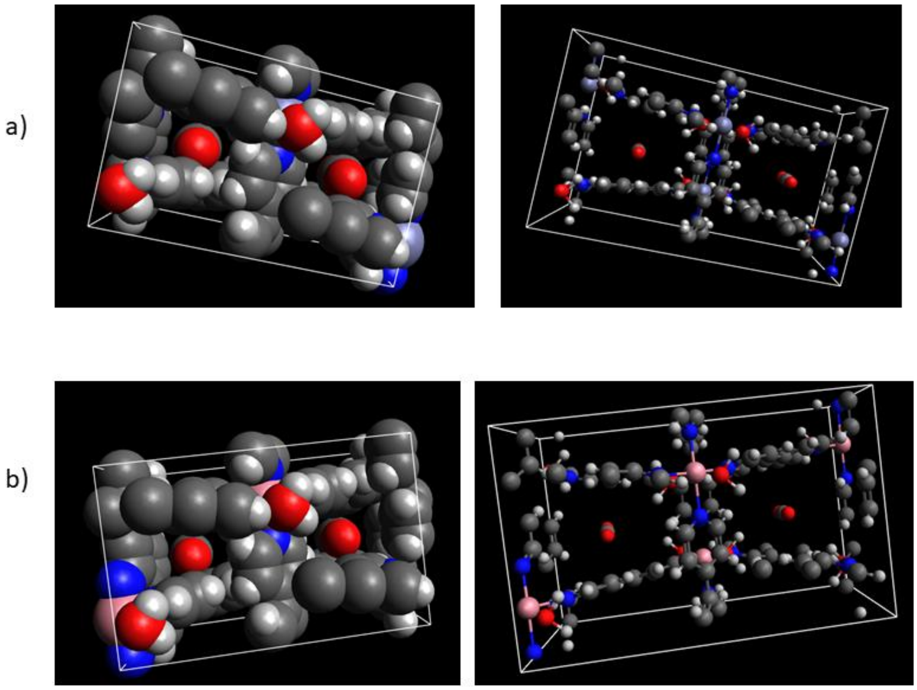

Figure 62. Representation of phases by Van der Walls spheres and ball and sticks. a) Identified phase for Co-ma-bpy, b) Identified phase for Co-ma-bpy.

In those structures again the bipyridine does not have any property for carbon dioxide adsorption, but the metal coordination sphere is more accessible that in the first group of compounds and there is enough space to get a guest molecule. Evaluating these possibilities, a geometrical optimization and relax was performed with Quantum Espresso software, but only the Co (II) compounds are simulated.

The simulation of CO_2 near to the coordination sphere of Co (II) does not converge and after days of calculus the CO_2 was repulsed to the pore, this result shows that the metallic center does not have suitable conditions for CO_2 adsorption. The adsorption of CO_2 inside the pores has two suitable possibilities (Figure 63), the more stable carbon dioxide position is the system with lower adsorption heat. The adsorption heat was calculated with the results of the optimization energies, using the following formula:

$$E_{ads} = E_{(pore+CO_2)} - [E_{pore} + E_{CO_2}]$$

The energy value of the sum of isolated pore structure and CO_2 is -3614.21178 Ry (-4744555.429 kJ/mol); while to total energy of the systems in Figure 63 is -4744672.798 kJ/mol for b) and -4744696.063 kJ/mol for a); therefore, the configuration with lower adsorption heat is b). The adsorption heat for b) is -140.6339533 kJ/mol , while for a) is -117.3684008 kJ/mol; it means the adsorption of CO_2 is energetically favored near to the wall of the molecular framework than in the middle of the pore.

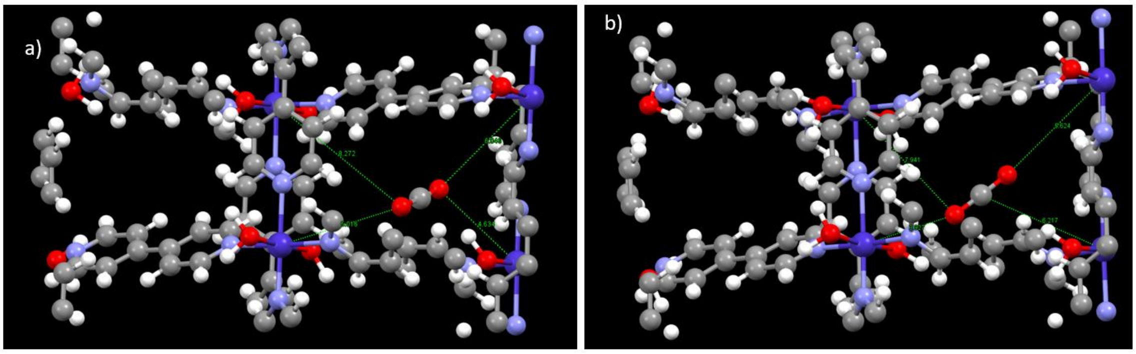

Figure 63. Suitable position of carbon dioxide molecules inside the Co(II) MOF.

5.11 Post-synthetic modification proposal by Diels Alder.

The samples Mn-ma-bpy, Co-ma-bpy and Zn-ma-bpy were not completely elucidated and according with their FTIR spectra the maleic acid is coordinated with each metal, those phase with maleic acid can be modified introducing a post-synthetic modification by cycloaddition. Maleic acid can achieve a cyclization by Diels Alder addition mechanism (Figure 64), in this case 1,3-diene can be cycloadded to maleic acid producing a very similar molecule of phthalic acid.

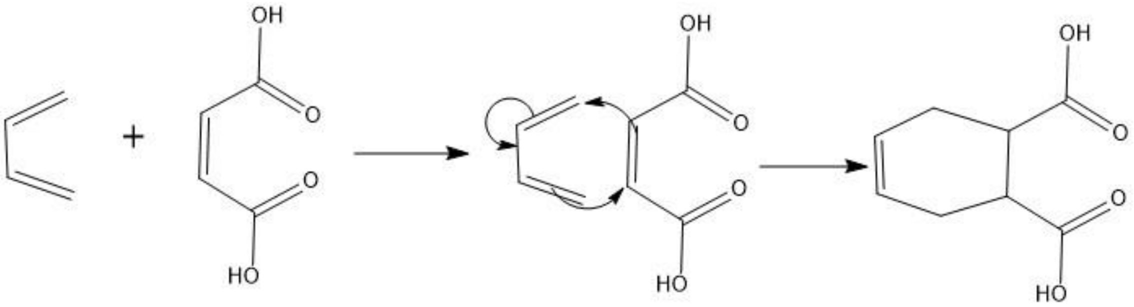

Figure 64. Diels Alder cycloaddition of 1,3-diene to maleic acid.

Maleic acid is the dienophile of this cycloaddition and the main requirement of this reaction is the overlapping of Highest Occupied Molecular Orbital (HOMO) of 1,3-diene and the Lowest Unoccupied Molecular Orbital of conjugation in maleic acid; to proof the possibility of this reaction the reagents was optimized in Orca and the molecular orbital were simulated to find the overlapping of orbital. The reagents were ubicated in different position until achieve the overlapping as is shown in Figure 65.

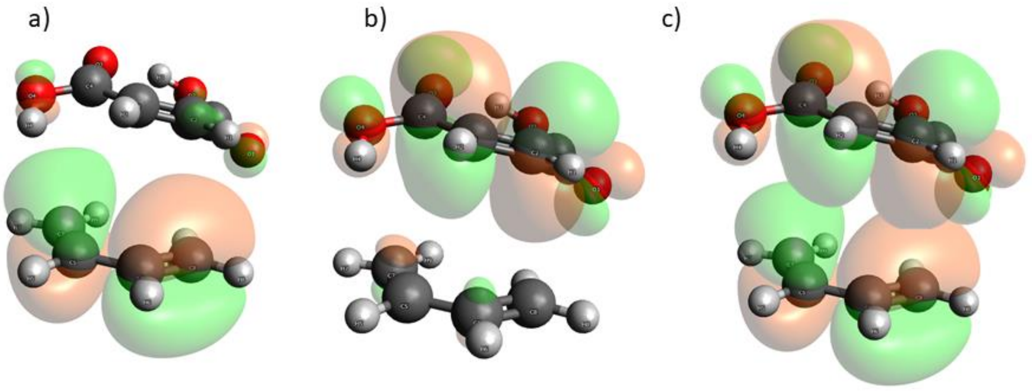

Figure 65. a) HOMO of 1,3-diene, b) LUMO of maleic acid, c) Overlapping of a) and b) allowing the cycloaddition.

This proposal has the main objective to evaluate if this post-synthetic modification results in a similar MOF reported by Patricia Mendoza in 2016[35], where four phthalic acids and two 4,4-bipyridines are coordinated with a cobalt metallic center as is shown in Figure 10.

5.12 Photo-response modelling of referenced material.

The photo-response was simulated in the referenced material synthetized by Quintero and Avila[34]; the structural change in this MOF could be produced by the dimerization of maleic anhydride, this reversible reaction is carried out by a 2+2 cycloaddition, the photo activation of those kind of reaction is reported widely using UV radiation, the peak of radiation adsorption occurs at 250 nm.[66,67] The photodimerization of maleic anhydride form the cyclobutane tetracarboxylic dianhydride (CBTA) and this compound has a strong geometrical restriction by the cyclobutane; this change is shown in Figure 66.

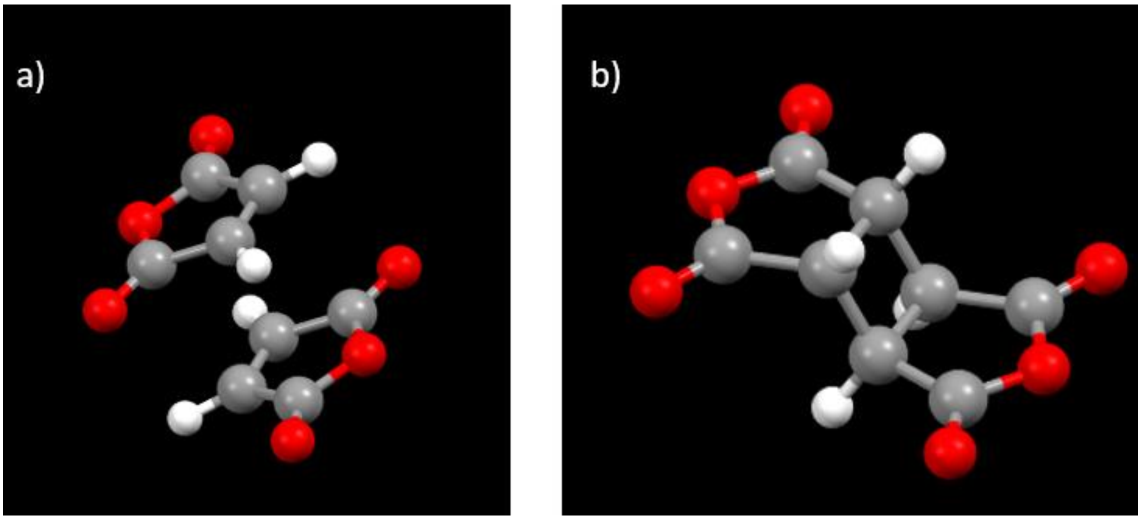

Figure 66. a) maleic acid in the relative positions according to the MOF reported by Quintero and Avila. b) CBTA formed as result of the photodimerization.

The photodimerization of maleic anhydride was simulated by geometric optimization in Orca to understand how the coordination spheres are affected. The results show a drastic change in the coordination environment losing the coordination on one oxygen by each CBTA molecule and the rotation of the 4,4-bipyridines (Figure 67). This result infers the possible structural change of the topology in the material and increase the possibility of an adsorption properties because the metal is more accessible, but also this photo-activation could be destroyed the framework if the oxygen bond is not enough to stabilize the structure.

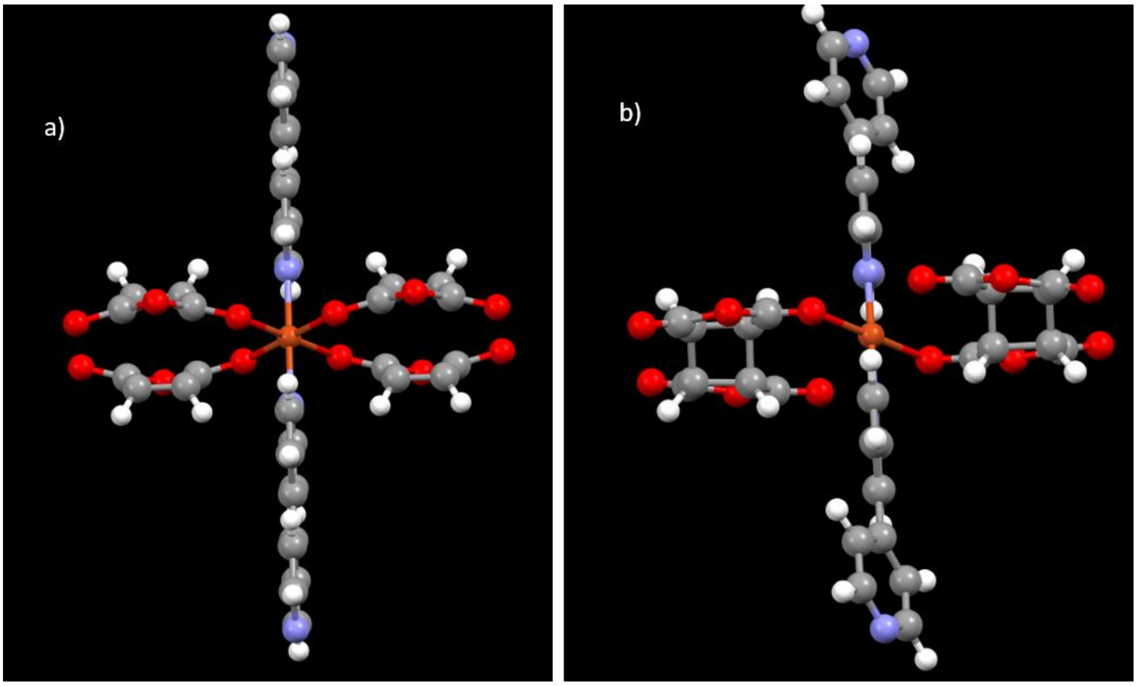

Figure 67. a) coordination sphere before photodimerization. b) coordination sphere after photodimerization

CHAPTER VI: Conclusion and future work

Octahedral coordination polymers were synthetized by hydrothermal method, the ligands used for this purpose were maleic acid and 4,4-bipyrideine. The Cu-ma-bpy* and Mn-ma-bpy form a coordination polymer but those cannot be considered as MOF because they do not have a real porosity freed for gas adsorption application. Both phases confirm the low lability of chlorides and its capacity to remain in the coordination sphere, even building chloride bridges; therefore, the counter ion of metallic salt influence the possible coordination of metal in a framework; and it is better to use nitrate salts than chloride salt to prevent distortions in the desired coordination.

Co-ma-bpy and Zn-ma-bpy have a minority phase as regard to 2D MOF structure, those structures have enough pore size to allow a possible application in adsorption of small molecules such as carbon dioxide. According with Co-ma-bpy adsorption simulation there two suitable site for carbon dioxide adsorption, but the preferred site for carbon dioxide in near to the walls than in the middle of the pore; also these simulations infers that a direct interaction between Co (II) and CO_2 is not favored. This application depends on Nitrogen adsorption isotherm to evaluate the porosity and TGA studies to evaluate the activation of pores, removing water molecules, and thermal stability of the compound. Also, this phase needs a more intense characterization to elucidate all phases present in the third stage of synthesis.

Hexamethylenetetramine form coordination compound with high hydroscopic behavior, but there is no proof of coordination polymers; although having four possible nitrogen donors, its compressed geometry and its steric hindrance do not let to synthetize MOFs and it is better use 4,4-biyridine for MOF synthesis.

FT-IR and UV-Vis spectroscopy are useful to suggest the structure of synthetized compounds, but X-Ray Diffractometry is the main characterization technique to elucidate crystalline compounds and identified phases presented in the samples.

Thinking in the future the modification of synthetized MOFs is needed to improve the properties of the materials, so the cyclization of maleic acid by Diels Alder addition could be modified the structure of coordination polymer, because this cycled molecule is very similar to phthalic acid used for very similar coordination compounds reported by Mendoza in 2016 [35].

Also, considering the material synthetized of Quinteros and Avila[34], a photo-response of this MOF is possible by the dimerization of maleic anhydride; the computational simulation of this reaction gave two possibilities, the first one is a reversible structural change with more accessible Co (II) ions, but the possibility of very instable material is present too.

Computational calculus and simulations are very useful to understand some phenomena; Quantum Expresso, Orca are very useful to optimize structures and simulate properties such as the ability of coordination, the stability of materials, spectroscopic properties, and molecular dynamics; also, Xcrysden, Mercury and Avogadro are great graphical user interfaces that let interpretate the calculations results.

MOF are very promising compound with applications in any field of industry and their ability to introduce modifications in the framework and even introduce active principles let design compounds needed to develop new electronic devices, better hydrogen batteries, modern systems to caught water molecules or separate gases and other.

References

1. Van Der Voort, P., Leus, K. & De Canck, E. *Introduction to Porous Materials*. (Jhon Wiley & Sons Ltd, 2019).

2. Yaghi, O. M., Kalmutzki, M. J. & Diercks, C. S. *Introduction to reticular chemistry : metal-organic frameworks and covalent organic frameworks*. (Wiley-VCH, 2019).

3. Cordova, K. E. & Yaghi, O. M. The 'folklore' and reality of reticular chemistry. *Mater. Chem. Front.* **1**, 1304–1309 (2017).

4. Zhou, H. C., Long, J. R. & Yaghi, O. M. Introduction to metal-organic frameworks. *Chemical Reviews* vol. 112 673–674 (2012).

5. Ribas Gispert, J. *Coordination chemistry*. (Wiley-VCH, 2008).

6. Fang, Q., Sculley, J., Zhou, H. C. J. & Zhu, G. Porous Metal-Organic Frameworks. in *Comprehensive Nanoscience and Technology* vols 1–5 1–20 (Elsevier Inc., 2011).

7. Li, G., Xia, L., Dong, J., Chen, Y. & Li, Y. Metal-organic frameworks. in *Solid-Phase Extraction* 285–309 (Elsevier, 2019). doi:10.1016/B978-0-12-816906-3.00010-8.

8. Cai, P. *et al.* Metal-organic frameworks: New functional materials and applications. in *Comprehensive Nanoscience and Nanotechnology* vols 1–5 35–54 (Elsevier, 2019).

9. Qian, B., Chang, Z. & Bu, X. H. Functionalized Dynamic Metal–Organic Frameworks as Smart Switches for Sensing and Adsorption Applications. *Topics in Current Chemistry* vol. 378 (2020).

10. Walton, I. M. *et al.* Photo-responsive MOFs: Light-induced switching of porous single crystals containing a photochromic diarylethene. *Chem. Commun.* **49**, 8012–8014 (2013).

11. Gates, T. & Jeffrey, H. Computational Materials: Modeling and Simulation of Nanostructured Materials and Systems. *Natl. Aeronaut. Sp. Adm.* (2003).

12. Neese, F., Wennmohs, F., Becker, U. & Riplinger, C. The ORCA quantum chemistry program package. *J. Chem. Phys.* **152**, 224108 (2020).

13. QUANTUMESPRESSO - QUANTUMESPRESSO. https://www.quantum-espresso.org/.

14. Liu, P. & Chen, G. *Porous Materials*. (Elsevier, 2014).

15. Tüysüz, H. & Schüth, F. Ordered Mesoporous Materials as Catalysts. in *Advances in Catalysis* vol. 55 127–239 (Academic Press Inc., 2012).

16. Lee, Y. R., Kim, J. & Ahn, W. S. Synthesis of metal-organic frameworks: A mini review. *Korean Journal of Chemical Engineering* vol. 30 1667–1680 (2013).

17. Mashhadzadeh, A. H. *et al.* Metal–Organic Framework (MOF) through the Lens of Molecular Dynamics Simulation: Current Status and Future Perspective. *J. Compos. Sci.* **4**, 75 (2020).

18. Wang, K. B. *et al.* Metal-organic frameworks with different spatial dimensions for supercapacitors. *New Journal of Chemistry* vol. 44 3147–3167 (2020).

19. Miao, Y. R. & Suslick, K. S. Mechanochemical Reactions of Metal-Organic Frameworks. in *Advances in Inorganic Chemistry* vol. 71 403–434 (Academic Press Inc., 2018).

20. Jpn, B., Paik Suh, M. & Author, C. *Metal-Organic Frameworks and Porous Coordination Polymers: Properties and Applications Metal-Organic Frameworks and Porous Coordination*. *Soc. Coord. Chem* vol. 65 (2015).

21. James, S. L. Metal-organic frameworks. *Chem. Soc. Rev.* **32**, 276–288 (2003).

22. Zafar, F. & Sharmin, E. *Metal-Organic Frameworks*. (ExLi4EvA, 2016).

23. Lukehart, C. & MacGillivray, L. *Metal-Organic Framework Materials*. (Wiley, 2014).

24. Eddaoudi, M. *et al.* Modular chemistry: Secondary building units as a basis for the design of highly porous and robust metal-organic carboxylate frameworks. *Acc. Chem. Res.* **34**, 319–330 (2001).

25. Tranchemontagne, D. J., Tranchemontagne, J. L., O'keeffe, M. & Yaghi, O. M. Secondary building units, nets and bonding in the chemistry of metal–organic frameworks. *Chem. Soc. Rev.* **38**, 1257–1283 (2009).

26. *Metal Organic Frameworks*. (MDPI, 2020).

27. Smith, M. B. & March, J. Mechanisms and Methods of Determining Them. in *March's Advanced Organic Chemistry* 296–327 (John Wiley & Sons, Inc., 2007). doi:10.1002/9780470084960.ch6.

28. Manouras, T. & Vamvakaki, M. Field responsive materials: Photo-, electro-, magnetic- and ultrasound-sensitive polymers. *Polymer Chemistry* vol. 8 74–96 (2017).

29. Mukhopadhyay, R. D., Praveen, V. K. & Ajayaghosh, A. Photoresponsive metal-organic materials: Exploiting the azobenzene switch. *Mater. Horizons* **1**, 572–576 (2014).

30. Patel, D. G. *et al.* Photoresponsive porous materials: The design and synthesis of

photochromic diarylethene-based linkers and a metal-organic framework. *Chem. Commun.* **50**, 2653–2656 (2014).

31. Patel, D. G. *et al.* Photoresponsive porous materials: The design and synthesis of photochromic diarylethene-based linkers and a metal-organic framework. *Chem. Commun.* **50**, 2653–2656 (2014).

32. Castellanos, S., Kapteijn, F. & Gascon, J. Photoswitchable metal organic frameworks: Turn on the lights and close the windows. *CrystEngComm* vol. 18 4006–4012 (2016).

33. Rice, A. M. *et al.* Photophysics Modulation in Photoswitchable Metal-Organic Frameworks. *Chemical Reviews* vol. 120 8790–8813 (2020).

34. Quintero, M. & Avila, E. *Personal Communications*. (2011).

35. Mendoza, P. Diseño, síntesis y caracterización de polímeros de coordinación empleando como unidades de conexión anhídridos orgánicos mono- y bi-funcionalizados como potenciales intercambiadores iónicos. (UNIVERSIDAD DE LOS ANDES, 2016).

36. Pavia, D., Lampman, G., Kriz, G. & Vyvyan, J. *Introduction to Spectroscopy* . (2013).

37. Larkin, P. *Infrared and Raman Spectroscopy*. (Elsevier, 2018). doi:10.1016/C2015-0-00806-1.

38. Ramer, G. & Lendl, B. Attenuated Total Reflection Fourier Transform Infrared Spectroscopy. in *Encyclopedia of Analytical Chemistry* (John Wiley & Sons, Ltd, 2013). doi:10.1002/9780470027318.a9287.

39. Stuart, B. *Infrared Spectroscopy: Fundamentals and Applications.* (Wiley, 2004).

40. Gauglitz, G. & Moore, D. *Handbook of Spectroscopy*. (Wiley-VCH Verlag, 2014).

41. Huheey, J. E., Keiter, E. A., Keiter, R. L. & Aguilar Ortega, M. T. *Química inorgánica : principios de estructura y reactividad*. (Oxford University Press, 1997).

42. Tabisz, Ł., Tukibayeva, A., Pankiewicz, R., Dobielska, M. & Leska, B. Disiloxanes and Functionalized Silica Gels: One Route, Two Complementary Outcomes—Guanidinium and Pyridinium Ion-Exchangers. *PLoS One* **10**, e0145680 (2015).

43. Garcia, J., Bausa, L. E. & Jaque, D. *An Introduction to the Optical Spectroscopy of Inorganic Solids*. (Jhon Wiley & Sons Ltd, 2005).

44. Cullity, B. D. & S.R., S. *Elements of X-Ray Diffraction*. (PEARSON, 2014).

45. X-Rays | MyScope. https://myscope.training/legacy/xrd/background/concepts/xrays/.

46. Mohanty, S., Das, B. & Dhara, S. Poly(maleic acid) - A novel dispersant for aqueous alumina slurry. *J. Asian Ceram. Soc.* **1**, 184–190 (2013).

47. Max, J. J. & Chapados, C. Infrared spectroscopy of aqueous carboxylic acids: Malic acid. *J. Phys. Chem. A* **106**, 6452–6461 (2002).

48. Mirhosseini-Eshkevari, B., Ghasemzadeh, M. A., Esnaashari, M. & Ganjali, S. T. Hexamethylenetetramine-based ionic liquid/MIL-101(Cr) metal-organic framework composite: a novel and versatile tool for the preparation of pyrido[2,3-d:5,6-d′]dipyrimidines. *RSC Adv.* **11**, 364–373 (2020).

49. Xu, J. *et al.* Preparation and characterization of fast-curing powder epoxy adhesive at middle temperature. *R. Soc. Open Sci.* **5**, (2018).

50. Tamer, Ö. A unique manganese (II) complex of 4-methoxy-pyridine-2-carboxylate: Synthesis, crystal structure, FT-IR and UV–Vis spectra and DFT calculations. *J. Mol. Struct.* **1144**, 370–378 (2017).

51. Chang, R. & Goldsby, K. *Chemistry*. (McGraw-Hill Education, 2012).

52. Köse, D. A., Necefoglu, H. & Icbudak, H. Synthesis and characterization of N,N-diethylnicotinamide-acetylsalicylato complexes of Co(II), Ni(II), Cu(II), and Zn(II). *J. Coord. Chem.* **61**, 3508–3515 (2008).

53. Hargreaves, M. K. & Stevinson, E. A. The infra-red spectra of fumaramic and maleamic acids and their sodium salts. *Spectrochim. Acta* **21**, 1681–1689 (1965).

54. Nguyen, T. T., Le, T. T., Phan, P. T. & Nguyen, N. H. Preparation, Characterization, and Application of Novel Ferric Oxide-Amine Material for Removal of Nitrate and Phosphate in Water. *J. Chem.* **2020**, 1–12 (2020).

55. Köse, D. A. & Necefoğlu, H. Synthesis and characterization of bis(nicotinamide) m-hydroxybenzoate complexes of Co(II), Ni(II), Cu(II) and Zn(II). *J. Therm. Anal. Calorim.* **93**, 509–514 (2008).

56. Vraneš, M., Gadžurić, S. B., Zsigrai, I. J. & Dožić, S. Absorption spectra of cobalt(II) chloride and nitrate complexes in aqueous calcium nitrate-ammonium nitrate melts: The influence of solvent composition. *J. Mol. Liq.* **152**, 34–38 (2010).

57. Mishinkin, V. Y., Grabovsky, S. A., Kabal'Nova, N. N. & Murinov, Y. I. Complex formation between 5-aminoorotic acid and copper(II) ions in dimethylsulfoxide solution. *Russ. J. Gen. Chem.* **85**, 1686–1691 (2015).

58. Patel, K. S., Patel, J. C., Dholariya, H. R., Patel, V. K. & Patel, K. D. Synthesis of

Cu(II), Ni(II), Co(II), and Mn(II) Complexes with Ciprofloxacin and Their Evaluation of Antimicrobial, Antioxidant and Anti-Tubercular Activity. *Open J. Met.* **2**, 49–59 (2012).

59. Crabtree, R. *THE ORGANOMETALLIC CHEMISTRY OF THE TRANSITION METALS*. (John Wiley & Sons, Inc., 2014).

60. Chaudhary, R. G. *et al.* Synthesis and characterization of metal coordination polymers with fumaroyl bis (paramethoxyphenylcarbamide) by using FTIR, XRD, SEM and TG techniques . *J. Chinese Adv. Mater. Soc.* **3**, 177–187 (2015).

61. Bedowr, N. S., Yahya, R. B. & Farhan, N. Structural characterization of copper (II) tetradecanoate with 2,2′-bipyridine and 4,4′-bipyridine to study magnetic properties. *J. Saudi Chem. Soc.* **22**, 255–260 (2018).

62. Tamer, Ö. A unique manganese (II) complex of 4-methoxy-pyridine-2-carboxylate: Synthesis, crystal structure, FT-IR and UV–Vis spectra and DFT calculations. *J. Mol. Struct.* **1144**, 370–378 (2017).

63. Hu, C., Li, Q. & Englert, U. Structural trends in one and two dimensional coordination polymers of cadmium(II) with halide bridges and pyridine-type ligands. *CrystEngComm* **5**, 519–529 (2003).

64. Czakis-Sulikowska, D. & Czylkowska, A. Complexes of Mn(II), Co(II), Ni(II) and Cu(II) with 4,4′-bipyridine and dichloroacetates. Synthesis, thermal and other properties. *J. Therm. Anal. Calorim.* **71**, 395–405 (2003).

65. Lim, C. H., Holder, A. M. & Musgrave, C. B. Mechanism of homogeneous reduction of CO2 by pyridine: Proton relay in aqueous solvent and aromatic stabilization. *J. Am. Chem. Soc.* **135**, 142–154 (2013).

66. Zhang, Z. Photodimerization of Maleic Anhydride. *J. Chem. Educ.* **75**, 1515 (1998).

67. Horie, T. *et al.* Photodimerization of maleic anhydride in a microreactor without clogging. *Org. Process Res. Dev.* **14**, 405–410 (2010).

Appendix I: COMPUTATIONAL INPUTS

Orca Input examples

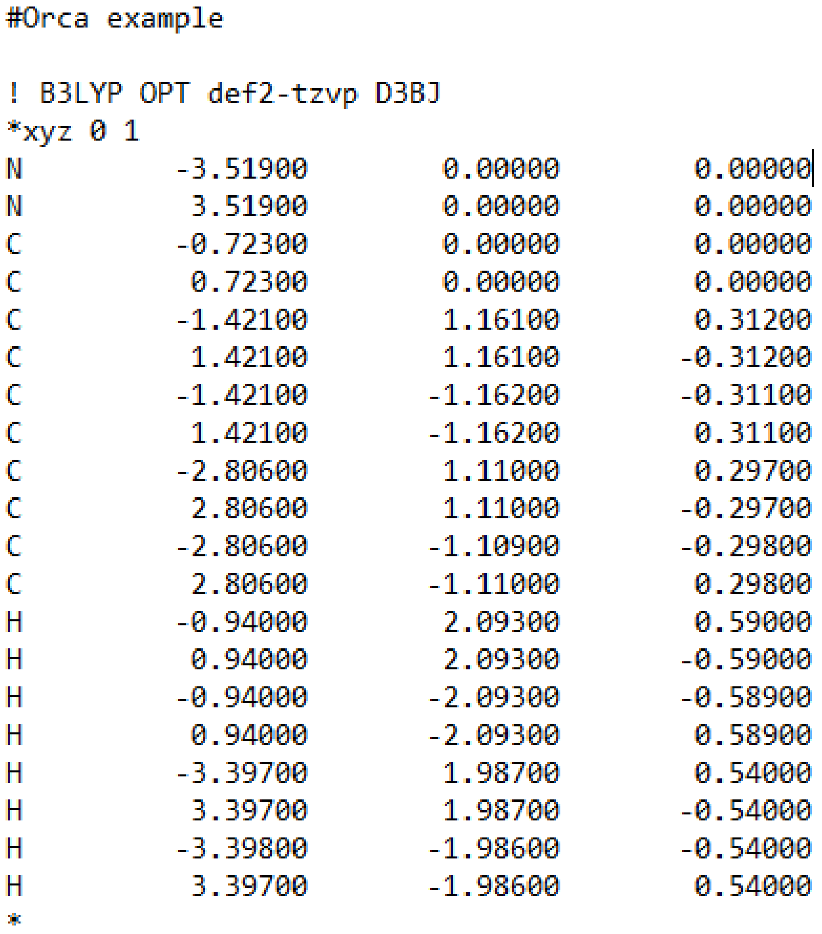

```
#Orca example

! B3LYP OPT def2-tzvp D3BJ
*xyz 0 1
N         -3.51900        0.00000        0.00000
N          3.51900        0.00000        0.00000
C         -0.72300        0.00000        0.00000
C          0.72300        0.00000        0.00000
C         -1.42100        1.16100        0.31200
C          1.42100        1.16100       -0.31200
C         -1.42100       -1.16200       -0.31100
C          1.42100       -1.16200        0.31100
C         -2.80600        1.11000        0.29700
C          2.80600        1.11000       -0.29700
C         -2.80600       -1.10900       -0.29800
C          2.80600       -1.11000        0.29800
H         -0.94000        2.09300        0.59000
H          0.94000        2.09300       -0.59000
H         -0.94000       -2.09300       -0.58900
H          0.94000       -2.09300        0.58900
H         -3.39700        1.98700        0.54000
H          3.39700        1.98700       -0.54000
H         -3.39800       -1.98600       -0.54000
H          3.39700       -1.98600        0.54000
*
```

Figure 68. Orca Input file for 4,4-bipyridine geometry optimization

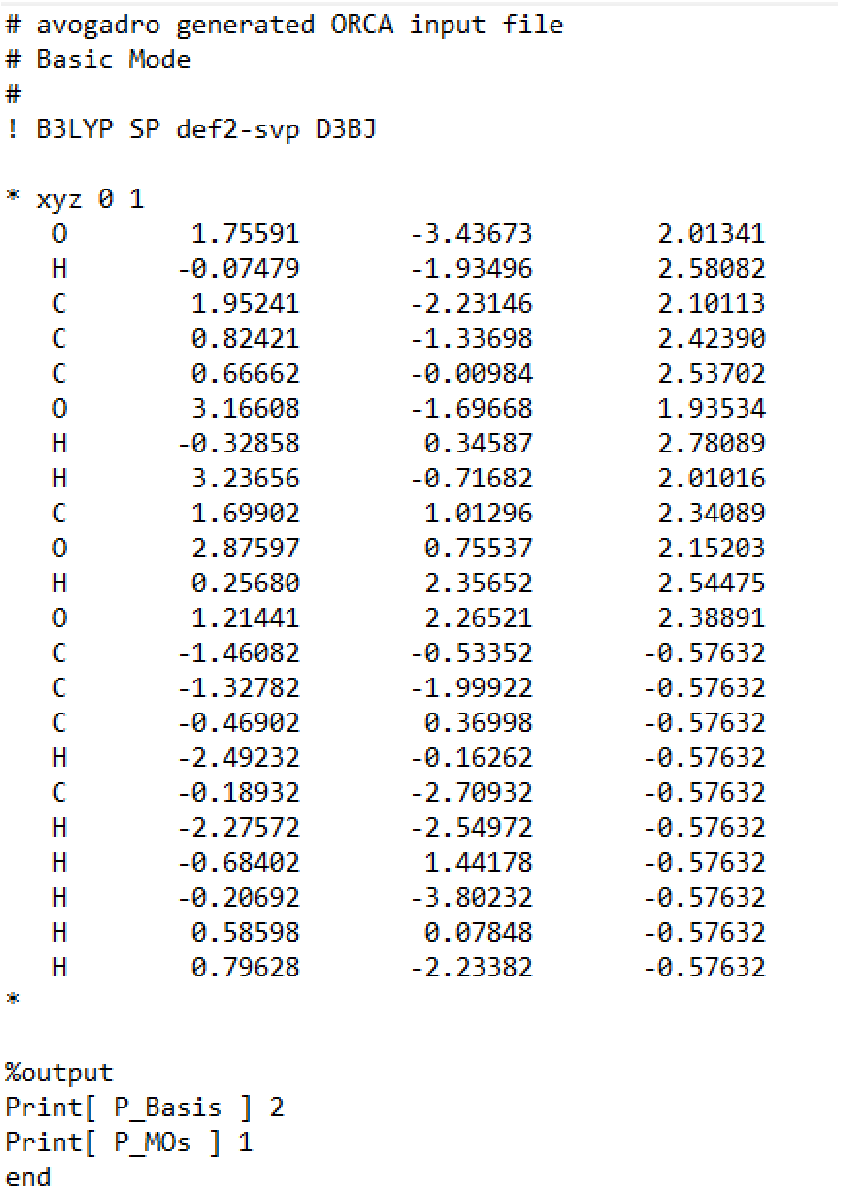

```
# avogadro generated ORCA input file
# Basic Mode
#
! B3LYP SP def2-svp D3BJ

* xyz 0 1
   O        1.75591      -3.43673       2.01341
   H       -0.07479      -1.93496       2.58082
   C        1.95241      -2.23146       2.10113
   C        0.82421      -1.33698       2.42390
   C        0.66662      -0.00984       2.53702
   O        3.16608      -1.69668       1.93534
   H       -0.32858       0.34587       2.78089
   H        3.23656      -0.71682       2.01016
   C        1.69902       1.01296       2.34089
   O        2.87597       0.75537       2.15203
   H        0.25680       2.35652       2.54475
   O        1.21441       2.26521       2.38891
   C       -1.46082      -0.53352      -0.57632
   C       -1.32782      -1.99922      -0.57632
   C       -0.46902       0.36998      -0.57632
   H       -2.49232      -0.16262      -0.57632
   C       -0.18932      -2.70932      -0.57632
   H       -2.27572      -2.54972      -0.57632
   H       -0.68402       1.44178      -0.57632
   H       -0.20692      -3.80232      -0.57632
   H        0.58598       0.07848      -0.57632
   H        0.79628      -2.23382      -0.57632
*

%output
Print[ P_Basis ] 2
Print[ P_MOs ] 1
end
```

Figure 69. Input for orbitals calculation in the Diels Alder reaction between maleic acid and 1,3-diene

Quantum Espresso Input examples

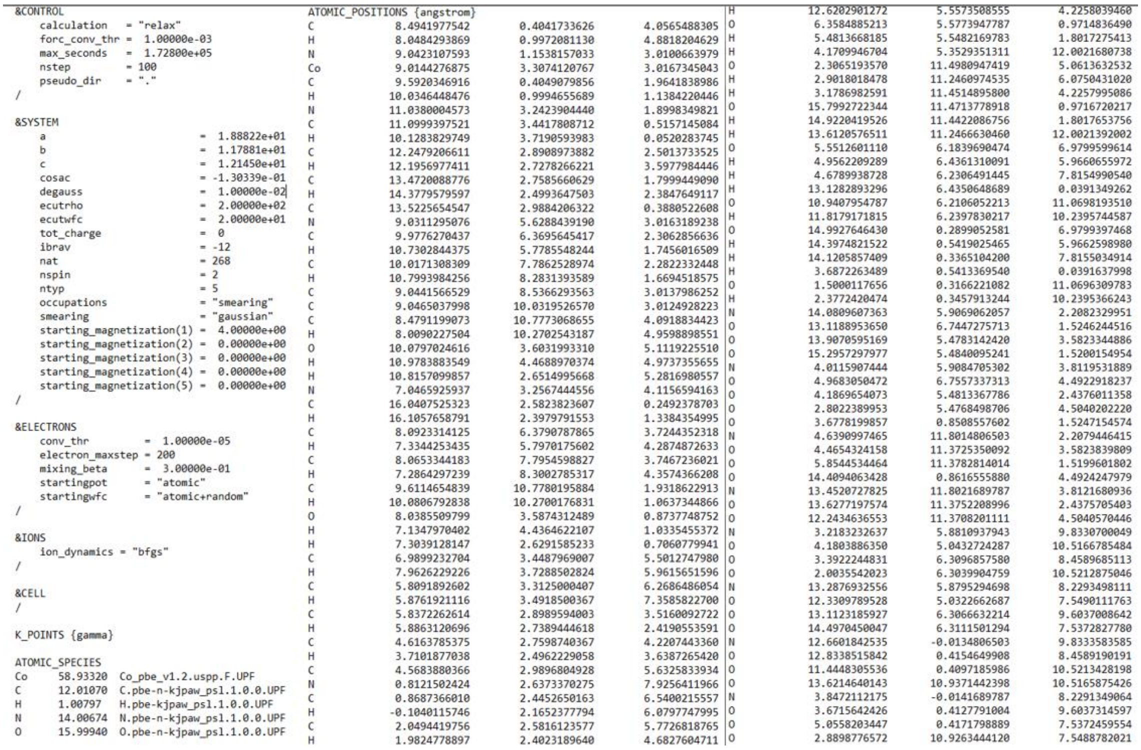

```
&CONTROL
    calculation   = "relax"
    forc_conv_thr =  1.00000e-03
    max_seconds   =  1.72800e+05
    nstep         = 100
    pseudo_dir    = "."
/

&SYSTEM
    a                         =  1.88822e+01
    b                         =  1.17881e+01
    c                         =  1.21450e+01
    cosac                     = -1.30339e-01
    degauss                   =  1.00000e-02
    ecutrho                   =  2.00000e+02
    ecutwfc                   =  2.00000e+01
    tot_charge                =  0
    ibrav                     = -12
    nat                       = 268
    nspin                     = 2
    ntyp                      = 5
    occupations               = "smearing"
    smearing                  = "gaussian"
    starting_magnetization(1) =  4.00000e+00
    starting_magnetization(2) =  0.00000e+00
    starting_magnetization(3) =  0.00000e+00
    starting_magnetization(4) =  0.00000e+00
    starting_magnetization(5) =  0.00000e+00
/

&ELECTRONS
    conv_thr         =  1.00000e-05
    electron_maxstep = 200
    mixing_beta      =  3.00000e-01
    startingpot      = "atomic"
    startingwfc      = "atomic+random"
/

&IONS
    ion_dynamics = "bfgs"
/

&CELL
/

K_POINTS {gamma}

ATOMIC_SPECIES
Co     58.93320  Co_pbe_v1.2.uspp.F.UPF
C      12.01070  C.pbe-n-kjpaw_psl.1.0.0.UPF
H      1.00797   H.pbe-kjpaw_psl.1.0.0.UPF
N      14.00674  N.pbe-n-kjpaw_psl.1.0.0.UPF
O      15.99940  O.pbe-n-kjpaw_psl.1.0.0.UPF
```

```
ATOMIC_POSITIONS {angstrom}
C            8.4941977542       0.4041733626       4.0565488305
H            8.0484293869       0.9972081130       4.8818204629
N            9.0423107593       1.1538157033       3.0100663979
Co           9.0144276875       3.3074120767       3.0167345043
C            9.5920346916       0.4049079856       1.9641838986
H           10.0346448476       0.9994655689       1.1384220446
N           11.0380004573       3.2423904440       1.8998349821
C           11.0999397521       3.4417808712       0.5157145084
H           10.1283829749       3.7190593983       0.0520283745
C           12.2479206611       2.8908973882       2.5013733525
H           12.1956977411       2.7278266221       3.5977984446
C           13.4720088776       2.7585660629       1.7999449090
H           14.3779579597       2.4993647503       2.3847649117
C           13.5225654547       2.9884206322       0.3880522608
N            9.0311295076       5.6288439190       3.0163189238
C            9.9776270437       6.3695645417       2.3062856636
H           10.7302844375       5.7785548244       1.7456016509
C           10.0171308309       7.7862528974       2.2822332448
H           10.7993984256       8.2831393589       1.6694518575
C            9.0441566529       8.5366293563       3.0137986252
C            9.0465037998      10.0319526570       3.0124928223
C            8.4791199073      10.7773068655       4.0918834423
H            8.0090227504      10.2702543187       4.9598898551
O           10.0797024616       3.6031993310       5.1119225510
H           10.9783883549       4.4688970374       4.9737355655
H           10.8157099857       2.6514995668       5.2816980557
N            7.0465925937       3.2567444556       4.1156594163
C           16.0407525323       2.5823823607       0.2492378703
H           16.1057658791       2.3979791553       1.3384354995
C            8.0923314125       6.3790787865       3.7244352318
H            7.3344253435       5.7970175602       4.2874872633
C            8.0653344183       7.7954598827       3.7467236021
H            7.2864297239       8.3002785317       4.3574366208
C            9.6114654839      10.7780195884       1.9318622913
H           10.0806792838      10.2700176831       1.0637344866
O            8.0385509799       3.5874312489       0.8737748752
H            7.1347970402       4.4364622107       1.0335455372
H            7.3039128147       2.6291585233       0.7060779941
C            6.9899232704       3.4487969007       5.5012747980
H            7.9626229226       3.7288502824       5.9615651596
C            5.8091892602       3.3125000407       6.2686486054
H            5.8761921116       3.4918500367       7.3585822700
C            5.8372262614       2.8989594003       3.5160092722
H            5.8863120696       2.7389444618       2.4190553591
C            4.6163785375       2.7598740367       4.2207443360
H            3.7101877038       2.4962229058       3.6387265420
C            4.5683880366       2.9896804928       5.6325833934
N            0.8121502424       2.6373370275       7.9256411966
C            0.8687366010       2.4452650163       6.5400215557
H           -0.1040115746       2.1652377794       6.0797747995
C            2.0494419756       2.5816123577       5.7726818765
H            1.9824778897       2.4023189640       4.6827604711
```

```
H           12.6202901272       5.5573508555       4.2258039460
O            6.3584885213       5.5773947787       0.9714836490
H            5.4813668185       5.5482169783       1.8017275413
H            4.1709946704       5.3529351311      12.0021680738
O            2.3065193570      11.4980947419       5.0613632532
H            2.9018018478      11.2460974535       6.0750431020
H            3.1786982591      11.4514895800       4.2257995086
O           15.7992722344      11.4713778918       0.9716720217
H           14.9220419526      11.4422086756       1.8017653756
H           13.6120576511      11.2466630460      12.0021392002
O            5.5512601110       6.1839690474       6.9799599614
H            4.9562209289       6.4361310091       5.9660655972
H            4.6789938728       6.2306491445       7.8154990540
H           13.1282893296       6.4350648689       0.0391349262
O           10.9407954787       6.2106052213      11.0698193510
H           11.8179171815       6.2397830217      10.2395744587
O           14.9927646430       0.2899052581       6.9799397468
H           14.3974821522       0.5419025465       5.9662598980
H           14.1205857409       0.3365104200       7.8155034914
H            3.6872263489       0.5413369540       0.0391637998
O            1.5000117656       0.3166221082      11.0696309783
H            2.3772420474       0.3457913244      10.2395366243
N           14.0809607363       5.9069062057       2.2082329951
O           13.1188953650       6.7447275713       1.5246244516
O           13.9070595169       5.4783142420       3.5823344886
O           15.2957297977       5.4840095241       1.5200154954
N            4.0115907444       5.9084705302       3.8119531889
O            4.9683050472       6.7557337313       4.4922918237
O            4.1869654073       5.4813367786       2.4376011358
O            2.8022389953       5.4768498706       4.5040202220
O            3.6778199857       0.8508557602       1.5247154574
N            4.6390997465      11.8014806503       2.2079446415
O            4.4654324158      11.3725350092       3.5823839809
O            5.8544534464      11.3782814014       1.5199601802
O           14.4094063428       0.8616555880       4.4924247979
N           13.4520727825      11.8021689787       3.8121680936
O           13.6277197574      11.3752208996       2.4375705403
O           12.2434636553      11.3708201111       4.5040570446
N            3.2183232637       5.8810937943       9.8330700049
O            4.1803886350       5.0432724287      10.5166785484
O            3.3922244831       6.3096857580       8.4589685113
O            2.0035542023       6.3039904759      10.5212875046
N           13.2876932556       5.8795294698       8.2293498111
O           12.3309789528       5.0322662687       7.5490111763
O           13.1123185927       6.3066632214       9.6037008642
O           14.4970450047       6.3111501294       7.5372827780
N           12.6601842535      -0.0134806503       9.8333583585
O           12.8338515842       0.4154649908       8.4589190191
O           11.4448305536       0.4097185986      10.5213428198
O           13.6214640143      10.9371442398      10.5165875426
N            3.8472112175      -0.0141689787       8.2291349064
O            3.6715642426       0.4127791004       9.6037314597
O            5.0558203447       0.4171798889       7.5372459554
O            2.8898776572      10.9263444120       7.5488782021
```

Figure 70. Quantum Espresso Input for relax caculus of Co-ma-bpy based in the phase found by XRD analysis.